UNIVERSITY OF OKLAHOMA

GRADUATE COLLEGE

TOPOLOGICAL TRANSPORT IN SB QUANTUM WELLS

A DISSERTATION

SUBMITTED TO THE GRADUATE FACULTY

in partial fulfillment of the requirements for the

Degree of

DOCTOR OF PHILOSOPHY

By

SHAYNE CAIRNS
Norman, Oklahoma
2015

TOPOLOGICAL TRANSPORT IN SB QUANTUM WELLS

A DISSERTATION APPROVED FOR THE
HOMER L. DODGE DEPARTMENT OF PHYSICS AND ASTRONOMY

BY

Dr. Sheena Murphy, Chair

Dr. Michael Santos

Dr. Kieran Mullen

Dr. Greg Parker

Dr. Carol Silva

Acknowledgments

I would like to first acknowledge my adviser Dr. Sheena Murphy for her excellent tutelage in my graduate studies. I knew from the moment that I came to OU, I wanted to work for Dr. Murphy and she was willing to take me on as a grad student starting my second year. Dr. Murphy was always willing to take time to explain theoretical and experimental concepts. I also enjoyed her input on non-physics related material which gave me a new perspective on issues I was naive too. I would also like to acknowledge the previous grad students who have moved on from Dr. Murphy's lab that contributed to my education here at the university; Ruwan Dedigama and Dilhani Jayathilaka.

I would also like to thank Dr. Michael Santos for his discussions on both physics and non-physics topics. In addition I would like to acknowledge Dr. Santos' research group for their assistance in the growth of the samples presented in the following dissertation, in particular, Chomani Gaspe and Kaushini Wickramasinghe as the growers of the samples studied. Also Tetsuya Mishima for the TEM cross-sectional images and Joel Keay for SEM surface studies of samples mentioned in this dissertation. I want to thank Dr. Johnson, Lu Li, and Rassel Shazzad for their assistance in device processing along with Dr. Mullen and Dr. Uchoa for illuminating theory discussions on topological insulators. I would like to thank my fellow officemates for all of their support during my doctoral studies.

All high field data was taken at the National High Magnetic Field Laboratory (NHMFL) in Tallahassee, FL. I want to thank the administrative and technical staff at the NHMFL for their assistance during research trips at the lab, in particular, Tim Murphy, Glover Jones, and Ju-Hyun Park. All research in this dissertation was supported by the National Science Foundation, Division of Materials Research (DMR 1207537).

Table of Contents

List of Figures

Abstract

The following dissertation will cover the initial studies of Sb quantum wells as topological insulators. The theoretical background and previous studies of topological insulators are covered first, to set the foundation for future discussion. The idea of topology is discussed and how it relates to physical systems like the quantum Hall state is described. Then the theory behind topological band structure and the Z_2 topological insulator system is discussed. This is followed by the experimental observations of topological insulators in 2D and 3D systems. Sb as a topological insulator is introduced in relation to the the first 3D topological insulator observed in Bi-Sb alloys. Due to the large conduction in bulk Sb, quantum confined Sb wells are grown by molecular beam epitaxy (MBE) to reduce bulk conduction.

Sb quantum wells grown by MBE on two types of substrates, GaAs(111) and GaSb(111). Before growth of the Sb well, a 0.5 μm GaSb buffer was grown to provide an excellent lattice matched surface, as GaSb and Sb in the (111) direction have less than a 0.1% lattice mismatch. The initial Sb wells ($\sim$ 30 samples) were grown on GaAs(111) substrates, using two different growth procedures. Surface studies of Sb wells showed a large amount of dislocations originating from the lattice mismatch between the GaAs substrate and GaSb buffer layer; hence a second series of wells was grown on GaSb(111) substrates to alleviate this problem. GaSb substrates from three different manufactures were used: Wafer Tech, New Way Semiconductor, and Galaxy Wafer. Multiple substrate manufacturers were used depending on existing supply at the University, cost of substrates, and availability. Sb wells grown on New Way substrates showed poor quality when compared to wells grown on Wafer Tech and Galaxy substrates and were hence discontinued. Sb wells of excellent quality were then fabricated into Hall bar devices and

nano-wire devices.

Standard device processing steps presented unexpected issues when applied to Sb wells and a revised procedure was formulated. Nano-wire devices were fabricated using electron beam lithography (EBL) and reactive ion etching (RIE). Magneto-transport and quantum interference experiments were then conducted.

To better understand the effects seen in magneto-transport measurements, classical magneto-transport and quantum interference theory is covered. The classical magneto-resistance effect is introduced along with quantum interference effects (e.g. weak localization). These effects are used to explain low and high field data. Zero field conductance measurements show reduced bulk conduction and residual surface conductivity at zero well thickness. Low field measurements exhibit a strong weak anti-localization (WAL) effect that dissipates with increasing temperature. Fits to WAL data using a theoretical model by Hikami, Larkin, and Nagaoka agree well with experiment and a determination of the phase breaking length and α pre-factor is possible. The temperature and thickness dependence of the fitting parameters was investigated. High field magneto-transport is done in tilted field to determine whether the observed magneto resistance is 2D or 3D in origin. An evolution of the high field magneto resistance from parabolic (B^2) to linear (B) field dependence is seen for decreasing well thickness. This effect can be reproduced using a simple model containing bulk and WAL terms in concert. Initial measurements of nano-wire devices show the presence of universal conductance fluctuations (UCF), but more work is required to form a complete picture.

In conclusion, the Sb quantum wells in this study show reduce bulk conduction when compared to bulk films. Also the presence of residual conduction at zero well thickness indicates surface transport as expected for a 3D topological insulator. Parameters determined from WAL fitting are independent of well thickness which

points to 2D surface conduction. This is also seen in tilted field measurements when data is plotted versus perpendicular field. All of these results point towards 2D surface conduction with a bulk background which is confirmed by the simple model used to explain high field magneto-transport data using surface and bulk channels in parallel.

Chapter 1

Introduction

Topological insulators (TIs) are a newly predicted phase of condensed matter with unique intrinsic properties. A TI, as it name implies, is an insulator that is distinguished from a normal band insulator by a topologically protected conducting state at the interface with a trivial insulator. This conducting interface state is only half a normal metal; it is helical with the spin orientation related to the momentum. It is also required to exist and thus is impervious to localization by weak disorder. The existence of these materials were first predicted [2] and then confirmed by experiment[3]. TIs can be broken into two different types based on system dimensionality, 2D or 3D.

The first 2D TI to be experimentally confirmed was in CdTe/HgTe quantum wells [3] while the first 3D TI was observed in $Bi_{1-x}Sb_x$ alloys [5]. Following these discoveries a multitude of materials are expected exhibit a 3D topological state (e.g. Bi_2Se_3, Bi_2Te_3, strained HgTe, etc.)[11, 12]. One of the main pitfalls however, is that many of the candidate materials exhibit excess bulk conduction due to unintentional doping or defects. This makes transport measurements rather difficult that isolate the topological surface conduction from the bulk. Attempts have been made to combat this issue by compensation doping and gating.

In this dissertation we will investigate transport measurements on a predicted elemental TI, antimony (Sb). An elemental TI provides an advantage that the stoichiometry is simple, avoiding defect issues related to substitution of unwanted elements and alloy defects. While Sb is predicted to host a topological phase[6] its bulk structure is semi-metallic and measurement of the topological state is shorted through the bulk. To overcome this, the Sb films are quantum confined

to reduce bulk conduction.

This dissertation is organized as follows: Chapter 2 discusses the theory behind topological insulators and the concept of a Z_2 topological insulator as proposed by Kane and Mele[13]. This is followed by an overview of previous experimental measurements of 2D and 3D topological insulators. Observations in CdTe/HgTe quantum wells and $Bi_{1-x}Sb_x$ alloys are discussed. The theoretical prediction that Sb hosts a topological phase and its experimental implementation is also addressed.

Chapter 3 provides details on the molecular beam epitaxy (MBE) growth of the ultra thin Sb wells and their physical characterization. Wells were grown on both, GaAs(111) and GaSb(111) substrates. Physical characterization was carried out using cross-sectional and surface scanning electron microscopy (SEM) along with cross-sectional transmission electron microscopy(TEM). A comparison of the growth quality on both substrates is provided.

Chapter 4 gives an outline of the standard photolithography processing steps used to produce devices measured in this dissertation. Problems and solutions that occurred during fabrication are also addressed. Details are also provided for subsequent processing via electron beam lithography of nano-wire devices for quantum interference experiments.

Chapter 5 gives an overview of magneto-transport (Drude model and Hall effect) and quantum interference theory (universal conductance fluctuations and weak localization). The Hikami, Larkin, and Nagoka (HLN) model[10] of weak antilocalization is discussed.

Chapter 6 covers the experimental measurements and their analysis and implications. Zero field conductance measurements are taken to determine surface and bulk effects. High field magneto-transport measurements for a range of film thicknesses are reported and their unique evolution is analyzed with current theories

and low field magneto-transport is explained within the framework of the HLN model. Additionally preliminary magneto-transport measurements on nano-wire devices are addressed.

Chapter 2

Topological Insulators

2.1 Theoretical Prediction

Conventional solids can be divided into two types: insulators and conductors (see Figure **2.1**) with conductors having partially filled valence or conduction bands (metals and semimetals) and insulators having a filled valence band and empty conduction band (semiconductors and insulators). When topology is considered the insulators divide into two more categories, trivial and topological insulators. At any interface between trivial and topological insulators, a conducting state must form in order to allow the topological index (distinct for the two types of insulator) to change from one value to the other. This chapter will introduce topological insulators starting with topology, advancing to an analog of the topological insulator, the quantum Hall effect and then discussing topological insulators in greater detail.

Topology relates to the genus of geometrical objects. The genus, g, of a geometrical object counts the number of holes and allows us to classify the topology of different geometrical objects; for example when comparing the genus (Figure **2.2** (c) and (f)) of a sphere (g=0) to a donut (g=1). If we consider a donut and coffee cup, while they appear completely different, it is possible to continuously deform a donut into a coffee cup and vice versa. However, the donut cannot be continuously deformed into a sphere without filling a hole, thus the objects are in different topological classes. We identify a "topological invariant" (in this case genus) with topologically distinct objects.

A condensed matter system for which topology is important is the quantum

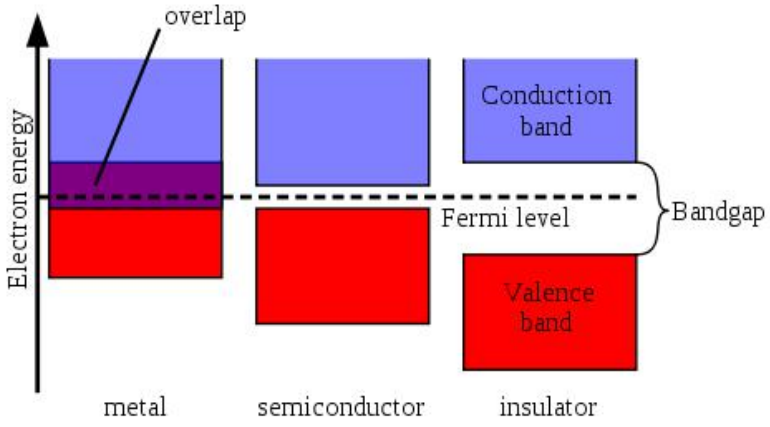

Figure 2.1: Band representation of a metal, semiconductor, and insulator. When the conduction band and valence band overlap this is referred to as a metal, or a band is partially filled. An insulator is where there exists a bandgap between an empty conduction and fully filled valence band. A semiconductor in this picture can be thought of as a poor insulator, with a very small bandgap.

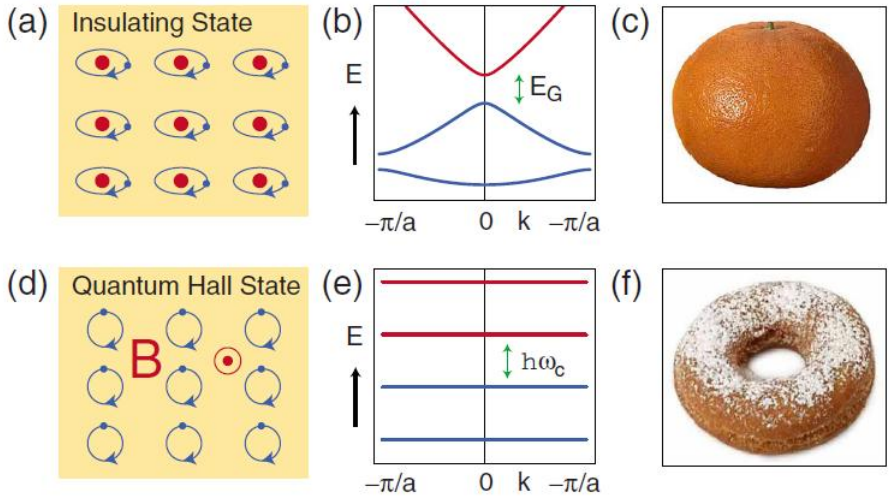

Figure 2.2: (a) Atomic insulator with positive cores and orbiting electrons. (b) A simple band structure representation of an insulator with band gap E_G. (d) The QHS with cyclotron orbits under applied magnetic field. (e) Landau quantization of the bands, separated in energy by $\hbar\omega_c$. (c) and (f) Two objects with a different associated genus, g. (c) A sphere with g=0. (f) A donut (torus) with g=1. The genus is a geometrical analog to the Chern number. Figure taken from [1].

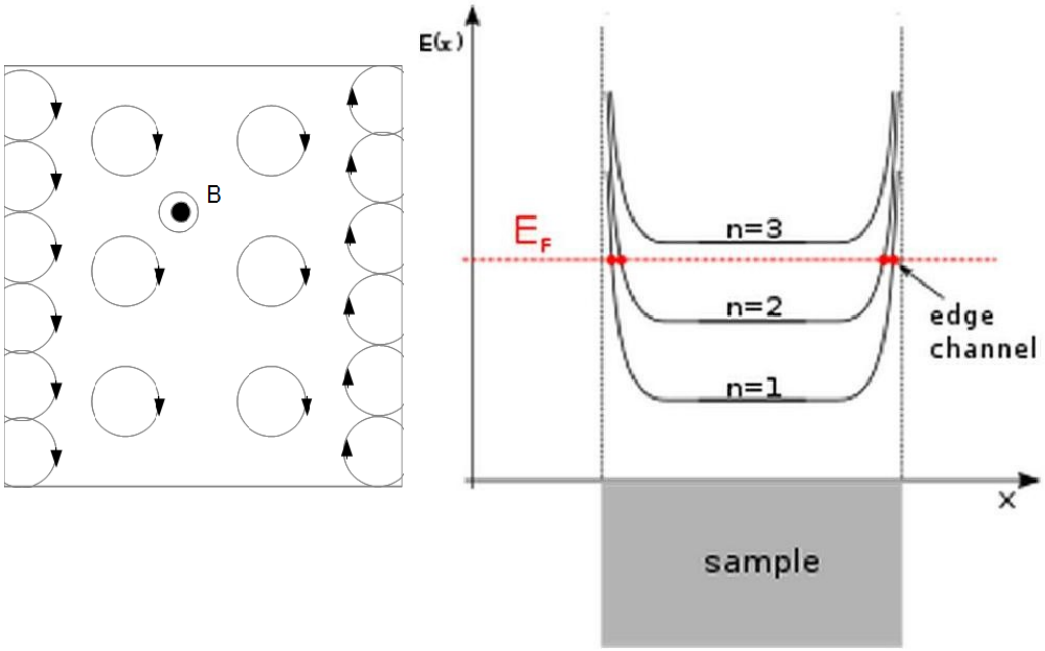

Figure 2.3: On the left is a pictorial representation of the quantum Hall state where electrons are localized by cyclotron orbits in the interior of the sample while electrons can move along the edge. The diagram on the right represents the energy vs. position plot showing Landau levels that bend upwards at the sample edge. The Fermi level can be placed in between Landau levels where there is an insulating interior with a conducting edge state. In between n=2 and n=3 the Chern number counts the number of edge states per an edge; for this case n=2.

Hall state[14, 15] (QHS). At low temperatures ($\sim$ 4 K), a high mobility($\sim$ 100,000 cm^2/Vs) two dimensional electron system in a strong magnetic field, ($>$ 2 T), will display quantized Hall resistance. This arises from the quantization of the energy levels due to cyclotron orbits (Landau levels) (See Figure **2.2**). However at the perimeter of the sample carriers execute skipping orbits that allow for conduction at the edge (see Figure **2.3**); these edge states are special because they only traverse in one direction (i.e. chiral) and are therefore, impervious to backscattering. When the Fermi energy lies between Landau levels, say n=2 and n=3 (Figure **2.3**), the sample interior is insulating while two edge states are crossed on either side of the sample. The number of edge states crossed per an edge specifies the relevant topological invariant, also known as the Chern number, which takes on integer values. If we lower the Fermi level to lie between n=2 and n=1, it must first cross a conducting interior state. Therefore when the Chern number changes between regions of different integer values there has to be a conducting state, this is referred to as the bulk-edge correspondence.

The Chern number is a tool used to classify the topological nature of a system; it is analogous to genus and has a similar topological invariance. For genus the geometrical space is used to determine genus while for topological insulators, the analogous geometric space is in the Brillouin zone (BZ) and by examining the band structure for a given system we can calculate the associated topologically invariant number.

2.2 Z_2 Topological Insulators

While the QHS is an analog of a TI, it requires an applied magnetic field. A Z_2 topological insulator has similar properties to the QHS but does not require an applied magnetic field. A key component of the Z_2 TI class is that it consists

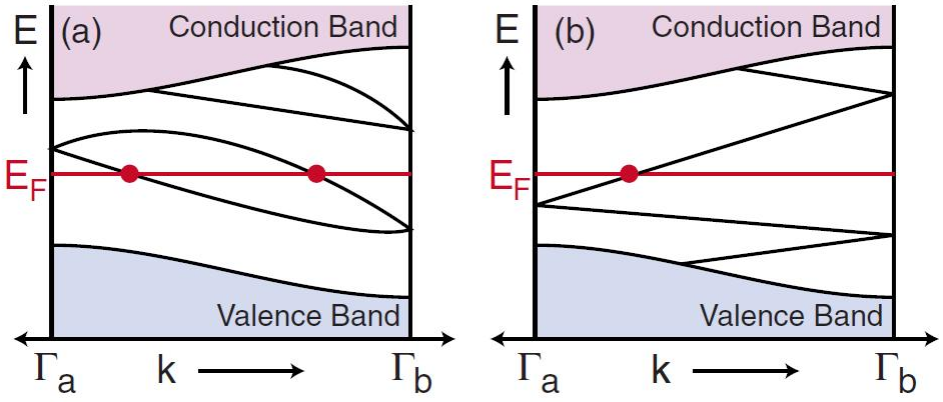

Figure 2.4: Two possible situations for the band structure of a Z_2 TI in the BZ. (a) Surface states which are degenerate at the Kramer's points Γ_a and Γ_b connect pairwise across the BZ. (b) Surface states that instead switch partners across the BZ. The Fermi level in (a) crosses the surface bands an even number of times, while in (b) it crosses an odd number of times. An odd number of crossings gives topologically protected conducting boundary states. Figure taken from [1].

of spin $\frac{1}{2}$ particles with a strong spin orbit interaction. Spin $\frac{1}{2}$ particles have an interesting property under time reversal, each energy level is at least double degenerate; this is known as Kramer's degeneracy theorem. Therefore, application of the time reversal operator on the state E(k,↓); yields:

$$E(k,\downarrow) = E(-k,\uparrow) \tag{2.1}$$

Since our system is periodic in k, then at the BZ edges $k_{BZ} \rightarrow -k_{BZ}$ gives:

$$E(k_{BZ},\downarrow) = E(k_{BZ},\uparrow) \tag{2.2}$$

Hence at particular symmetry points in the BZ, the levels must be spin degenerate; these points in k-space are referred to as time reversal invariant momenta (TRIM).

Plotted in Figure **2.4** we have the band structure of a material in the first

BZ. At the TRIM points Γ_a and Γ_b, Kramer's degeneracy must hold. Away from these TRIM points the spin orbit interaction can split this degeneracy. There are two scenarios for how the edge states can split and reconnect at the special TRIM points. In one case, the edge states can pair together as in Figure **2.4**(a) or they can switch partners as in Figure **2.4**(b). In Figure **2.4**(a) the Fermi level can be shifted such that either no edge states are crossed or only two i.e. an even number. In Figure **2.4**(b) however the Fermi level cannot be shifted such that it will not cross an edge state i.e. it must always cross an edge state at least once. In general, this scenario always has an odd number of crossings. We can now classify time reversal invariant Hamiltonians that satisfy Kramer's theorem by an new invariant called ν which takes integer values 0 or 1 i.e. # of crossings (mod 2).

Whether the Fermi level crosses and even or odd number of states depends on the underlying band structure and determines the value of ν. The mathematical formula for the calculation of ν in general is:

$$(-1)^{\nu} = \prod_{n=1}^{N} \delta_n \tag{2.3}$$

where N = the number of TRIM points and δ is related to the determinant of a matrix representation of the Bloch wave functions at the TRIM points. Calculation of this property can be quite difficult but using particular symmetries the problem can be simplified. If a crystal has inversion symmetry[13] there is a shortcut to calculating ν. At the TRIM points the eigenstates have associated parity eigenvalues $\epsilon = \pm 1$. The Z_2 invariant can then be calculated from the following,

$$\delta_n = \prod_{m} \epsilon_m(\Lambda). \tag{2.4}$$

The product here is taken over all occupied bands at the TRIM points(Λ). Thus by a knowledge of the parity of each occupied band we can determine whether a system is topologically trivial (ν=0) or non-trivial (ν=1).

Unlike the QHS, the Z_2 topological class can exist in either two or three dimensional (2D or 3D) structures. Additionally because spin-orbit coupling splits the degeneracy at all points other than the TRIM, the conducting states have their spin locked at a right angle to their momentum and 180° backscattering is suppressed. In 2D TIs, this suppression of backscattering manifests itself as quantized edge state conductance, as follows from Landauer-Buttker ballistic transport theory[16]. For 3D TIs the conduction is on the whole surface and the backscattering effect appears as weak anti-localization[10, 17, 18], which will be discussed in detail in Chapter 5 . While the surface/edge states of a TI are protected from elastic backscattering, they are not protected from inelastic scattering because inelastic scattering is associated with phase de-coherence which breaks time reversal symmetry; thus the quantized conductance can only be observed on length scales less than the phase breaking length which has ramifications on device size for topological transport measurements. Another property of the surface/edge states is their Dirac (i.e. linear and mass less) like dispersion similar to graphene[19]. This has the potential to host a special particle referred to as the Majorana fermion[20–22]. Majorana fermions are special in that they are their own anti-particle; this unique characteristic has possible application in quantum computing[23], thus the great interest in TIs.

2.3 Previous Experimental Measurement of TIs

2.3.1 2D Topological Insulators

Breaking from the normal order of the discovery of novel materials, TIs were theoretical predicted before being observed. In 2006 it was suggested a 2D topological state could exist in HgTe/CdTe quantum wells[2]. HgTe/CdTe structures have a strong spin-orbit interaction due to their large atomic number. As a reminder, the spin-orbit interaction is important because it breaks the Kramer's degeneracy away from the the TRIM points; this allows the possibility that the Fermi level crosses an odd number of states in the gap leading to topologically non-trivial band structure. CdTe has typical ordering of its bands with an s-like conduction

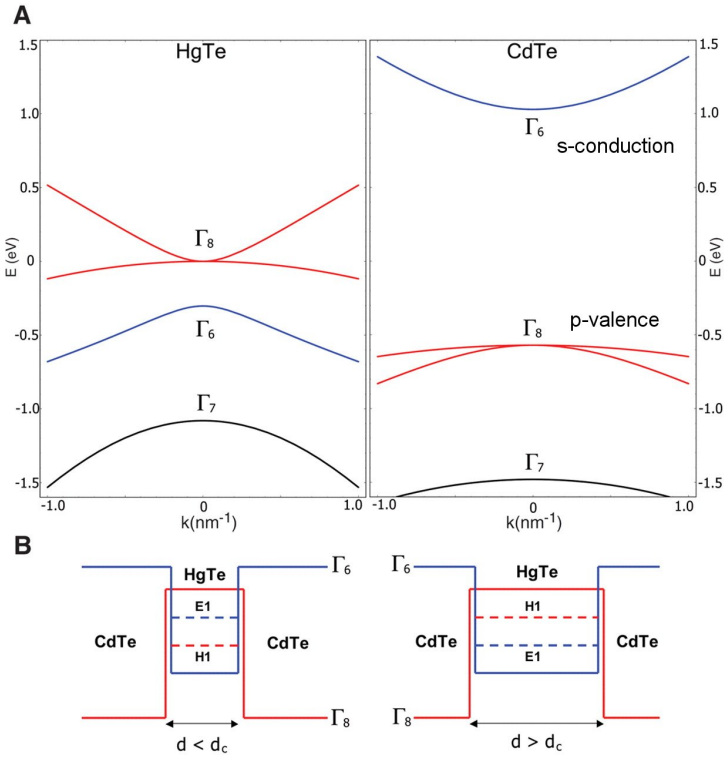

Figure 2.5: (a) Band structure of bulk HgTe and CdTe near the Γ point. (b) In the typical regime ($d < d_c$) the first electron sub-band, E1, is higher than the first hole sub-band, H1. In the inverted regime ($d > d_c$), H1 is higher than E1. Figure taken from [2].

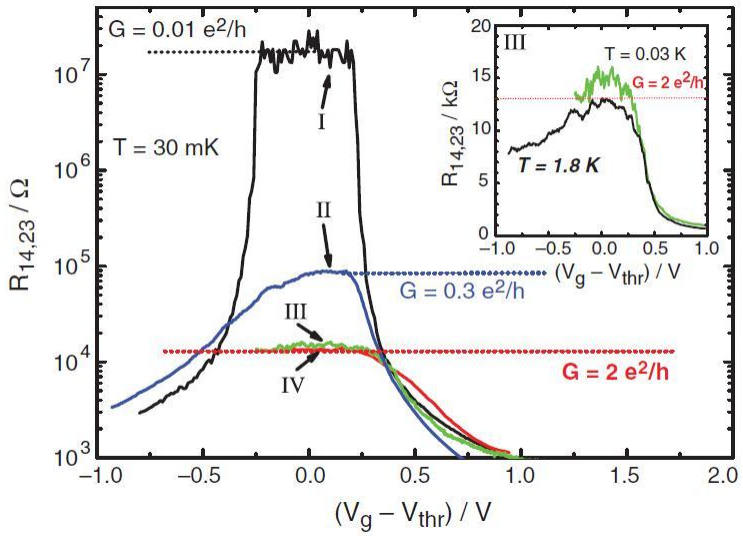

Device	Length	Width
I, II	20 μm	13.3 μm
III	1 μm	1 μm
IV	1 μm	0.5 μm

Figure 2.6: Plot of 4pt resistance vs gate voltage for I-IV devices at 30 mK. The gate voltage is swept to move the Fermi level into the gap. Device I (d=5.5 nm) shows an insulating gap as expected in the normal regime. Device II-IV (d=7.3 nm) are in the inverted regime. Device II plateaus at a conductance smaller than the expected G=$2e^2/h$ since its voltage probe separation is longer than the phase breaking length. Devices III and IV have voltage probe separations on the order of the phase breaking length and plateau at the expected conductance for ballistic transport. The inset shows the temperature dependence of the the plateau for device III. Figure taken from[3]. The device dimensions are given in the side table.

band (Γ_6) above a p-like valence band (Γ_8)(See Figure **2.5**a). However, in HgTe the p-like valence band rises above the s-like conduction band leading to an inverted band structure(Figure **2.5**a). If HgTe is quantum confined by sandwiching it between two layers of CdTe, the relative position of the HgTe conduction and valence bands can be controlled by the thickness of the well. As the well thickness decreases, the conduction band is shifted up in energy and the valence band is shifted down in energy. For a critical thickness, d_c, there is a phase transition in the HgTe band structure: for $d < d_c = 6.3\,\text{nm}$, HgTe has the typical band order, but when $d > d_c$ there is a band inversion(Figure **2.5**b) (and correspondingly a phase transition from a trivial insulator to a topological insulator).

The first experimental observation of a TI was made in HgTe/CdTe quantum wells (QWs)[3]. In the experiment, multiple HgTe QWs samples were grown with different well thicknesses smaller and larger than d_c and Hall bar devices were fabricated with differing lengths and widths. Low temperature four-point measurements were made as a function of gate voltage (Figure **2.6**) to tune the Fermi level through the HgTe bulk gap. Device I (d=5.5 nm) shows insulating behavior (i.e. maximum in resistance) when tuned through the gap as expected for $d < d_c$. Devices II-IV (d=7.3 nm) have inverted band order, but have different Hall bar dimensions, L (μm) x W (μm) as shown in the table adjacent to Figure **2.6**. Device III and IV show the expected quantized conductance of $2e^2/h$ for two ballistic channels. While Device III and IV have different widths, the devices have the same value of conductance, indicating edge transport. Device II despite having inverted bands does not show the same quantized conductance value, this is because the voltage probes are separated by more than the phase breaking length and inelastic scattering has reduced the ballistic conductance. The same group also showed that strained bulk HgTe is a 3D TI[12]. Under strain HgTe will open a gap between the heavy hole and light hole bands and the topological surface states will lie in this gap. The signature that strained HgTe was a 3D TI was the observation of the quantum Hall effect, a characteristic feature of a 2D electron system. This 2D electronic system is the manifestation of the topological conducting states for the 3D TI surface.

2.3.2 3D Topological Insulators

The first 3D TI however, was not strained HgTe but rather was made in BiSb alloys[5]. Figure **2.7**(a) is the band structure of bulk Bi showing semi-metallic ordering with a direct gap at the L point where the conduction and valence band

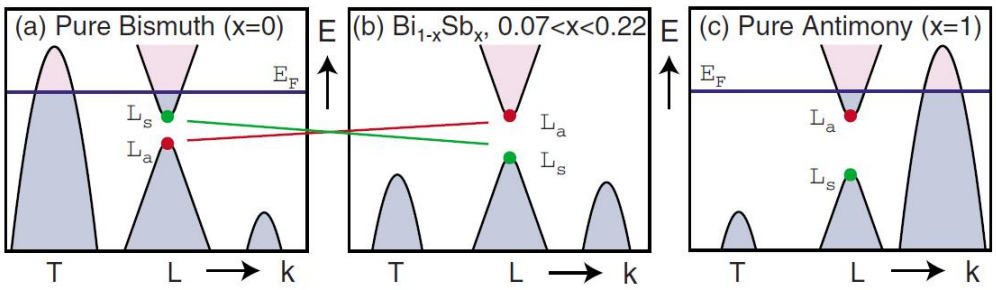

Figure 2.7: Evolution of the band structure for $Bi_{1-x}Sb_x$. (a) Band structure of pure Bismuth in the semi-metallic state. Note that the conduction and valence band at the L point are in the normal order $L_{s,a}$. (b) When 0.07<x<0.22, the semi-metallic bulk transitions to a semi-conducting order where the nature of the bands have inverted. (c) For x>0.22 the band structure reverts to semi-metallic like behavior. Figure taken from [1]

are derived from symmetric (L_s) and anti-symmetric (L_a) orbitals. Substituting Sb in for Bi there is an evolution of the band structure[24]. At x $\approx$ 0.07 the valence band at the T point drops below the L point valence band leaving an direct-gap insulator at the L point. Note that the bands at the L point have inverted ordering, analogous to HgTe QWs. As x is increased greater than 0.22, the valence band at the K point rises above the L point conduction band restoring the semi-metallic Sb phase.

Since both Bi and Sb have inversion symmetry, equation **2.4** can be used to determine the Z_2 topological invariant. The parity eigenvalues (Figure **2.8**) for the occupied states at the TRIM points were calculated in [4] and Fu and Kane [13] were able to calculate the topological class of Bi and Sb. For this calculation one needs the parity eigenvalues for the five occupied bands, which are represented by the five lowest energies at the TRIM points (Γ, T, L, and X)[a]. While the calculation for Bi(Figure **2.8**) reveals ν=0 (trivial topology), that

[a]One may notice that for Bi only four levels at T appear to lie below the Fermi energy and that six levels appear to lie below the Fermi energy for Bi and Sb. In reality five levels lie below the Fermi energy at each TRIM point for each of the materials. The discrepancy is due to small uncertainties in the band structure calculations

TABLE III. Energy levels of Bi (in eV) at the symmetry points T, Γ, L, and X.

T_6^-	−12.2442	Γ_6^+	−14.0000	L_s	−11.9545	X_a	−12.1649
T_6^+	−11.1331	Γ_6^-	−8.0870	L_a	−11.5966	X_s	−10.3162
T_6^-	−1.1798	Γ_6^+	−2.5364	L_s	−1.7896	X_s	−5.6525
T_6^+	−1.1196	Γ_6^+	−1.1289	L_a	−1.6669	X_a	−4.1632
T_{45}^-	0.0111	Γ_{45}^+	−0.8238	L_a	−0.0403	X_a	−3.1047
T_6^+	0.3813	Γ_6^-	0.2430	L_s	−0.0267	X_s	2.3508
T_6^-	0.9529	Γ_6^-	1.6893	L_s	0.8024	X_s	3.2956
T_{45}^+	1.4754	Γ_{45}^-	1.7878	L_a	0.9201	X_a	4.4031

Energy levels of Sb (in eV) at the symmetry points T, Γ, L, and X.

T_6^-	−12.022	Γ_6^+	−13.446	L_s	−11.659	X_a	−11.607
T_6^+	−10.378	Γ_6^-	−7.150	L_a	−11.156	X_s	−9.916
T_6^-	−1.252	Γ_6^+	−2.684	L_s	−2.421	X_s	−6.571
T_{45}^-	−0.814	Γ_6^+	−1.759	L_a	−2.145	X_a	−4.730
T_6^+	−0.332	Γ_{45}^+	−1.454	L_s	−0.786	X_a	−4.217
T_6^+	0.732	Γ_6^-	1.076	L_a	−0.0899	X_s	2.579
T_6^-	1.125	Γ_6^-	1.836	L_s	0.166	X_s	3.229
T_{45}^+	1.474	Γ_{45}^-	2.114	L_a	0.991	X_a	4.135

TRIM	Bismuth	Antimony
T	-1	-1
Γ	-1	-1
L	-1	+1
X	-1	-1
Index	+1	-1
ν	0	1
Topological?	Trivial	Non-trivial

Figure 2.8: Calculation of the energy levels in Bi and Sb at the TRIM points. The parity indices(+,-,a,s) for all occupied bands are used to calculate the Z_2 topological invariant using equation **2.3** and **2.4**. Occupied bands are represented by the lowest five energy bands. Energy level tables taken from [4]

for semi-metallic Sb has ν=1 (non-trivial topology). For $(0.07 < x < 0.22)$ the semiconducting alloy inherits its topological nature from the semi-metallic Sb making it a predicted 3D topological insulator.

This prediction was confirmed by Hasan et al.[5] using angle resolved photo emission spectroscopy (ARPES) to investigate the topological band structure of BiSb alloy and Sb. In ARPES a photon source causes the emission of electrons from the occupied bands in the crystal. These emitted electrons are collected and their energy is measured. Once the initial and final energy are known the momentum can be calculated and the band structure can be reconstructed. Figure **2.9** shows the ARPES mapping along the $\bar{\Gamma} - \bar{M}$ direction for both BiSb and Sb. These ARPES maps directly confirmed the theoretically predicted band structure. Since the work done on BiSb alloys, there has been a plethora of TIs predicted and measured including chacolgenides (i.e. Bi_2Se_3, Bi_2Te_3, Sb_2Te_3, etc.), topological crystalline insulators, and complex compounds[11].

Many 3D TIs suffer from a large bulk conduction due to unintentional doping

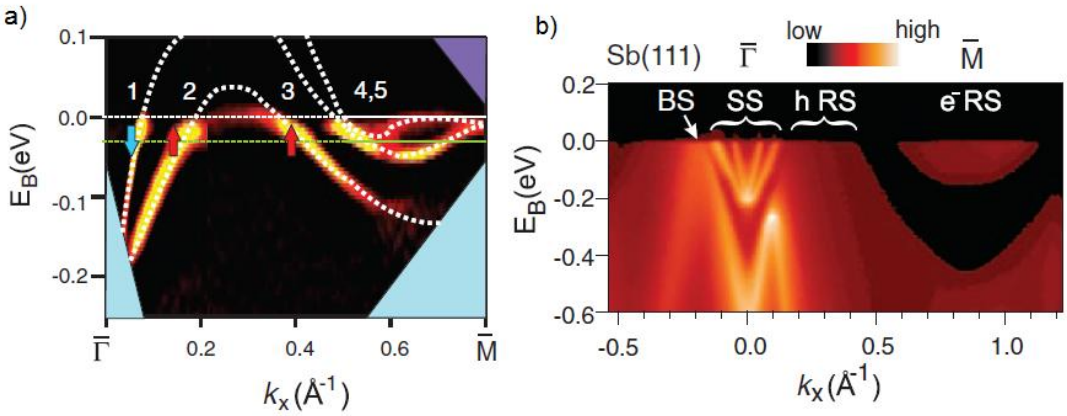

Figure 2.9: a) ARPES plot for $Bi_{1-x}Sb_x$ showing the trace of surface state bands within the gap. The numbers count the crossing of the surface states across the Fermi level. b) ARPES plot for Sb(111) showing the predicted surface bands. Bulk states are labeled as BS and surface states as SS. Figure taken from [5]

from vacancies. This effect can be corrected by gating or doping. In the case of Sb however, the bulk conduction comes from the semi-metallic bands. This can be suppressed by quantum confinement. In quantum confinement we start with the infinite square well picture, where the energy levels inside the well are express as

$$E_n = \frac{\hbar^2 n}{2m^* L^2} \tag{2.5}$$

where E_n is the nth energy level where n takes increasing integer values starting at n=1, $\hbar$ is the reduced Planck constant, m^* is the effective mass, and L is the well width. Therefore, as the well width is decreased the nth level increases in energy. Specifically Zhang *et al.* [6] calculated quantum confinement of Sb(111), will cause the bulk bands to separate and decrease the bulk conduction. In the same study, Sb was also predicted to undergo multiple phase transitions as a function of decreasing film thickness from a topological semi-metal to a 2D TI phase and finally a trivial insulator. The trivial insulator phase arises from the top and bottom surfaces hybridizing and opening a surface gap (Figure **2.10**(d)). An ARPES study was carried out on ultra-thin Sb(111) films confirming the

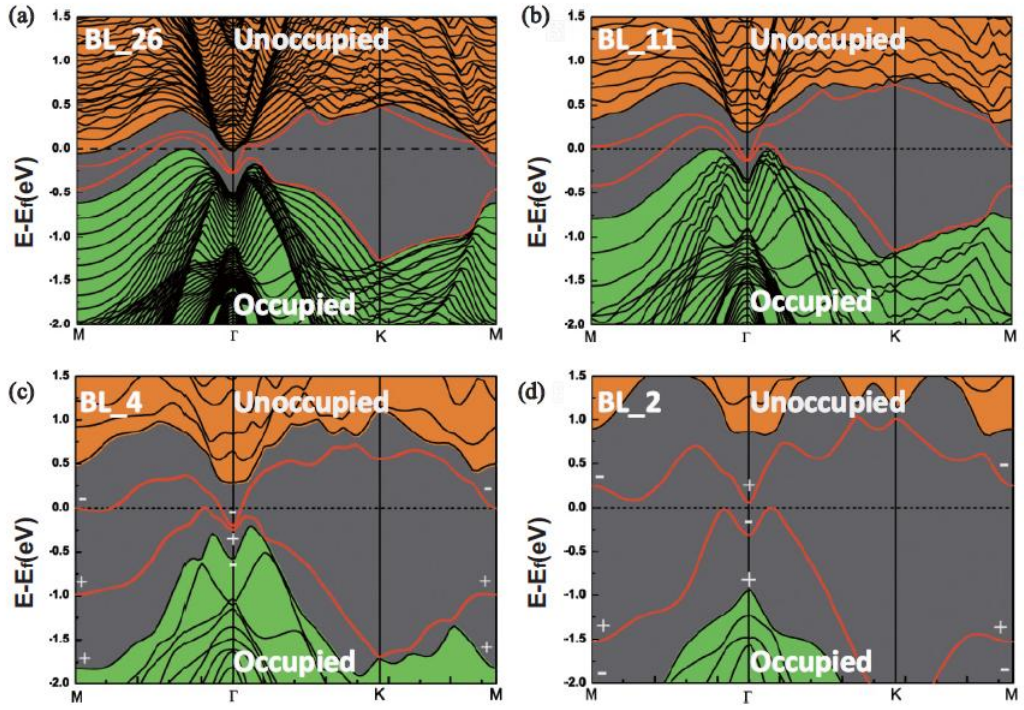

Figure 2.10: Calculated band structure for Sb(111) at different thicknesses. Bulk bands are shown in the green and orange, while the red lines are surface states. (a) At 26 BL, Sb shows semi-metallic band structure associated with the bulk. (b) At 11 BL a bulk gap is beginning to open allowing for the measurement of only the surface bands. (c) At 4 BL, a large bulk gap has opened while still retaining the gap-less Dirac-like surface states. (d) Once the thickness is reduced to 2 BL a surface gap opens. Figure taken from [6]

topological nature of the band structure[25]. An interesting result of the ARPES study, was that for films below 4 BL, the expected surface gap did not open. This was attributed to inter-facial bonds between the film and substrate unaccounted for in calculations of free-standing films. Since then additional theoretical studies have also predicted that Sb(111) hosts a topological phase[26–28].

Chapter 3

Growth and Characterization of Sb wells

Sb crystallizes in a rhombohedral structure; along (111) the crystal forms in bilayers (BL) and follows an ABC stacking order (see Figure **3.1**). To form quality ultra-thin Sb layers, an appropriate lattice-matched barrier material must be chosen. Zincblende GaSb has a lattice constant of a= 6.0959 Å while the in-plane lattice constant of of GaSb(111) is 4.3105 Å. Both GaSb(111) and Sb have an hexagonal arrangement of surface atoms along the (111) surface where their atomic spacings are comparable[29] (GaSb(111) a=4.310 Å and Sb a=4.310 Å) such that the mismatch between the two along the $\langle 111 \rangle$ direction is less than 0.1%. For transport studies of TIs it is important to minimize the bulk conduction due to defects and unintentional doping, since they can dominate the conduction if their density is too high. GaSb has a band gap of 0.8 eV at low temperatures which is larger than the predicted Sb gap at the thicknesses grown for this study[6, 30]. Due to the elemental composition of our materials (Sb on GaSb) the likelihood of dopants due to vacancies in the GaSb layers is small when compared to other TI compounds (e.g. Bi_2Se_3, Bi_2Te_3). For these reasons, GaSb was chosen as the layer on which to grow our Sb wells. Two different substrates were chosen: GaAs with a GaSb epilayer; and GaSb with a GaSb epilayer, both are described in the sections that follow.

3.1 Sb on GaAs(111) substrates

The first round of Sb samples ($\sim$ 30) were grown by molecular beam epitaxy (MBE) on semi-insulating (SI) GaAs(111)A[7]. Figure **3.2** shows the MBE growth

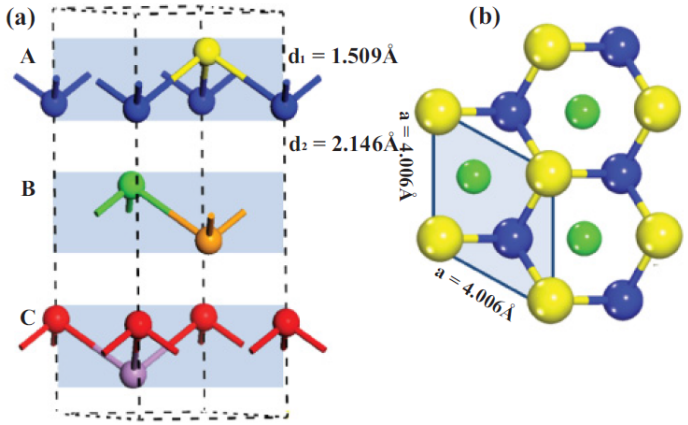

Figure 3.1: (a) Unit cell of Sb showing ABC stacking, with 1 BL spacing equivalent to $d_1 + d_2$. (b) Hexagonal (111) surface view of Sb crystal. Figure taken from [6]

GaSb cap (optional)	GaSb cap (optional)
Sb layer	Sb layer
0.5 um GaSb buffer	0.5 um GaSb buffer
SI-GaAs(111) substrate	n-GaSb(111) substrate

Figure 3.2: MBE growth stacks for the two different structures grown for this study. The Sb layer is of variable thickness between different growths. Samples grown without a GaSb cap were used for surface FE-SEM studies. SI stands for semi-insulating.

stack for these structures. A 0.5 μm undoped GaSb buffer layer is grown to provide a clean latticed match surface for the Sb growth. The first set of samples ($\sim$10) were grown by leaving the Sb shutter open and allowing the substrate to cool to 220°C after growth of the GaSb epilayer. During the substrate cooling the RHEED (Reflection High Energy Diffraction) pattern was monitored until the patterned changed from 5x1 to 2x1, indicating that Sb had deposited on the surface. RHEED is a technique used to characterize the surface quality of a material. The resulting diffraction pattern correlates to the crystalline order of the sample and depending on the material there are standard diffraction patterns for high quality growth. This growth method had limited ability to control the well thickness since RHEED does not indicate the initial amount of Sb deposited.

A revised growth process was then used for the rest of the samples in this series ($\sim$ 20) where the epitaxial Sb layers were grown at a fixed substrate temperature ranging from 300°C to 280°C. In this process, after the GaSb epilayer was grown the substrate temperature was lower with the Sb shutter open. When the RHEED pattern changed from 2x6 to 5x1, the Sb shutter was closed at 65°C below this transition temperature. The substrate was then lowered an additional 200°C with the Sb shutter closed; the RHEED pattern stayed 5x1 through out this additional cool-down. The substrate was then set to the desired growth temperature and the the length that the Sb shutter was opened determined the Sb well thickness.

The thickness of the layers were controlled by the length of time the Sb shutter was opened. A thin ($\approx$ 10 nm) cap is grown to protect the underlying Sb layer from surface oxidation. Samples without caps were grown for surface characterization measurements. A series of physical and electrical characterization measurements were made to determine the quality of the wells.

The growth quality was determined by field-emission scanning electron microscopy (FE-SEM) and field-emission transmission electron microscopy (FE-

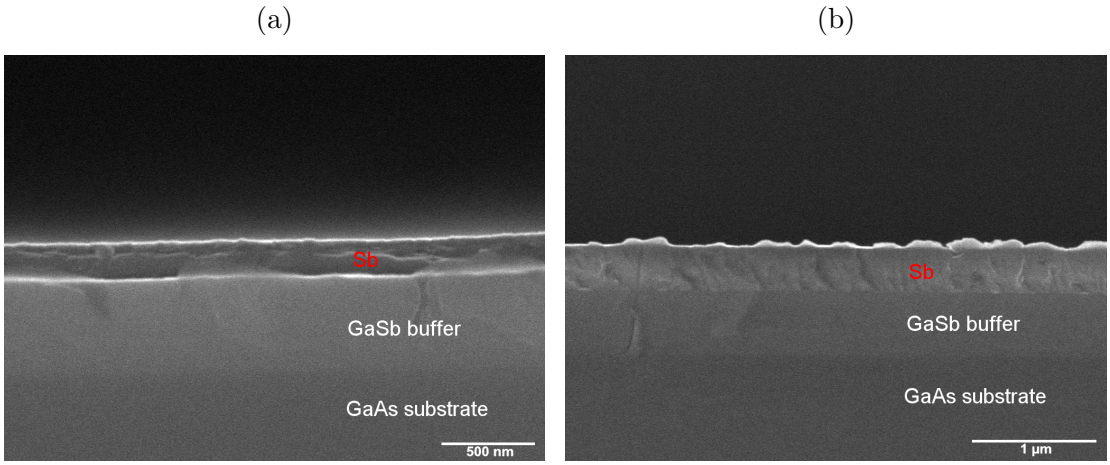

Figure 3.3: Cross-sectional FE-SEM images of thick Sb layers used for growth rate calibration. (a) 30 min growth time produced a Sb layer of ∼180 nm. (b) 60 min growth time produced a Sb layer of ∼350 nm. Both wells were grown at a substrate temperature of 300°C.

TEM). The layer thickness was not able to be determined during growth, so post-growth cross-sectional measurements of thick Sb wells (deposition times $\geq$ 30 min) were made. In Figure **3.3** are cross-section images of the 30 min and 60 min wells grown at 300°C, where the 30 min well appears to be half the thickness of the 60 min well. This indicates that we have well controlled Sb deposition and a deposition rate of 0.1 nm/s was determined. A cross-sectional FE-TEM[7] image was taken (Figure **3.4**) of an ultra-thin layer grown at 300°C for 41s. The expected well thickness of 4.1 nm (growth time 41s and growth rate of 0.1 nm/s) is confirmed indicating excellent control of layer thickness even for ultra-thin wells. Figure **3.4** also shows the Sb and GaSb wells have excellent crystalline order with sharp clean interfaces.

Surface characterization was performed using FE-SEM in plan-view using a toroidal semi-conductor backscatter detector. This detector is sensitive to compositional differences and crystalline defects. Figure **3.5** shows two FE-SEM images for two wells of similar growth time but at different substrate temperatures. The triangular structures arise from growth on the (111) surface (Figure **3.1**). The

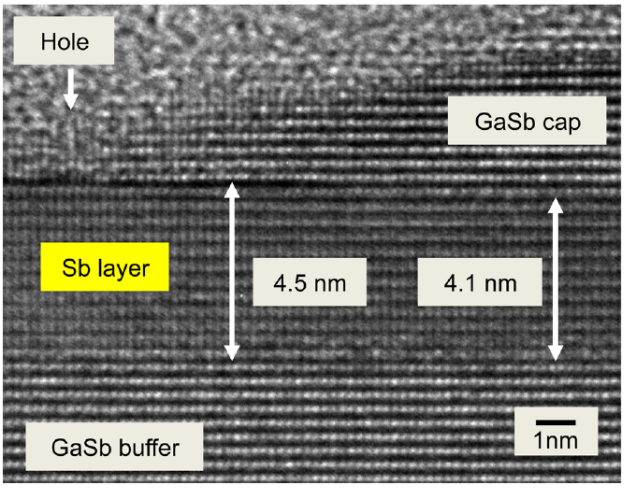

Figure 3.4: Cross-sectional FE-TEM image of 41s Sb layer grown at 300°C. Sb layer shows well ordered growth and clean interfaces between layers. Measured layer thickness is close to the expected thickness of 4.1 nm. Image taken along the ⟨211⟩ direction. Hole in GaSb cap is indicative of non-uniform coverage. Image taken from [7].

larger triangular defect is associated with the GaSb/GaAs lattice mismatch and the dark spots are voids also attributed to dislocations from the lattice mismatch. When comparing Figure **3.5**(a) and (b) we can see that as the substrate temperature is reduced, the number of voids decreases. Subsequent growths on GaSb substrate were performed at lower temperatures to create more continuous wells.

Figure **3.6** is a plan-view FE-SEM image of a ∼1.5 nm sample with no cap. The substrate temperature was held at 280°C. A new feature present here is the dark lines running throughout the image. These dark lines correlate to bilayer step edges of the Sb growing on the (111) surface. The density of dark point features seen is similar to that seen in Figure **3.5**.

Electrical measurements were made on ≈ 5 x 5 mm samples in the Van der Pauw configuration. Contact was made to the wells using indium mechanically pressed onto the sample. The contacts were not annealed to avoid parallel conduction from the substrate. Four-point and Hall measurements were made at a

(a) (b)

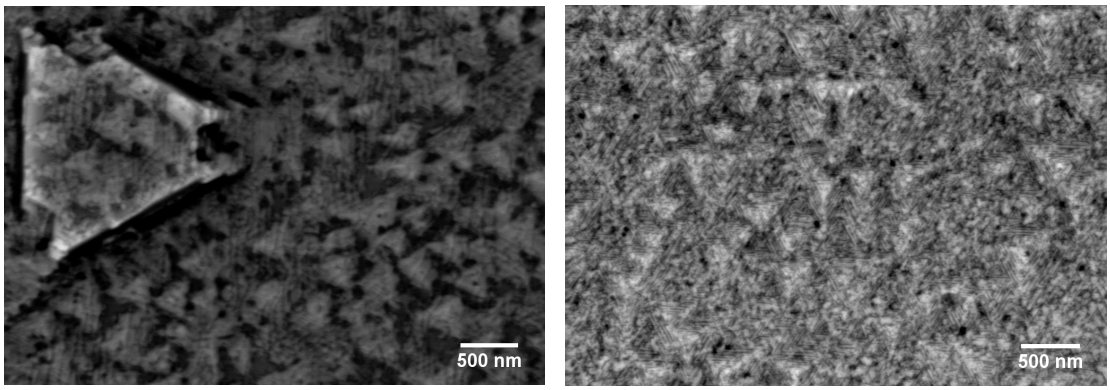

Figure 3.5: (a) Plan-view FE-SEM image showing triangular structures originating from growth along the (111) surface. Sample thickness is ≈4.0 nm and grown at a substrate temperature of 300° C. (b) Plan-view of 4.0 nm sample grown at substrate temperature of 280° C. The lower temperature growth improves surface coverage indicated by a reduction of surface voids. Both samples are capped with ∼10 nm of GaSb.

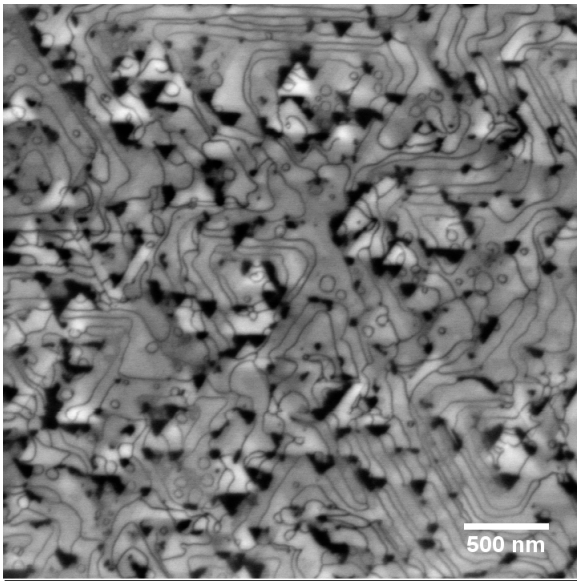

Figure 3.6: FE-SEM image of a ≈1.5 nm Sb sample with no cap. Sample was grown at a substrate temperature of 280°C. Dark spots are voids in the surface due to incomplete coverage. Dark lines running throughout are bilayer step edges of Sb.

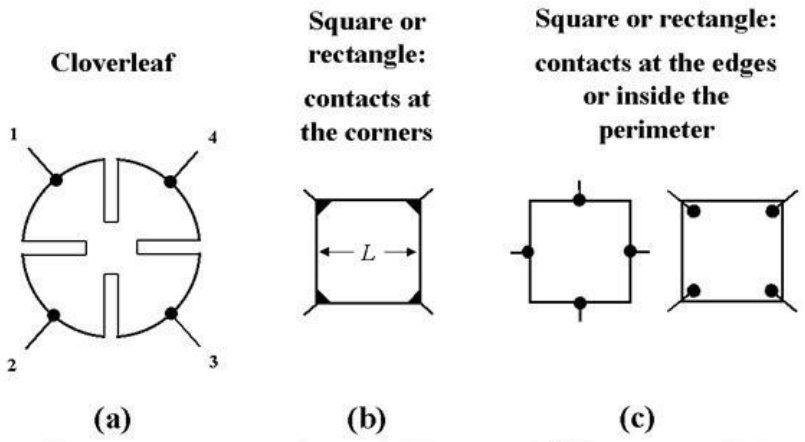

Figure 3.7: Various van der Pauw method geometries. a) Ideal cloverleaf geometry. b) Square sample geometry that allows for simplification of van der Pauw method. c) The bare minimum but not ideal geometry for application of the van der Pauw method. Image taken from Wikipedia.

range of temperatures from 300 K to 20 K using a closed cycle He-4 cryostat. Two point current-voltage measurements were made at 300, 77, and 20 K to test for the linearity of the contacts to ensure Ohmic contacts.

Aside-van Der Pauw method:

The van der Pauw method (VdP) [31] is widely used to determine sample resistivity, carrier density and mobility. The usefulness of this method is that it can be applied to a sample of any shape, so long that the sample is flat, of uniform thickness, solid (has no holes), homogeneous, isotropic, with contacts along the sample edge, and the area contacted is an order of magnitude smaller than the total sample area. When preparing samples there are a few geometries which are best suited (Figure **3.7**). The sample should have four ohmic contacts placed close to the edge boundary. The cloverleaf pattern in Figure **3.7**(a) is the ideal shape since it isolates the contacts from the sample. Square samples with contacts

placed in the corners as in Figure **3.7**(b) are an acceptable geometry, so long as the contacts are not far from the outside edge as in Figure **3.7**(c). The contacts should all be of the same material and the wires used for leads should be the same. A basic resistance measurement is made by applying a DC current between contacts 1-4 and measuring voltage from 2-3 (see Figure **3.7** for contact layout). The average resistance is the average of the measurements from along each sample edge. In the limit when the resistance along the vertical and horizontal edges are equivalent the sheet resistance of the sample is:

$$R_s = \frac{\pi}{\ln 2} R_{avg} \tag{3.1}$$

where R_s is the sheet resistance and R_{avg} is the average resistance. The VdP method allows you to make a measurement of the Hall effect in the sample. The Hall effect is a classical effect due to the Lorentz force causing charge separation in the sample[32]. For example, take a piece of material where electrons are the free carrier and a current, I, is applied in the +x direction (see Figure **3.8**) with the magnetic field, B, applied out of the page. The Lorentz force, F_B deflects electrons in the -y direction and they pile up along the bottom edge. This leaves an excess of positive ions along the top edge. This creates an internal electric field, E, in the -y direction which exerts a force, F_E, on the electrons that cancels out the Lorentz force. When this steady state situation is reached one can measure the Hall voltage, V_H, or transverse voltage due to the internal electric field. It can be shown (see 5 for calculation) that the Hall resistance $R_H = V_H/I = B/ne$, where n is the 2D carrier density and e is the electron charge. Therefore, from the slope of transverse resistance versus magnetic field plot one can calculate the 2D carrier density. In the VdP method, the Hall voltage can be measured by applying current from 1 to 3 and measuring voltage between 2 to 4. Note that

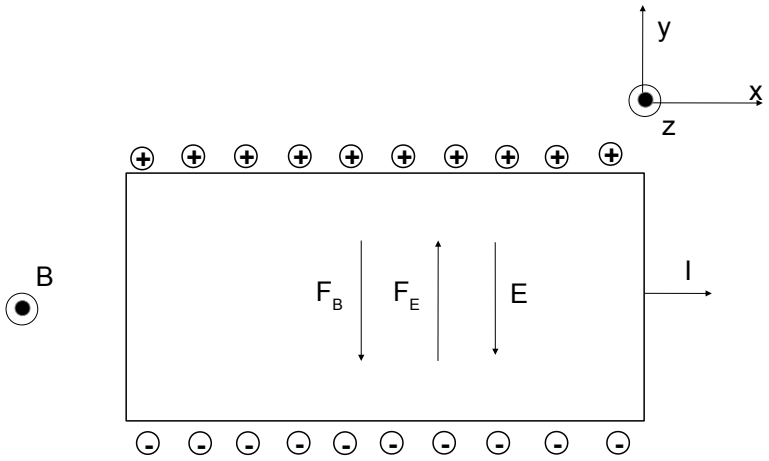

Figure 3.8: Graphical representation of the Hall effect for an electron doped sample. Current, I, is applied in the +x direction and magnetic field is applied out of the page. The Lorentz force, F_B, due to the magnetic field deflects electrons in the -y direction where they pile up along the bottom edge; this leaves excess positive ions along the top edge. This charge separation creates an internal electric field, E, which exerts a force, F_E, which cancels out the Lorentz force. In this steady state situation, the transverse voltage can be measured which is used in the calculation of the sample density. See text for more detail.

if there is a misalignment of the contacts, then when measuring the Hall voltage there will be a non-zero intercept due to mixing between the longitudinal and transverse resistance. This can be eliminated by subtracting the Hall voltage for a sweep up in positive field by the Hall voltage for sweep up in negative field (e.g. 0 to 8 T and then 0 to -8 T). Since the longitudinal resistance is symmetric about B=0 the vertical offset is removed, while the Hall resistance is anti-symmetric about B=0. Therefore you have to divide by a factor of 2 for double counting the Hall resistance. This can be represented by the following formula: $R_H(B\uparrow)$-$R_H(B\downarrow)=2R_{xy}$, where R_H is the Hall resistance, the B↑ is a sweep from to 0 to positive field, B↓ is a sweep from 0 to negative field, and R_{xy} is the transverse resistance. Note that the absolute value of positive and negative field must be equivalent. With knowledge of the sheet resistance and carrier density, n_s, the mobility, μ, is calculated from the Drude model:

$$\mu = \frac{1}{en_sR_s} \tag{3.2}$$

with e being the elementary charge.

In Figure **3.9**, the sheet resistance vs temperature for seven samples is shown. All of these samples were grown at a substrate temperature of 280°C. Wells of 20-40 s growth time show metallic-like behavior ($\frac{dR}{dT} > 0$) as a function of temperature, while the 15 and 10 s wells show insulating behavior($\frac{dR}{dT} < 0$). To determine whether we are measuring the Sb layer or other parallel layers, we compared the resistance of the samples in Figure **3.9** to that of a GaSb buffer layer. The GaSb buffer layer at 20 K had a sheet resistance of $8.1\text{x}10^3\,\Omega/\square$, extrapolating to the GaSb cap layer (average thickness 10 nm) we would predict a sheet resistance of $8.1\text{x}10^5\,\Omega/\square$. Both GaSb layer resistances are larger than what is measured for

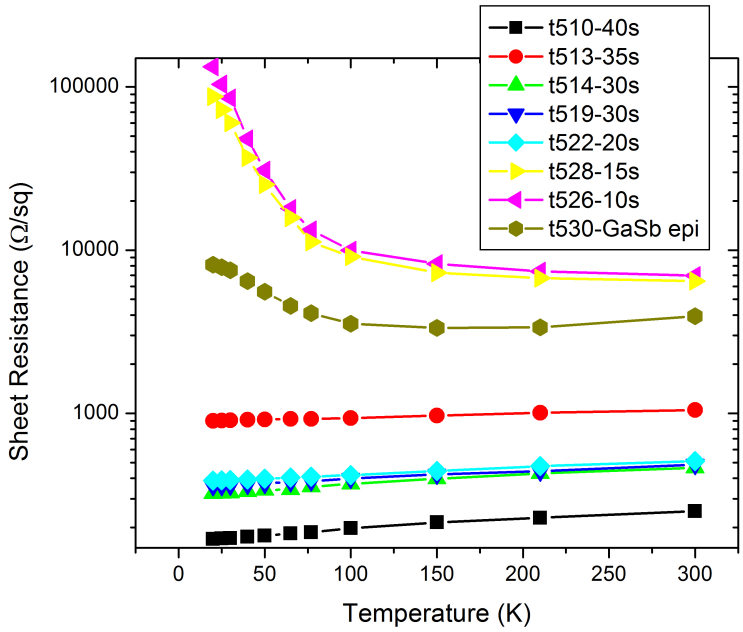

Figure 3.9: Plot of sheet resistance vs temperature for seven different growth times of Sb wells . All wells plotted above were grown at a substrate temperature 280°. For wells grown longer than 20 s we see metallic like behavior while below 20 s insulating behavior is observed. There was a lack of reproducibility as seen by the well grown for 35 s which should have a smaller resistance compared wells grown for 20 s. Instead the 35 s well is more resistive than wells that are expected to be thinner. The transition between insulating and metallic behavior could be due to a metal-insulator transition or a possible percolation transition. This is investigated using surface SEM studies covered in a later section.

the 20-40 s samples indicating that the Sb layer is the main channel of conduction for these samples. The 15 and 10 s samples have resistances on the order of the GaSb layers indicating a different conduction process. In these thinner wells, the increase in resistance as a function of temperature is an indication of a possible percolation transition[33] due to incomplete Sb coverage. This is confirmed when looking at the surface using FE-SEM (Figure **3.6**), showing voids in the Sb layer. Due to the large lattice mismatch between the GaAs substrate and the GaSb buffer layer and to improve the quality of our wells we decided to change from growing on GaAs(111) substrates to the more natural selection of GaSb(111) substrates.

3.1.1 Surface SEM study

To discover the origin of the transition from metallic to insulating behavior observed in Figure **3.9** a surface SEM study was done on three different samples. The GaSb epilayer (Figure **3.10**(a)) shows voids (dark spots) which are due to the lattice mismatch between the GaSb epilayer and the GaAs substrate. Then the quality of an un-capped and capped 15 s growth time sample was studied. To see if these voids propagate through the subsequent layers, a surface SEM was done on a capped (Figure **3.10**(b)) and un-capped (Figure **3.10**(c)) sample. Both of these samples show that the voids do propagate through to the active layers and that growing on GaAs substrates does not produce high quality wells. To counter this lattice mismatch, wells were instead grown on n-GaSb(111) substrates from three different manufacturers.

3.2 Sb on GaSb(111) substrates

Growth on the GaSb(111) substrates follows a very similar growth stack to that of the GaAs(111) substrate growths (Figure **3.2**), with a substitution of the GaSb(111) for GaAs(111). An important distinction between the two substrates is that the GaAs substrates are semi-insulating while the GaSb substrates are n-type (Te) doped.

In Figure **3.11** we have FE-SEM images of both GaSb buffer layers on the different substrates. The GaSb buffer layer on GaSb substrate shows more ordered growth with fewer defects compared to the GaSb buffer on GaAs. For the series grown on GaSb substrates, three different manufacturer substrates were used: Wafer Tech, New Way Semiconductor, and Galaxy Wafer. All samples for the GaSb substrates were grown using the fixed temperature substrate method.

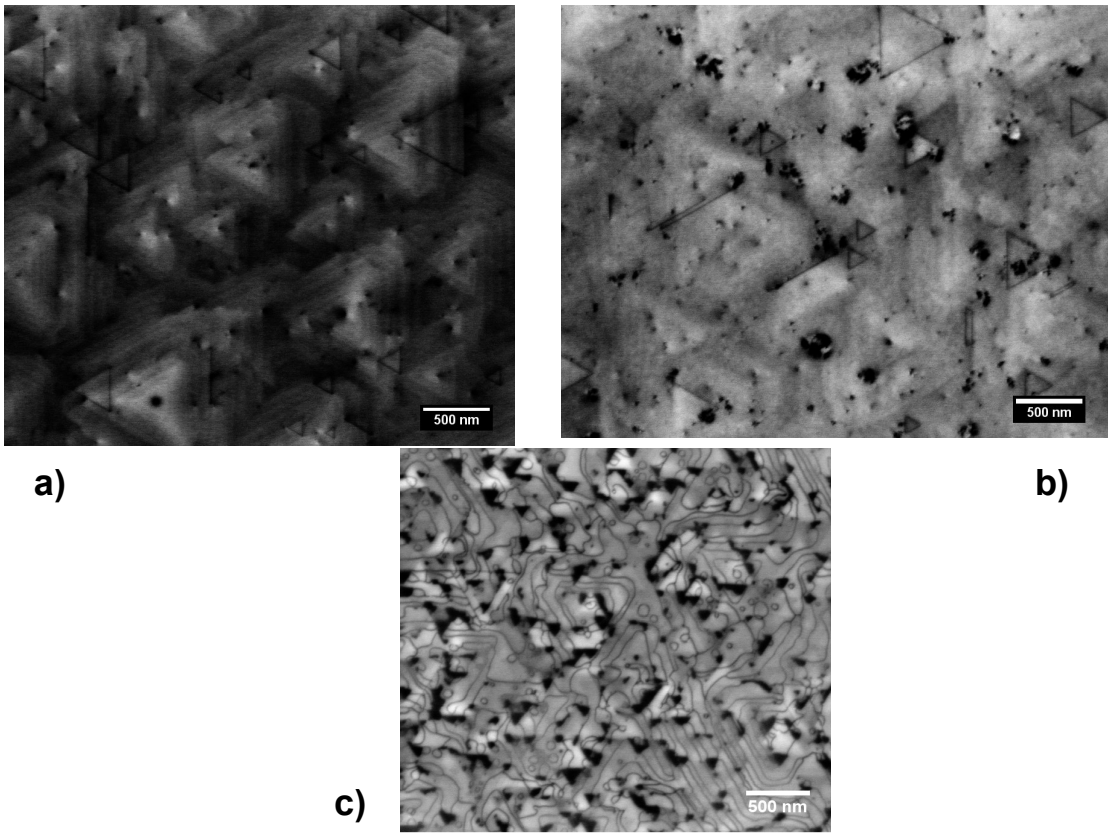

Figure 3.10: Surface SEM images captured using a back scatter detector. a) Surface SEM image for a GaSb epilayer grown on GaAs(111) substrate. Voids (dark spots) in the epilayer are due to the large lattice mismatch between the substrate and grown layer. b) Surface SEM for a capped 15 s growth time Sb well showing voids that originate from the underlying structure. This is also true a uncapped sample shown in c) of the same growth time.

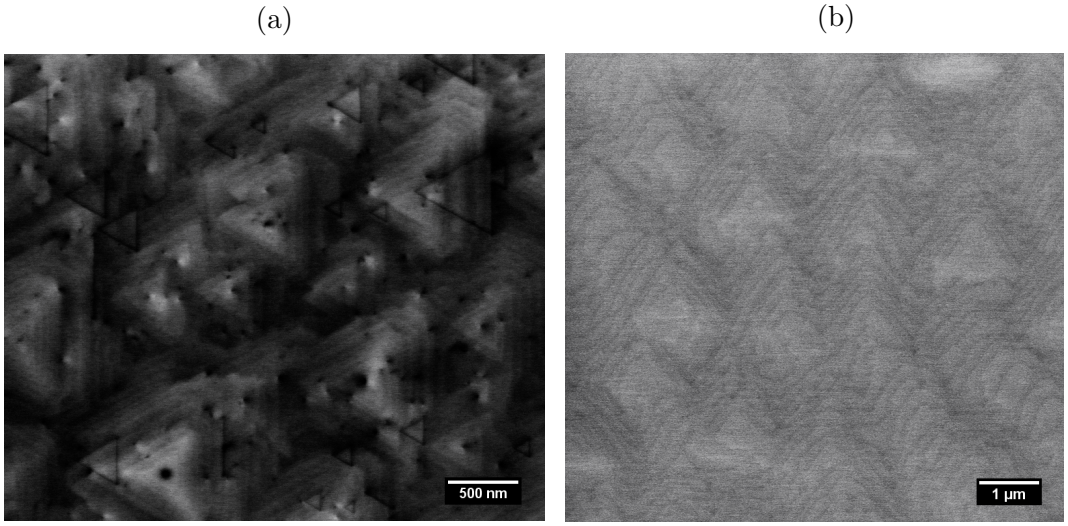

Figure 3.11: FE-SEM images of GaSb buffer layers grown on two different substrates. (a) GaSb buffer layer grown on GaAs(111) substrate showing point defects coming from lattice mismatch. (b) GaSb buffer layer grown on GaSb(111) substrate showing well ordered structure with no point defects.

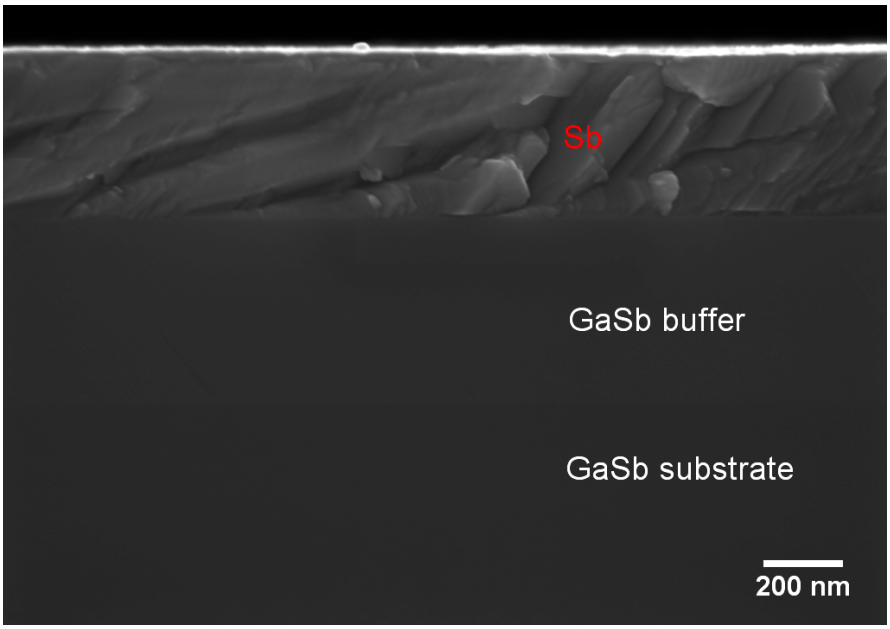

Figure 3.12: Cross-sectional FE-SEM image of a thick Sb layer used for growth rate calibration on GaSb substrates. Roughness of Sb layer comes from cleaving sample along a natural cleavage plane for the GaSb substrate but not for the Sb layer.

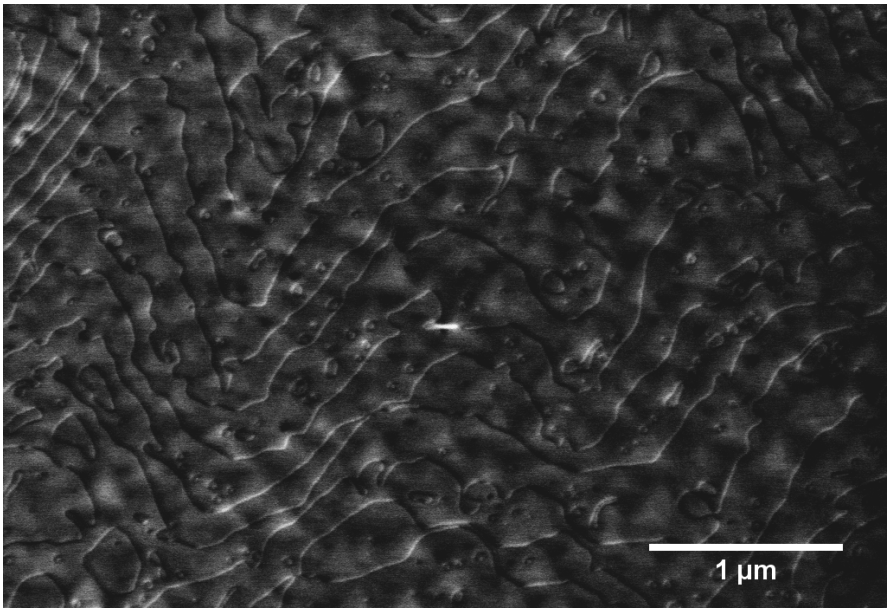

Figure 3.13: Plan-view FE-SEM image for ≈3.6 nm Sb well showing a continuous layer with bilayer steps grown on a GaSb(111) substrate.

The first series of samples (Aug 2012-Nov 2012) were grown on Wafer Tech substrates, but due to a limited supply of substrates a new supplier was sought. The second series of samples (Nov 2012-Oct 2013) was then grown on substrates from New Way semiconductor. Physical and electrical characterization on eight different growths showed poor quality wells. The GaSb epilayer was then compared to growths on Wafer Tech substrates, to compare the growths on the different substrates. Figure **3.14** shows the sheet resistance as a function of temperature for GaSb epilayers on the three different substrates. GaSb epilayers on Wafer Tech and Galaxy Wafer show insulating behavior as expected for good quality semi-conducting GaSb. While epilayer grown on New Way semiconductor shows metallic behavior due to a large amount of defects in the substrate. We then transitioned to growing Sb wells (Nov 2013-Feb 2014) on the remaining Wafer tech substrates. These substrates were then replaced by substrates from Galaxy Wafer for the most current growths (Feb 2014-present).

We expect transport measurements to show samples grown on GaSb substrates

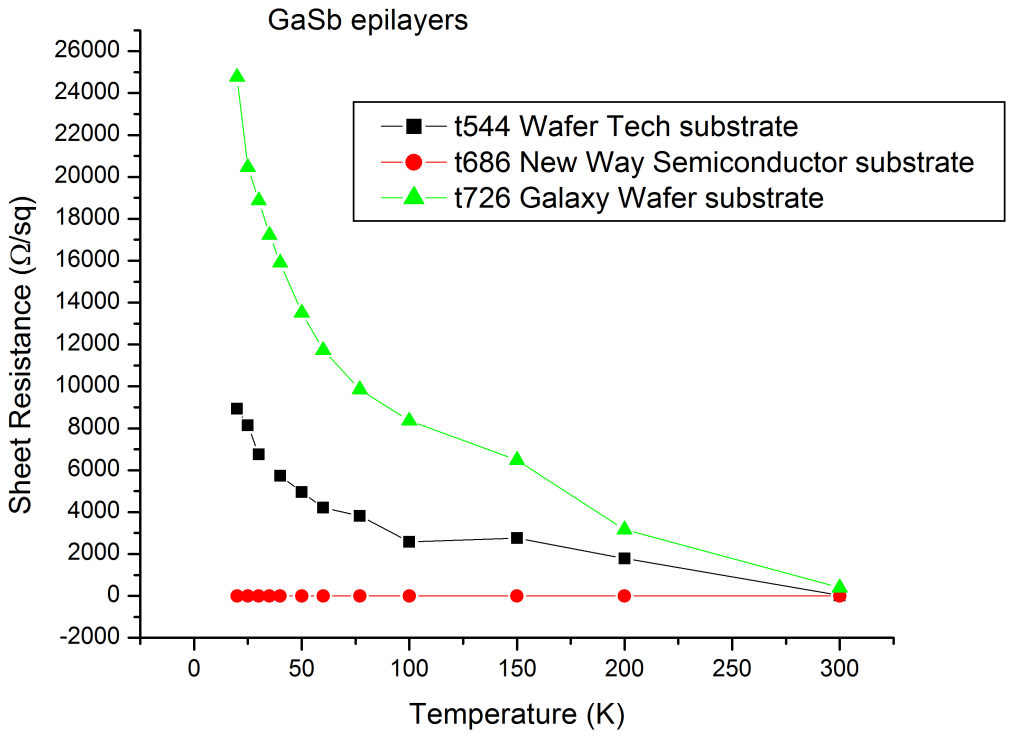

Figure 3.14: Plot of sheet resistance vs temperature for three different GaSb epilayers. The epilayers were grown on substrates from different manufacturers. For Wafer Tech and Galaxy Wafer substrates, the GaSb epilayer shows insulating behavior as expected for the semi-conducting GaSb. While on the New Way Semiconductor substrate the GaSb epilayer shows metallic behavior. This is unacceptable because the subsequent Sb well needs to be grown on a insulating layer such that the Sb well dominates the conduction.

to have a lower resistance since the formation of defect states is reduced. Surprisingly transport measurements on both samples at 20 K show comparable resistance (8100 Ω/□ for GaAs vs 8900 Ω/□ for GaSb). This could be due to that while the GaAs substrate is semi-insulating the GaSb substrate is n-type doped. The GaSb buffer layer while being undoped, ends up unintentionally p-type. This comes from Ga vacancies that occur during growth[34]. Therefore we form a p-n junction at the interface of the n-type GaSb substrate and p-type GaSb buffer. This p-n junctions forms a potential barrier preventing the flow of electrons into the substrate, therefore causing an increase in the resistance of the sample.

After establishing optimum growth conditions on GaSb(111) substrates we grew a series of wells for a range of thicknesses from 1.8 to 5.4 nm (≈16 samples). Some wells were left uncapped for surface studies. To make sure the growth calibration did not change when switching substrates, we grew thick Sb layers (>100 nm) and measured their thickness by cross-sectional FE-SEM (Figure **3.12**). The growth rate (1.8 Å/s) was higher than the previous growth rate (1.0 Å/s) on GaAs substrates. This is most likely to due to the lower growth temperature of 180° C on GaSb(111) compared to 280° C on GaAs(111) substrate. Figure **3.13** is a sample representative plan-view FE-SEM image using a backscatter detector showing Sb bi-layer steps.

3.3 Summary

Sb quantum wells were grown on type types of substrates: GaAs(111) and GaSb(111). Over the approximately 30 samples grown on GaAs substrates two main results can be concluded. For wells grown at the lowest substrate temperature, 280° C, which should correspond to the best quality showed a lack in reproducibility and a propagation of voids due to the lattice mismatch between the

GaAs substrate and GaSb buffer layer. Wells were then grown on GaSb substrates which showed improved quality of buffer layer and therefore better well quality; although, growth quality of Sb quantum wells on GaSb substrates depended on the substrate manufacturer.

Chapter 4

Processing of Sb samples into devices

One of the simplest devices we fabricate is a Hall bar (Figure **4.1**). The resistance for a Hall bar can be expressed in units of Ohms per square, $R_{\square}$, using the following equation:

$$R_{\square} = R \times (\frac{W}{L}) \tag{4.1}$$

where R is the measured resistance, L is the distance between the center of the voltage probes, and W is the width of the Hall bar. The Hall bar design has certain advantages over van der Pauw (VdP) samples. While the VdP method involves minimal sample prep, the Hall bar geometries typically yield multiple devices from a comparably sized wafer. Additionally, a Hall bar has well defined probes which allow for multiple measurements across one device of both the longitudinal resistance, R_{xx}, and transverse resistance, R_{xy}, providing contact redundancy, which is lacking in a van der Pauw configuration. When measuring R_{xy} with a Hall bar, there is relatively little mixing of R_{xx} into the signal since the probes are lithographically defined as opposed to being applied by hand as with VdP samples.

Processing samples into Hall bar devices requires photolithography, etching, and metal deposition. Photolithgraphy (Figure **4.2**) is the process of using light to expose a photosensitive resist through a photo-mask to define device patterns. After exposure the sample is developed to resolve the desired pattern. This pattern is then etched into the sample either using either a chemical wet etch or dry etch. Once the mesa pattern has been defined another layer of photolithography is done to define contact pads. A metal contact can then be deposited through a multitude of thin film deposition techniques (e.g. thermal evaporation, sputtering, electron

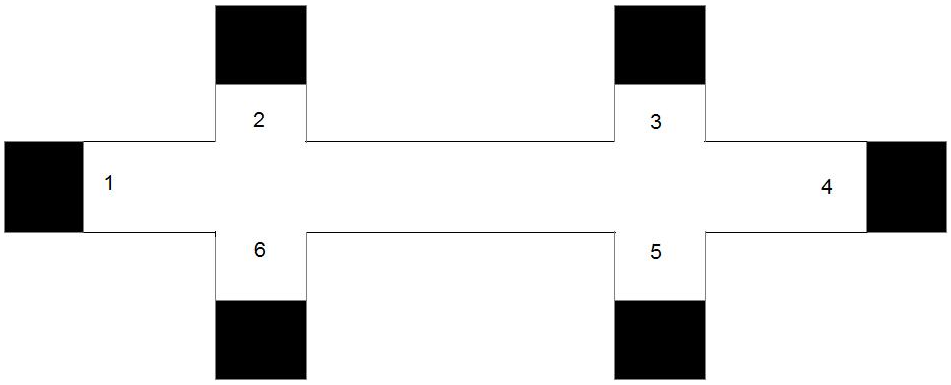

Figure 4.1: Schematic of a Hall bar design. For measurement of longitudinal resistance (R_{xx}), current is applied from 1 to 4 and voltage can be measured from either 2 to 3 or 6 to 5. For measurement of transverse resistance (R_{xy}), current is applied form 1 to 4 and voltage measured from either 6 to 2 or 5 to 3. For a constant current measurement, resistance can be calculated using Ohm's law: R = V/I

beam deposition, etc.). Our standard processing steps are detailed below.

4.1 Standard Processing Steps

Samples for processing are cut from MBE grown quarter wafer with an average sample size of 8 x 8 mm. This size is chosen to maximize the number of Hall bar devices per a sample and meets the minimum size for the spin coater. To cut samples from wafers, a diamond scribe is used for easy cleaving. A dry nitrogen air gun is used to blow away dust particles produced during scribing and cleaving. Both photolithography and etching are prepared inside a class 1000 clean-room. The sample is pre-cleaned with acetone, methanol, and isopropyl in a ultrasonic bath for 5 mins each. The sample is blown dry with nitrogen and placed in a oven at 150°C for 10 mins to evaporate any remaining pre-clean solvents. The sample is then allowed to cool before being place inside a Laurell spinner for photo-resist (PR) application. The PR is spun on at 4000 RPM for 40 seconds to achieve an approximate film thickness of 1.4 μm (per manufacturer). We use AZ 5214E image

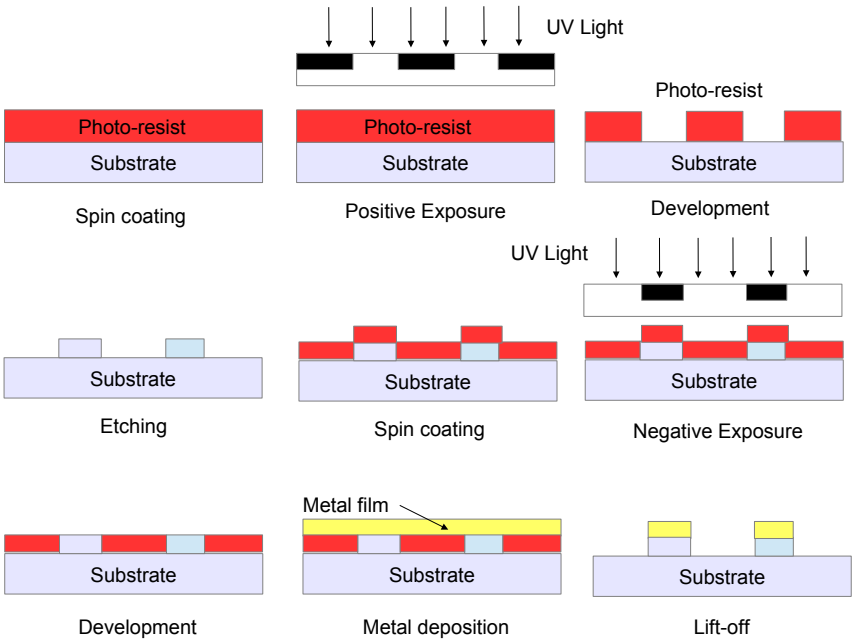

Figure 4.2: Outline of the steps in photolithography. The substrate is spin coated with photo-resist (PR). A photomask of the mesa pattern is brought into alignment over the substrate and the PR is exposed using UV light. The pattern is then developed to removed exposed resist from positive exposure. The mesa is etched into the substrate. Another layer of PR is spin coated onto the etched substrate. A photomask with contact features is aligned to the mesa and a negative exposure is performed. After development, all unexposed areas are removed. A metal film is deposited for Ohmic contacts which is removed using lift-off leaving behind metal contacts.

reversal PR, which can be used as either a positive or negative resist depending on the application need. After resist spinning the sample is pre-baked at 95°C on a hot plate to evaporate the remaining resist solvent. The sample is now ready for exposure.

A positive exposure will result in the removal of all exposed resist when developed, whereas negative exposure will result in the removal of all unexposed resist. For defining the Hall bar mesa we use a positive exposure. Using a Karl-Suss MJB-3 mask aligner the PR is exposed for 6.5 seconds with a 275 W Hg arc-lamp. The sample is then developed in either Shipley MF-319 or AZ 1:1 developer for

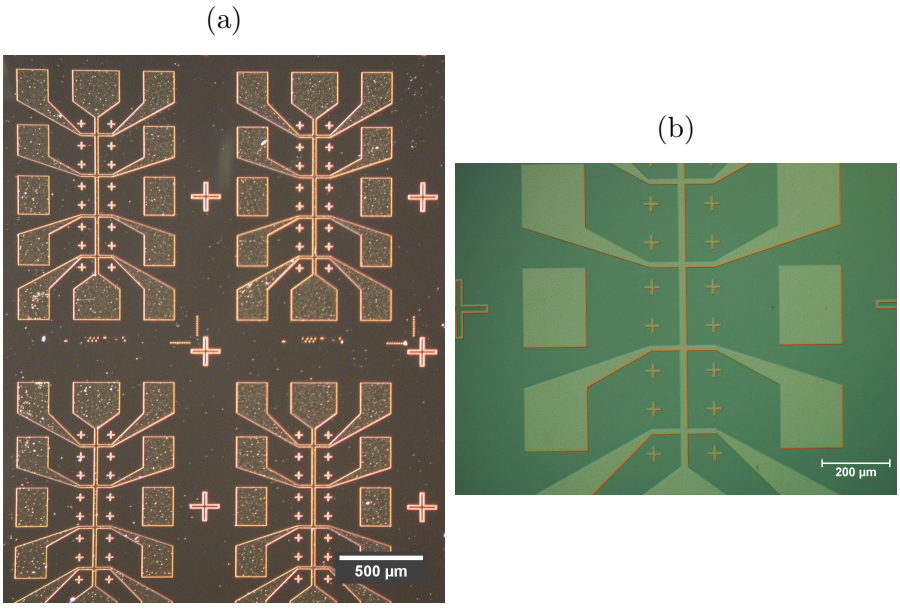

Figure 4.3: (a) Optical image of etched Hall bars on a Sb sample. The crosses are alignment marks for the contact mask. The smaller marks near the center of the Hall bar channel are used for electron beam lithography (EBL). (b) Close-up image of one the Hall bars showing the small EBL alignment crosses.

60 s. The Hall bar mesa is wet etched into the sample using a aqueous solution of hydrogen-peroxide, hydrofluoric acid, lactic acid. The etching solution is a 6:3:1 mixture by volume of 3% H_2O_2: 2.5% HF : 85% Lactic Acid. A detailed recipe can be found in Appendix A. The remaining PR is removed with Shipley 1165 remover, which leaves behind the Hall bar mesa(Figure **4.3**).

A second layer of negative photolithography is used to define contacts where the same steps as before are followed with two additional steps. After a shortened first exposure of 2.5 secs, there is an image-reversal bake for 1.5 mins at 150°C to convert the PR into a negative resist. This is then followed by a flood exposure for 50 seconds before development. Indium is used as the contact metal and a 100 nm layer is deposited using an Edwards thermal evaporator. The remaining In is removed in lift-off with Shipley 1165 PR remover.

A Tempress scriber is used to mark and cleave out individual or multiple

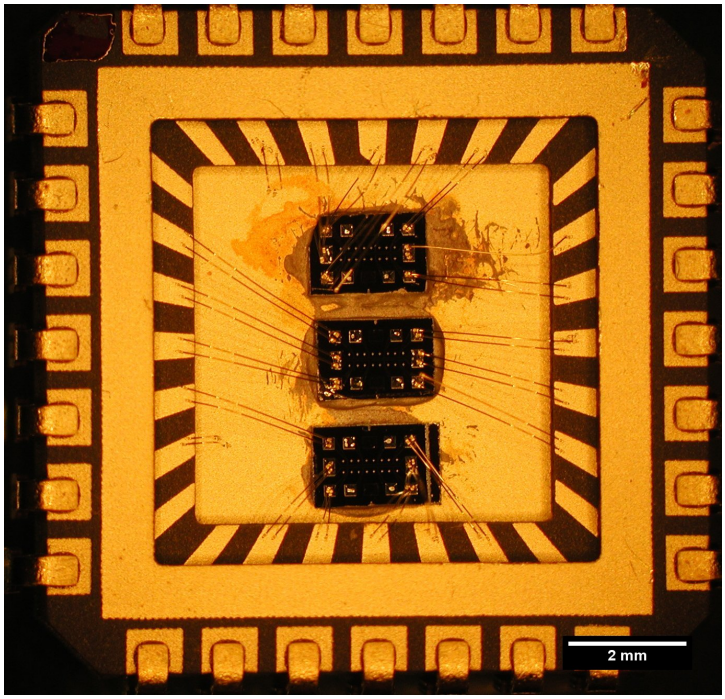

Figure 4.4: Completed Hall bar devices mounted in a PLCC socket for use in a He-4 fridge here at the university. The samples are mounted using Ted-Pella silver paste. Hall bars are cleaved from a larger piece using a Tempress scriber. The wires are applied using a K&S semi-automatic wedge bonder.

Hall bar devices. The devices are then mounted on a low temperature sample holder and wire bonded using a K&S 4523 wedge bonder. Figure **4.4** shows three completed Hall bar devices. Recipe for standard processing can be found in Appendix B.

4.2 Problems and Solutions with standard processing on Sb

Unfortunately our processing on the initial series of Sb was unsuccessful. All the devices had a significantly larger resistance at 77 K then previously measured on the unprocessed VdP samples. This was unexpected. We performed a systematic A/B failure analysis on Sb samples for every step of the photolithography

process and were able to determine that the developer was the culprit.

Developers for photolithography can be split into two different categories, organic (metal ion free) and inorganic (metal ion containing). The active component in organic developer is tetramthylammonium hydroxide (TMAH), while the active component of inorganic developer can be potassium hydroxide (KOH) or sodium hydroxide (NaOH). Microposit 351 (inorganic), AZ Developer 1:1 (inorganic), and Microposit MF319 (organic) are all compatible with the AZ5214E photo-resist. Samples from the same wafer and of similar size were used for testing. A different piece was soaked in a given developer for 60 s to match the time from standard processing. The resistance of each at 77 K was then compared with each other and a unprocessed control sample. The control sample had a resistance of $97\,\Omega$ while the three processed samples showed an increase in resistance ranging from $813\,\Omega$ to $1933\,\Omega$ rendering all three developers unacceptable for standard use.

4.2.1 Further Investigation

One possibility was that the developer was changing the surface chemistry of the Sb through oxidation. A well known side effect common to both types of developers is that they etch aluminum and aluminum alloys[35]. To determine if this was happening for the GaSb capped Sb samples, we took a sample with a 4 nm Sb layer and 10 nm GaSb cap and performed a negative exposure of the contact areas. The sample was then developed for 3 mins, much longer than the 1 min used in the standard procedure, to insure that we could observe etching if present. After development the photo-resist was removed and any remaining etched features were measured using a Ambios XP-2 profilometer. An optical image of the etched features is shown in Figure **4.5** clearly revealing etching. Multiple measurements were made across different steps and locations to determine an average sample

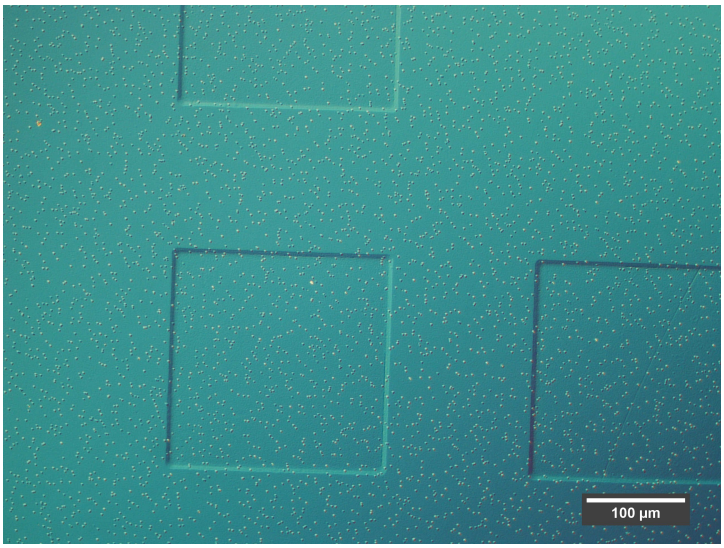

Figure 4.5: Etched features in a Sb sample after exposure to developer for 3 minutes. The depth of the features were measured using a profilometer. The coloring in the image is due to a Nomarski differential interference contrast (DIC) insert.

etch depth which was determined to be 27.4 nm for 3 mins yielding an etch rate of about 10 nm/min. To avoid etching the active area of the device, a modification of the standard photolithography process was required.

4.2.2 Revised Photolithography Process

Only one step of the process required modification, as during the mesa step, the channel and leads are protected by photo-resist during development. In the contact step however, a negative exposure opens windows over the contact areas for subsequent metal deposition. This meant that the contacts were exposed to the developer which damaged the underlying Sb layer. To define contact areas without exposure to the developer, we fabricated a Kapton shadow mask (Figure **4.6**) to deposit indium. We used a size $\#80 (343\,\mu\text{m})$ drill bit and a CNC (computer numerical control) milling machine to accurately drill holes into the Kapton mask. This allowed us to evaporate indium contacts onto the sample without using

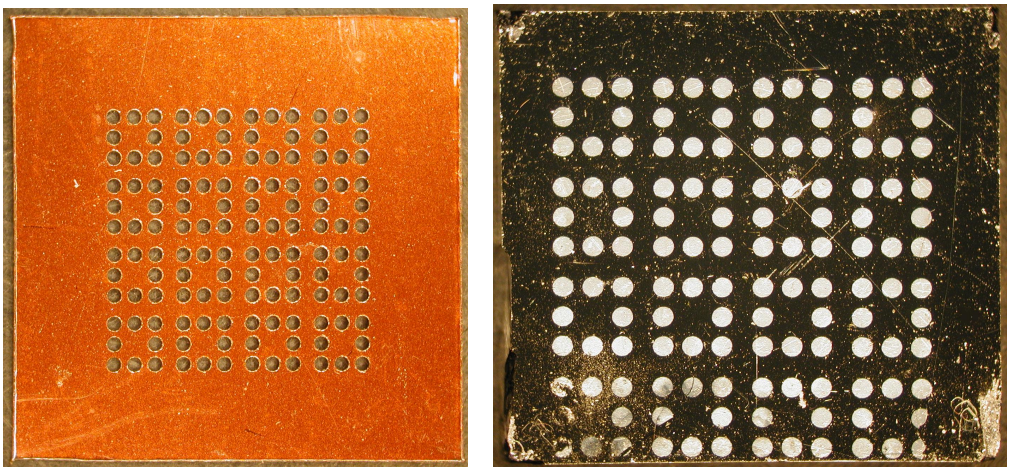

Figure 4.6: **Left**: Picture of Kapton contact shadow mask after milling. **Right**: Indium contacts after deposition using thermal evaporator. Kapton shadow mask is mounted above the sample on posts and kept in place using PR as adhesive.

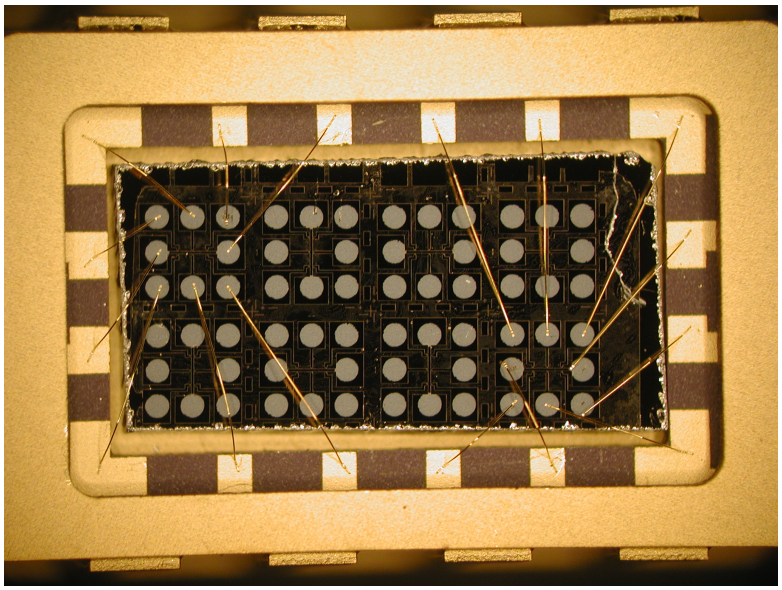

Figure 4.7: Completed section of Hall bars cleaved from a larger processing piece. Hall bars are mounted inside the header using silver paste. The header used here is for a different He-3/4 fridge located at the National High Magnetic Field Laboratory (NHMFL).

photolithography. To keep the mask in place during metal deposition, we used PR to adhere the mask to posts that would keep the mask above the sample without damaging the surface. We also modified the step sequence to deposit contacts first and then define the mesa so as to avoid a more complicated alignment procedure if the steps were in the typical order. A completed sample using the revised method can be seen in Figure **4.7**. The revised recipe can be found in Appendix C. Subsequently after 6-8 months of using the revised photolithography recipe we then grew samples with a thicker GaSb cap (40 nm versus the original 10 nm cap) to provide sufficient protection from the developer. This was not done earlier in the growth history due to concerns about not being able to contact the Sb well with un-annealed contacts. Once a thicker capped sample was grown we were able to compare the temperature dependence of the resistance to a sample of equivalent well thickness with a thinner cap, which showed little difference. Indicating that the thicker cap was not preventing the contacts from reaching the Sb well. The thicker cap provided sufficient etch protection for the Sb layer such that we could return to the standard processing procedure.

4.3 Nano-wire devices

Studies of universal conductance fluctuations are also covered in this dissertation. This occurs on very small length scales. In order to probe this physics we designed and fabricated nano-wire devices (NWDs). The NWDs must have dimensions on the order of the phase breaking length to allows us to probe the quantum interference properties. These devices were fabricated using electron beam lithography (EBL) and reactive ion etching (RIE).

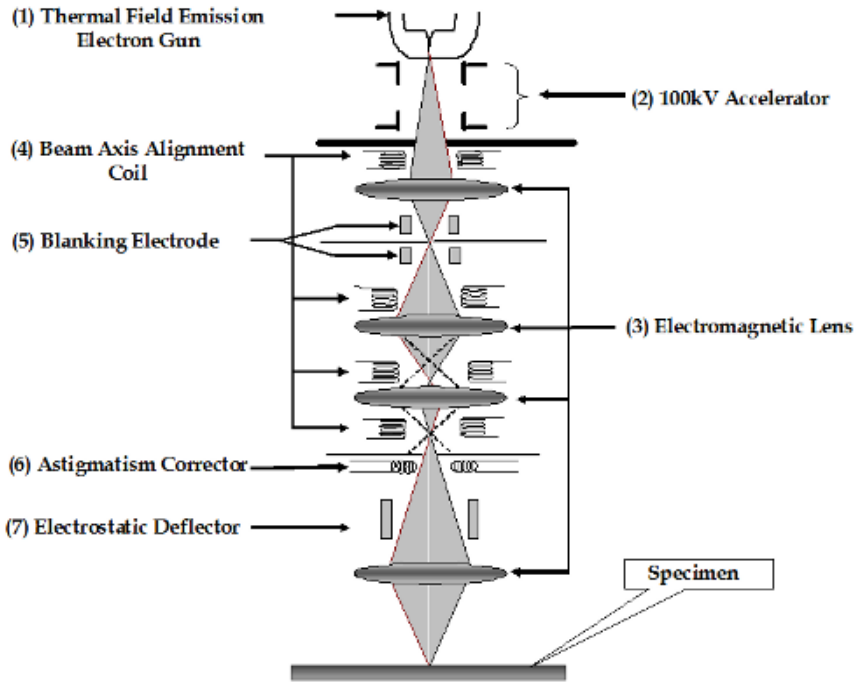

Figure 4.8: Diagram of SEM column. At the top of the diagram a electron gun produces electrons which are accelerated through a high voltage potential. The beam axis alignment coil is used to center the electron beam along the beam axis. The blanking electrode is used to blank the beam before and after writing in EBL. Electromagnetic lenses are used for collimating and focusing the beam as is passes through beam axis and the astigmatism corrector is used to correct the oblongness of the beam spot. The electrostatic deflector (or scanning coils) is used to deflect the beam for imaging and writing patterns. Figure taken from [8].

4.3.1 Electron-beam lithography

EBL is a technique used to create nanometer size structures that are not possible with due to the diffraction limit of optical photolithography techniques. In EBL, an electron beam is used to expose electron beam (e-beam) resist that is sensitive to electrons in contrast to photoresist which is sensitive to photons. The SEM used for EBL in this study is a JEOL 840A equipped with a tungsten filament that thermally generates electrons. Those free electrons are accelerated through 30 kV towards the sample. The beam is then collimated by electromagnetic lenses (similar to a solenoid) and a set of deflection (scanning) coils allows for movement

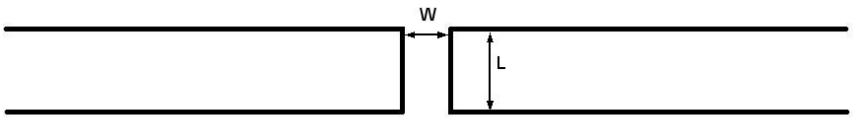

Figure 4.9: Drawing of the NWD. The narrow constriction with width, W, and length, L, is placed in the middle of the Hall bar channel. Both W and L are varied to probe the different length scales of quantum interference effects.

of the beam over the sample surface. Our standard SEM alignment procedure produces a well stigmated beam spot ranging from 100 to 150 nm in diameter depending on the beam current used.

The SEM is interfaced with a nanometer pattern generation system (NPGS) which includes a computer aided design (CAD) software, DesignCAD Express, used for pattern designing. The NPGS systems automates the pattern writing by remotely controlling the electron beam's position. In EBL the beam is used for both imaging and writing, therefore to protect the areas where one wants to pattern, an electronic beam blanker is used before and after writing. This allows for alignment of the electron beam over non-important areas then the beam can be blanked and moved into position for writing. A detailed EBL procedure can be found in Appendix D.

4.3.2 Dose Testing

Figure **4.9** shows the NWD to be patterned in the middle of the Hall bar channel. The dark lines represent a trench etched into the channel, electrically isolating the channel current. The Hall bar sample is prepped by cleaning the surface using an ultrasonic bath of acetone and isopropyl for 5 mins and dehydration bake at 150°C for 10 mins. We use ZEP520A e-beam resist for EBL. The resist is spun on at 5000 RPM for 45 seconds; resulting in a resist film of about 325 nm. To pattern the NWDs into the Hall bar channel we use the line dose setting of the

NPGS. Before our NWD fabrication, we performed a dose test to find the optimal dose to clear the e-beam resist and give the best resolution. Our dose test pattern is shown in Figure **4.9** a series of boxes, separated by 0.1, 0.2, 0.3, 0.4, 0.5, 1, 2, 3, 4, and 5 μm.

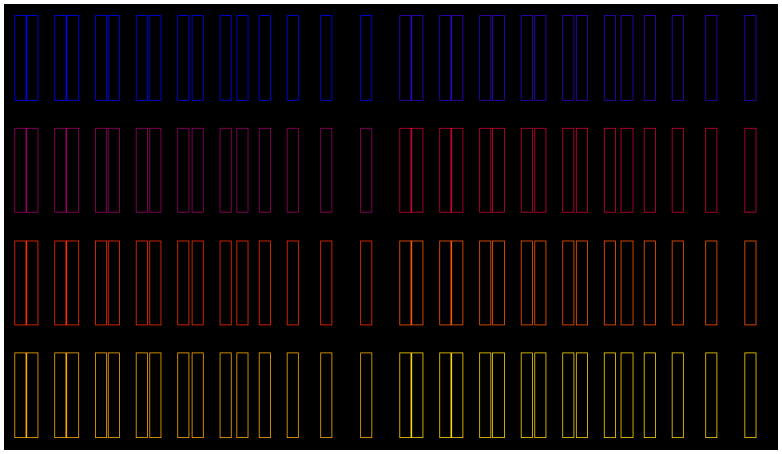

(a)

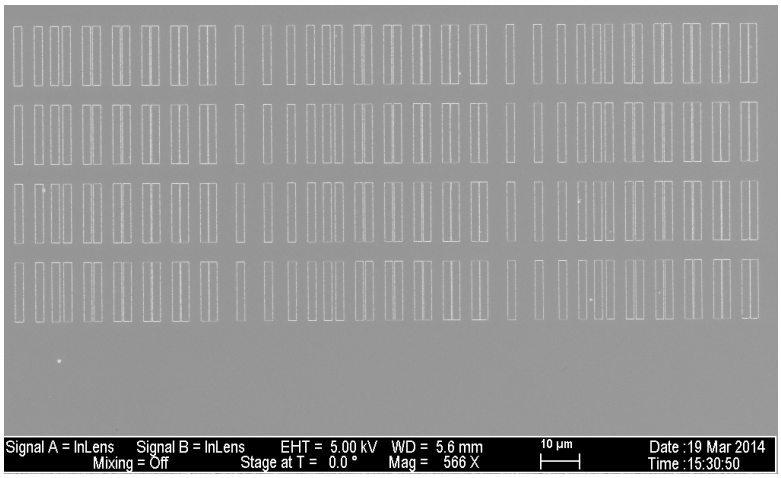

(b)

Figure 4.10: (a) Screen shot of line dose pattern from Design CAD Express. Different colors correspond to different values of line dose. (b) SEM image of a set of written line doses with indium deposited for imaging contrast.

Figure **4.10**(a) shows a screen shot of the CAD drawing for the dose test. A different line dose in units of nC/cm is associated with each different color. Depending on the beam current, the NPGS software will calculate the appropriate

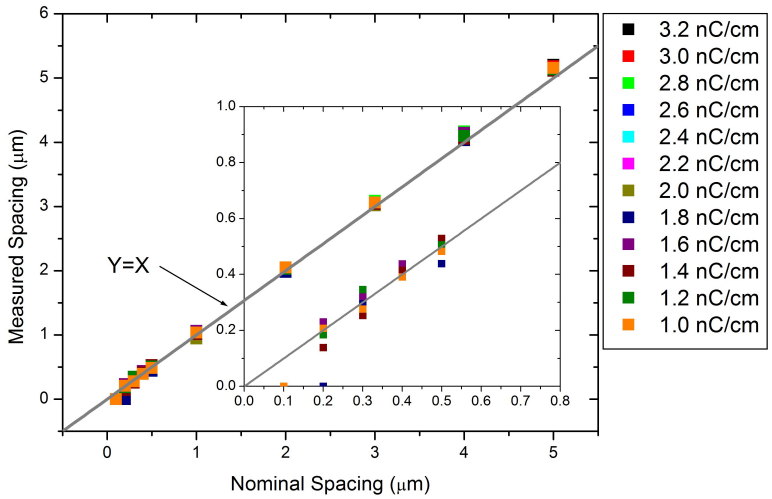

Figure 4.11: Plot of measured separation between features vs. nominal spacing for a range of doses from 1.0 nC/cm to 3.2 nC/cm. The grey line, Y=X, is for the ideal situation of patterning. Inset is close up view of the the measured spacings for nominal widths less than 1 μm. For large nominal spacings very little variation is seen in the measured width, while at the smaller nominal spacings there is a larger variation of about 15%. Variability in measured spacing is due to inaccuracies in where one measures the small separations.

beam dwell time to produce the desired dose.

Figure **4.10**(b) shows a line dose sample which has been developed in Xylenes for 45 secs with indium deposited to provide image contrast. Clarity of the lines indicates that the e-beam dose was high enough to clear the e-beam resist and allow indium to deposit. The set of outlined boxes is repeated in a 4 x 3 array starting with the lowest dose (1.0 nC/cm) in the upper-left and moving left to right; ending with the highest dose (3.2 nC/cm) in the lower-right. The measured separations between the features for each set of line doses is plotted in Figure **4.11**. We compare the measured separation to the nominal separation where the ideal case is plotted for Y=X. Points below the ideal line are overexposed resulting in a smaller measured width. Points above the ideal line are underexposed resulting in either the resist not completely clearing or making features are hard to resolve. At large feature size ($> 1\,\mu$m) the measured separation is insensitive over the range of

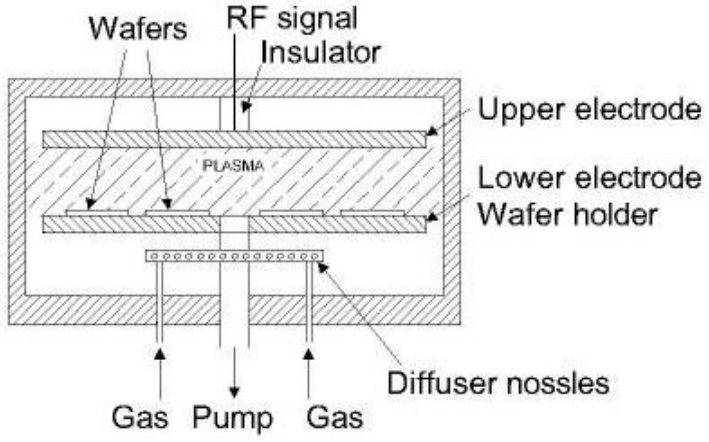

Figure 4.12: Diagram of the RIE chamber. The lower electrode serves as the wafer holder. Gas is pumped into the chamber at a fixed flow rate measured in sccm. The chamber is pumped on to maintain an appropriate vacuum($1x10^{-6}$ Torr for our system). The RF signal is applied between the electrodes to produce a plasma used for etching. The stage and power supplies are cooled by either water or water/ethylene-glycol mixture. Figure taken from https://www.mems-exchange.org/MEMS/processes/etch.html.

line doses studied. For smaller feature size ($< 1\,\mu$m) the separation was sensitive to line dose value. Combining results from a total of three tests for reproducibility, optimum dose was 2.2 nC/cm. This provided good resolution and the ability to clear the resist, which can have a variable thickness depending on the age of the decanted resist. After an appropriate dose is determined the NWD patterns are then etched into the sample forming a device.

4.3.3 Reactive ion etching

In photolithgraphy, it is often sufficient to use wet etching, however the NWDs have features smaller than a micron, wet etching is not used. Rather reactive ion etching (RIE) which etches anisotropically allows us to etch our pattern without the risk of undercutting.

An RIE machine consists of a vacuum chamber and a pair of parallel plates,

where a wafer plate (or stage) forms the bottom plate (See Figure **4.12**). The wafer plate is electrically isolated from the surrounding chamber. There are inlets for the gases used to etch the sample, which have adjustable flow rates in sccm (standard cubic centimeters per a minute). To maintain system pressure of a few mTorr during etching the system is backed by a turbo pump. The gases used depend on the material chemistry, for example boron trichloride (BCl_3) is the main gas used to etch our Sb samples. The RIE used in this study includes a inductively coupled plasma (ICP) unit which provides a high density source of ions to achieve faster etch rates. A large RF power, a few hundred watts, is applied to the plate which ionizes the incoming gas molecules and produces a plasma.

Electrons that were stripped from the gas to produce the plasma are fed out to ground as they collide with the chamber walls. This causes the plasma to be overall positive due to the larger density of positive ions compared to the free electrons in the chamber. The wafer plate though is electrically isolated and will start to build up a negative charge. A potential difference will form between the positive gas ions and the negative wafer plate, on the order of a few hundred volts, accelerating the ions into the sample for etching. The ions react chemically with the surface of the sample, but a small amount of sputtering can occur. This vertical interaction of the ions produces the anisotropic etch profile. RIE though is very sensitive to systematic parameters such as chamber pressure, gas flow rate, RIE and ICP power.

Etching Sb samples in the RIE is a two step process. Before the Sb is etched, an O_2 descum is performed to remove any surface contaminants. The O_2 flow rate is set to 50 sccm with the RIE and ICP powers set to 40 and 100 W for 30 s while the chamber is maintained at 25 mTorr. Following the descum is the main etching step which uses a mixture of BCl_3 and Ar. The BCl_3 and Ar are kept at

flow rates of four and six sccm respectively. The RIE and ICP powers are set to 100 and 150 W while the chamber pressure is maintained at three mTorr for the 17 s etch time. This gives an approximate etch depth of 100 nm. The RIE recipe used in this study can be found in Appendix E.

4.3.4 Fabricated NWDs

Figure **4.13** shows an SEM image of two different NWDs after etching with nominal separation of 0.5 and 0.8 μm. We measure a length greater than 2 μm for both NWDs because in the CAD program, the lines have zero line width while the SEM has a finite line width of 100-150 nm. We cannot resolve the infinitesimal sharp corners in the CAD program which results in the bulging seen at the ends of the NWD in Figure **4.13**. There is leftover e-beam resist seen as the webbed mesh particles in Figure **4.13**. We found that the e-beam resist hardens during RIE, due to the high temperatures generated inside the RIE chamber, which makes removal of resist more difficult. To combat this the samples are ultrasonic cleaned in 1165 PR remover for 3 mins.

4.4 Summary

Processing Sb quantum wells into Hall bars using the standard photolithography procedure resulted in devices having a larger resistance at 77 K when compared to unprocessed samples. This was due to a the developer unexpectedly etching our samples. A revised photolithography procedure was implemented to circumvent this problem, utilizing a Kapton shadow mask for contact deposition prior to mesa development. Much later in the growth history, Sb quantum wells were grown with a thicker cap layer to protect the underlying Sb well. Nano-wire devices were then fabricated on top of Hall bar channels using EBL and RIE.

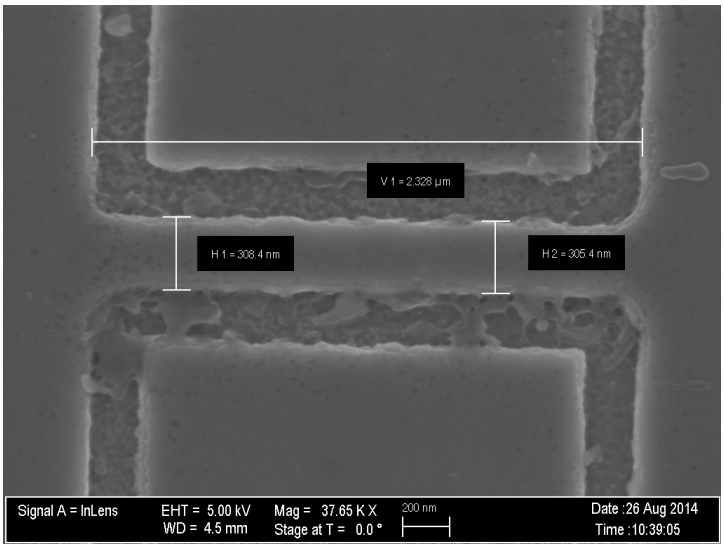

(a)

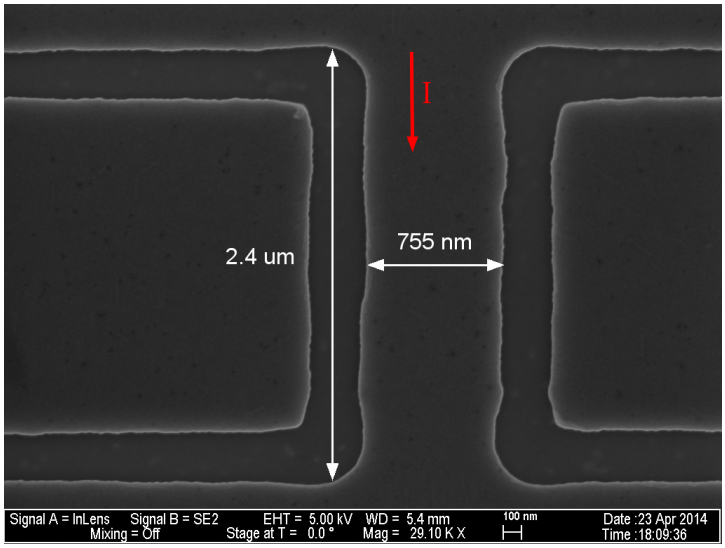

(b)

Figure 4.13: a) Close-up SEM image of a 0.5 μm wide NWD with a nominal length of 2 μm. The dark gray trenches are where the channel was etched. The webbed mesh particles are leftover e-beam resist that was not fully removed. b) SEM image of at 0.8 μm wide NWD with a nominal length of 2 μm.

Chapter 5

Magneto-transport and Quantum Interference

There are many ways to probe the physical properties of condensed matter systems; a popular technique is magneto-transport (MT). MT is a measurement of the electronic transport in a system under the influence of an external magnetic field. MT is a particularly appropriate method to study quantum interference (QI) effects like weak localization[17], universal conductance fluctuations[36], and the Aharonov-Bohm effect[37]. This chapter will cover the basics of MT and quantum interference effects.

5.1 Drude Model and Hall Effect

The typical quantity measured in MT is resistance. The simplest model is the Drude model which starts with independent charged particles in the presence of an external electric field[32]. The equation of motion is

$$\mathbf{F} = m^* \frac{d\mathbf{v}}{dt} = q\mathbf{E} \tag{5.1}$$

where $\mathbf{F}$ is the force, m^* is the effective electron mass, v is the velocity, q is the charge, and $\mathbf{E}$ is the applied electric field. The scattering of electrons with impurities and lattice defects causes the system to reach a steady state situation where v is replaced with the drift velocity v_d and we introduce the scattering time τ_e. The scattering time is the time between elastic scattering events due to impurities in the sample. The scattering time is also related to the mean free path, l_e, which is the distance between elastic scattering events. The steady state

equation is

$$m^* \frac{\mathbf{v_d}}{\tau_e} = q\mathbf{E} \tag{5.2}$$

Rearranging **5.2** for $\mathbf{v_d}$ gives

$$\mathbf{v_d} = \frac{q\tau_e}{m^*}\mathbf{E} \tag{5.3}$$

so that the current density $\mathbf{J}$ is given by

$$\mathbf{J} = nq\mathbf{v_d} = \frac{nq^2\tau_e}{m^*}\mathbf{E} \tag{5.4}$$

$$\mathbf{J} = \sigma\mathbf{E}. \tag{5.5}$$

This is Ohm's Law where the proportionality constant between current density and electric field is the Drude conductivity, σ_o, where

$$\sigma_o = \frac{nq^2\tau_e}{m^*} = nq\mu \tag{5.6}$$

and $\mu = q\tau_e/m$ is the mobility, in units of m^2/Vs. The zero field electrical resistivity ρ is defined as the inverse of the Drude conductivity

$$\rho_o = \frac{1}{\sigma_o}. \tag{5.7}$$

If an external magnetic field, $\mathbf{B}$, is applied to the system the new equation of motion is

$$\frac{m^*\mathbf{v_d}}{\tau_e} = q(\mathbf{E} + \mathbf{v_d} \times \mathbf{B}). \tag{5.8}$$

We will assume that the electron moves in the x-y plane and **B** is applied in the z direction. Equation **5.8** written in component form is

$$\frac{m^* v_x}{\tau_e} = q(E_x + v_y B) \tag{5.9}$$

$$\frac{m^* v_y}{\tau_e} = q(E_y - v_x B). \tag{5.10}$$

Rearranging **5.9** and **5.10** for E gives

$$E_x = \frac{m^* v_x}{q\tau_e} - v_y B \tag{5.11}$$

$$E_y = v_x B + \frac{m^* v_y}{q\tau_e}. \tag{5.12}$$

The above can be written in matrix form

$$\begin{pmatrix} E_x \\ E_y \end{pmatrix} = \begin{pmatrix} m^*/q\tau & -B \\ B & m^*/q\tau \end{pmatrix} \begin{pmatrix} v_x \\ v_y \end{pmatrix}. \tag{5.13}$$

Writing **5.13** in terms of current density gives

$$\begin{pmatrix} E_x \\ E_y \end{pmatrix} = \frac{1}{\sigma_0} \begin{pmatrix} 1 & -\mu B \\ \mu B & 1 \end{pmatrix} \begin{pmatrix} J_x \\ J_y \end{pmatrix} \tag{5.14}$$

where σ_o is the Drude conductivity. Equation **5.14** is the inverse of Ohm's Law which gives the resistivity tensor ρ where

$$\rho_{xx} = \rho_{yy} = \frac{1}{\sigma_0} \tag{5.15}$$

$$-\rho_{xy} = \rho_{yx} = \frac{B}{nq}. \tag{5.16}$$

Equation **5.15** gives the Drude model relation between resistivity and conductivity for ρ_{xx} and the transverse Hall resistance, ρ_{xy}, for determining sample carrier density. Recall that the Hall measurement was used in Chapter 3 during the measurement of van der Pauw samples. Inverting **5.14** gives

$$\begin{pmatrix} J_x \\ J_y \end{pmatrix} = \frac{\sigma_0}{(1+\mu^2 B^2)} \begin{pmatrix} 1 & \mu B \\ -\mu B & 1 \end{pmatrix} \begin{pmatrix} E_x \\ E_y \end{pmatrix}. \tag{5.17}$$

This is the tensor version of Ohm's Law in a magnetic field where the conductivity tensor gives

$$\sigma_{xx} = \sigma_{yy} = \frac{\sigma_0}{(1+\mu^2 B^2)} \tag{5.18}$$

$$\sigma_{xy} = -\sigma_{yx} = \frac{\sigma_0 \mu B}{(1+\mu^2 B^2)}. \tag{5.19}$$

This yields a parabolic ($\sim$B^2) field dependence of the longitudinal conductivity. This is referred to as the classical magneto-resistance effect. The classical magneto-resistance effect is used to explain the high field magneto-resistance seen in Chapter **6.11**.

5.2 Quantum Interference

In the previous section, only classical effects were considered. To account for quantum effects a free electron can be described by a plane wave function of the form

$$\Psi = A e^{ik\cdot r} e^{i\phi} \sigma \tag{5.20}$$

where A is the normalized amplitude, ϕ is the quantum mechanical phase ($\phi = -iEt/\hbar$), and σ is a Pauli spin matrix. The quantum phase is what gives rise

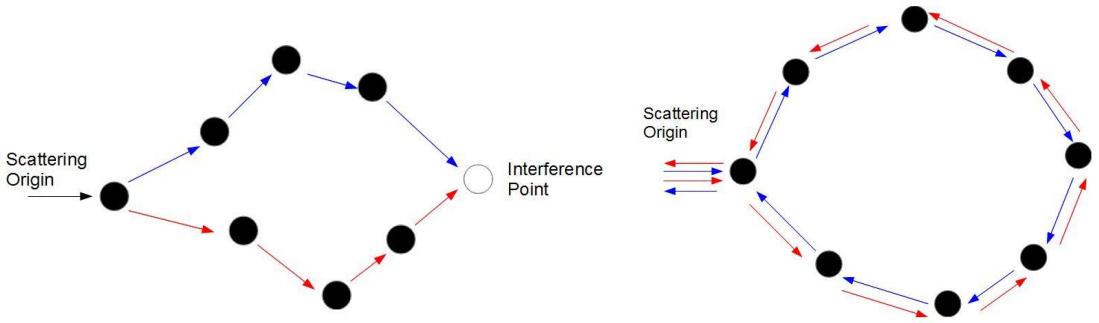

Figure 5.1: Two possible scattering cases. **Left**: Incoming carrier scatters from origin along two possible paths, blue and red, which then interfere at some later point. This is the case for UCF. **Right**: Incoming carrier scatters from origin in two possible paths, the blue (clockwise) or red (counter clockwise). The two paths interfere at the origin leading to WL or WAL. Black dots are scattering sites in the material.

to interference. Classically, the probability, P, to transition from point A to B through two different paths, 1 and 2, is the sum of the square of the amplitudes

$$P(A \to B) = |A_1|^2 + |A_2|^2 \tag{5.21}$$

while in quantum mechanics the probability is

$$P(A \to B) = |A_1|^2 + |A_2|^2 + A_1 A_2^* + A_1^* A_2 \tag{5.22}$$

The additional cross terms are the main distinction between classical and quantum cases, allowing for the interference of phase coherent electrons. There are many different types of quantum interference effects in transport, one of them is universal conductance fluctuations (UCF)[36, 38, 39] which will be covered in the following section.

5.3 Universal Conductance Fluctuations

It is possible for an electron to scatter from an origin and traverse two different paths in a sample undergoing multiple scattering events off impurities(Figure **5.1**Left). As long as the electron remains phase coherent over these paths, it can interfere at some later point which is not the origin. This leads to aperiodic fluctuations in the conductance which are reproducible. This distinguishes UCF from random noise. This effect was seen first in metals [36, 39]. What makes the effect universal is that across multiple different samples with different doping and quality amplitude of the conductance fluctuations are on the order of e^2/h, the same quantized conductance seen in Landauer-Buttiker theory[16]. Note that the amplitude of e^2/h is for a fully conducting phase coherent channel. If the sample length, L, and/or width, W, is larger than the phase breaking length, L_ϕ, the amplitude is reduced by $1/\sqrt{2N}$, where N=L*W/L_ϕ^2, is the number of phase coherent channels [38, 40].

In terms of dimensionality, UCFs can be seen in 2D and 3D[41] systems. The distinction between the two, can be probed by tilting the sample in a magnetic field. If the UCF features do not shift as the sample is being tilted then the observed effect is happening in a 3D system. If the UCF features do shift in field as the sample is tilted and instead the features are dependent on the perpendicular component of magnetic field, than the effect is 2D in origin. The nano-wire devices fabricated in Chapter 4 are used to probe UCF in Sb quantum wells.

5.4 Weak Localization and Weak Anti-Localization

Another possible scattering situation is where an electron scatters from an origin and travels in a complete loop either in a clockwise or counter-clockwise

manner returning to the origin. We will consider transport in the diffusive regime where the sample length, L, is larger than the mean free path, l_e ($L \gg l_e$). The probability to return to the origin is

$$P(\text{origin}) = |A_{cw}|^2 + |A_{ccw}|^2 + 2A_{cw}A_{ccw}. \quad (\mathbf{5.23})$$

The cross terms provides interference. The interference is constructive at the origin because both paths interact with the same impurities, except in reverse order, and thus accumulate the same phase difference. The amplitude for the clockwise and counter clockwise paths are equal, A_{cw}=A_{ccw}=A_o. This yields

$$P(\text{origin}) = |A_0|^2 + |A_0|^2 + 2|A_0||A_0| = 4|A_o|^2, \quad (\mathbf{5.24})$$

which is larger than the classical probability, $2|A_o|^2$ and is called weak localization (WL) [17]. WL is manifested as an increase in the probability to return the origin and thus a decrease in the conduction across the sample at B=0. The effect is gradually decreased in the presence of a magnetic field as flux threads through the closed paths inducing a phase difference of opposite sign for the two paths.

If the spin of the electron is included and is coupled to its momentum by the following spin orbit Hamiltonian

$$H_{soc} = -\frac{\hbar}{4mc^2}\,\boldsymbol{\sigma}\cdot(\mathbf{p}\times\nabla V) \quad (\mathbf{5.25})$$

as the electron traverses a closed loop, the spin will precess in opposite directions for CW vs CCW. This leads to destructive interference giving rise to a decrease in the probability to return to the origin. This effect is called weak anti-localization[10, 18] (WAL) and results in a conductance increase at B=0 (See Figure **5.2**). Weak anti-localization is relevant to MT transport measurements on

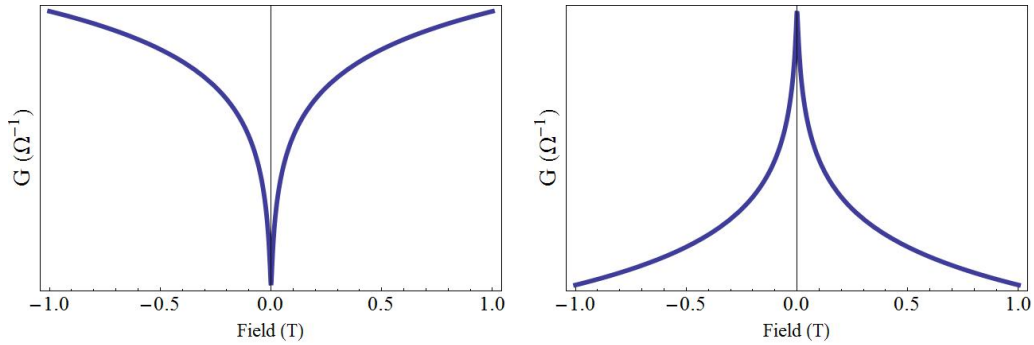

Figure 5.2: Plots of conductance vs magnetic field for WL and WAL. **Left**: Conductance plot shows a minimum at B=0 for WL. **Right**: Conductance shows a maximum at B=0 for WAL. The above plots are generated using equation **5.26** where the field dependence is part of the a parameter. In the lab a magnetic field H is applied, but in discussion B in units of Tesla is used to represent the magnetic field.

3D TIs because suppression of backscattering for the topological surface states is analogous to the destructive interference at the origin for WAL. WL and WAL can occur in both 2D and 3D systems[42, 43].

5.4.1 A Theoretical Model of WL and WAL

A seminal paper in the theoretical development of WL was published 1980 by Hikami, Larkin, and Nagaoka [10]. Using a renormalization group method and diagrammatic technique, Hikami et al. were able to determine an analytical expression for the conductivity correction due to WL in the presence of a magnetic field. Equation 17 in reference [10] is the general model for the conductivity in a magnetic field. The authors were looking for the quantum correction to the conductivity due to localization and calculate equation 18, in [10], written as

$$\Delta\sigma = -\frac{\alpha e^2}{2\pi^2\hbar}\left[-\psi\left(\frac{1}{2}+\frac{1}{\tau_\phi a}\right)+\ln\frac{1}{\tau_\phi a}\right] \qquad (\mathbf{5.26})$$

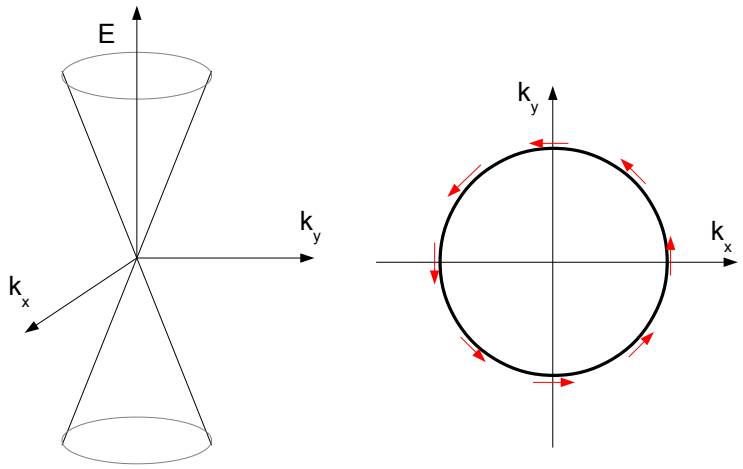

Figure 5.3: **Left:** Energy versus momentum in two-dimensional k-space for Dirac like dispersion giving a Dirac cone. **Right:** We can then plot a constant energy contour in two-dimensional k-space where the red arrows represent the spin of the electron. For the situation of backscattering, the electron can traverse the top or bottom semi-circle which gives to an total rotation of 2ϕ. For electrons this leads to an overall π phase shift of the wave function which leads to a reduction in backscattering.

where a=4DeH/$\hbar$c, τ_ϕ is the phase relaxation time, and ψ is the Digamma function (the logarithmic derivative of the Gamma function). The phase relaxation time is related to the phase breaking length l_ϕ by $l_\phi = \sqrt{D\tau_\phi}$ where D=$v_F^2\tau_e/2$, is the diffusion constant, v_F is the Fermi velocity, and τ_e is the elastic scattering time. If the spin-orbit interaction is weak and there are no magnetic impurities in the sample then α=1; this is the case for weak localization. If the spin-orbit interaction is strong and there are no magnetic impurities then the spin-orbit terms in τ_1 and τ_3 in Equation 17 from [10] are large such that the Digamma function approximates to a natural logarithm. This then cancels out equivalent logarithm terms leaving behind an α=-1/2; this is the case for weak anti-localization. Equation **5.26** will herein be referred to as the HLN model or theory.

In the case of TIs backscattering is suppressed due to a π Berry phase, acquired by the topological surface states as they traverse the Dirac cone. Recall that TI surface states are spin-momentum locked (see Chapter 2), as the states traverse the Dirac cone in k-space the spin evolves (See Figure **5.3**). Specifically if a state at $+k_x$ traverses the Fermi surface such that $+k_x \rightarrow -k_x$ where the state has backscattered it can do this by either traversing the top or bottom semi-circle. Both paths acquire a π spin flip for a total rotation of 2π. For spin $\frac{1}{2}$ particles, they have the special property that rotation by 2π gives the wave function an eigenvalue of -1. This is represented as a quantum mechanical phase of π leading to destructive interference and hence a suppression of backscattering. Thus the HLN model can be applied to the MR signal of a TI.

Recall that in the HLN model $\alpha = -\frac{1}{2}$ per a conducting channel. For 3D TIs, if bulk contributions can be neglected, then $\alpha = -1$ for the sum of top and bottom surfaces. If bulk contributions are still present the bulk states can couple the top and bottom states resulting again in $\alpha = -\frac{1}{2}$[11]. Also because TIs have large spin orbit coupling, it is possible that a residual bulk contribution could result in its own WAL signal. To distinguish between surface and bulk WAL contributions, a tilted field can be employed. While bulk states are relatively insensitive to tilted fields, surface states depend primarily on perpendicular field and thus the two components can be distinguished.

Chapter 6

Experimental Results and Discussion

After device fabrication, magneto-transport(MT) measurements were made at low temperatures, < 1.5 K, and in magnetic fields up to 18 T. A majority were made at the National High Magnetic Field Laboratory. The MT behavior can be separated at low and high field regimes. Each regime will be addressed in the sections that follow, starting with the zero field, moving to the WAL in low fields, then the high field regime and concluding with studies of nano-wires.

6.1 Zero Field Conductance Measurements

Figure **6.1** plots the resistance of a 3.6 nm Sb quantum well in units of $\Omega/\square$ versus temperature measured in Kelvin. This plot is representative of the temperature dependence across 12 different QW samples. We see the resistance increase as a function of temperature indicating insulating like behavior before saturating at lower temperatures. This is a good indication that the bulk Sb conduction is being suppressed by quantum confinement.

Figure **6.2** displays one of the more important figures in the thesis, the conductance at 20 K versus well thickness. The solid blue line in the figure shows the expected conductance of a slab of bulk Sb thinned to the thickness shown on the x axis. Also shown as open (uncapped) and solid triangles is the conductance of the wells. It is observed that the conductance of the wells lie below that of the expected conductance of the thinned bulk indicating that we have suppressed bulk conduction by quantum confinement. The conductance of the buffer layers are plotted as green squares as wells with zero thickness. The uncapped samples have

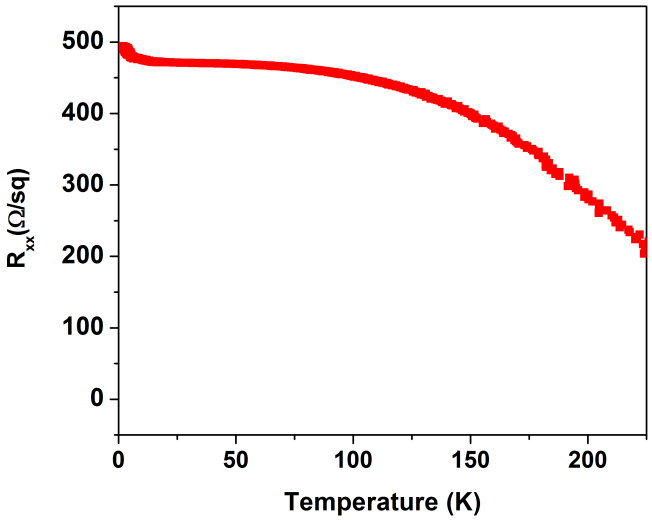

Figure 6.1: Plot of resistance in Ω/□ vs temperature for a 3.6 nm well. The sample shows insulating like behavior (dR/dT<0) indicating a reduction in bulk conduction before plateauing below 50 K. This temperature behavior is representative of all Sb samples measured in this dissertation.

additional error bars to account for the oxidation of the Sb well which reduces the the effective Sb thickness. We model the 2D conductance of our Sb wells using the following equation:

$$G = G_s + \sigma_b\, t \tag{6.1}$$

where G_s is the surface conductance, σ_b is the bulk conductivity, and t is the sample thickness. The fit using equation **6.1** is represented by the dashed line yielding a non-zero intercept which is associated with residual surface conductance. Comparing the value of the residual conductance and comparing it to that of the 3.6 nm well, we find that the surface conduction makes up approximately 13% of the total conductance. It is important to note that the value of the intercept and its associated error are on the same order. While these measurements were all in the van der Pauw geometry, additional MT measurements were made with Hall bars.

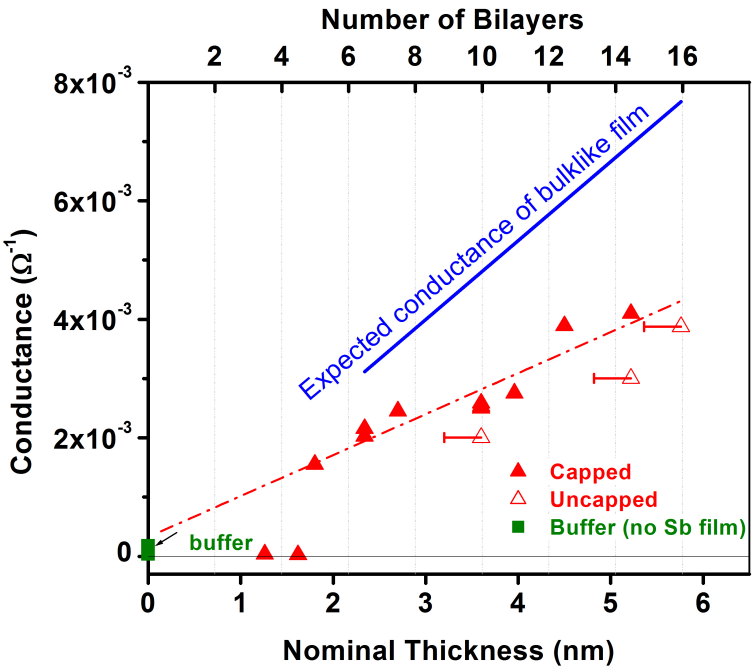

Figure 6.2: Plot of conductance at 20 K vs well thickness or number of bilayers. Blue solid line is the conductance of a bulk film thinned continuously to zero thickness. Uncapped samples have reduced well thickness, represented as error bar, due to surface oxidation. Fit to the capped sample data shows reduced bulk conduction when compared to bulk film. GaSb buffer layer conductance (green squares) is less than the measured well values emphasizing that the measured conductance originates from Sb well. Fit to capped data also gives a non-zero intercept indicating residual surface conductivity but the error in the fit is of the same order as the intercept.

6.2 Low Field Magneto-transport

In the Hall bar geometry, at lower temperatures and in the presence of a non-zero field, a large and pronounced WAL signal is observed around zero field as is expected for TIs with their large spin orbit interaction. In Figure **6.3** the WAL signal is plotted at different temperatures from -5 to 5 T. The strength of the WAL signal decreases with increasing temperature due to the decrease in the phase breaking length with increasing temperature. We employ the HLN model[10] by importing the data into Mathematica, subtracting the background to extract the

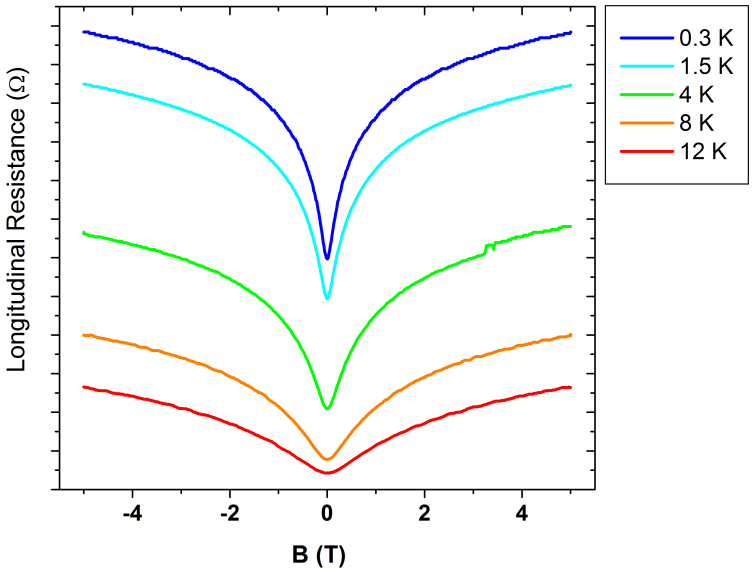

Figure 6.3: Plot of the longitudinal resistance versus magnetic field for 1.8 nm well. A strong WAL signal is clearly visible. The strength of the WAL signal decreases with increasing temperature as expected from the change of the phase breaking length with temperature.

quantum correction and then use the non-linear model function to do a least-squares fit to determine the α pre-factor and the phase breaking length. Since the total sample resistance is measured whereas the HLN model only describes the quantum correction to the conductivity, the measured data must be modified by removing a parabolic background($\alpha + \beta B^2$) or a linear background($\alpha + \beta B$). The result is divided by the square of the zero field resistance resulting in the quantum correction to the conductivity (See Appendix F). The background subtraction process is summarized as:

$$\Delta\sigma = (R_{xx} - background) * \frac{1}{(R_{xx}(B=0))^2} \tag{6.2}$$

The conductivity correction is plotted in units of $e^2/2\pi\hbar$ and fit to the HLN model. Recall that the HLN model gives two fitting parameters, α and H_ϕ, where

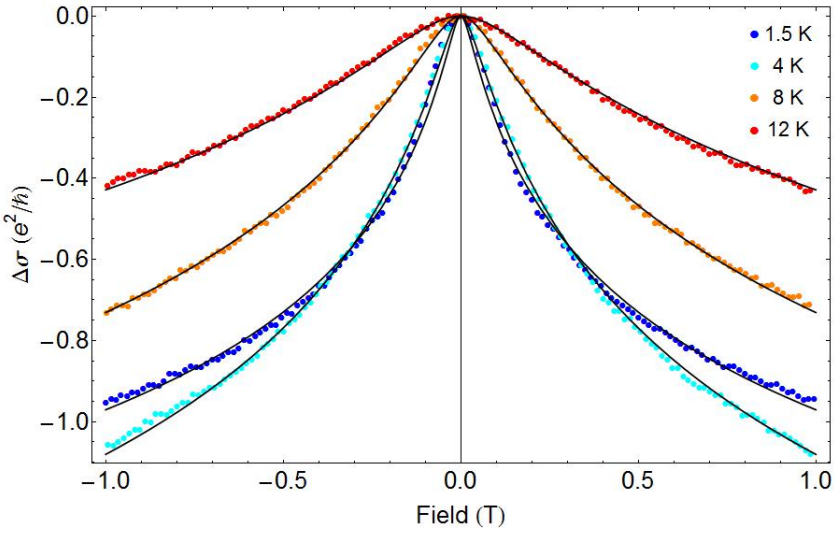

Figure 6.4: Fits to WAL using HLN model at different temperatures for 2.3 nm well. The black line are the fits to the data. The HLN model accurately describes the low field WAL signal. From these fits we can extract the α pre-factor and phase breaking length.

the phase breaking length, L_ϕ, is related to H_ϕ by,

$$L_\phi = \left(\frac{\hbar}{4eH_\phi}\right)^{1/2} \tag{6.3}$$

Fits to the data at different temperatures are shown in Figure **6.4**. The extracted values of the phase breaking length vs temperature are plotted in Figure **6.5**. The line on the log-log scale of Figure **6.5** has a slope of 0.6. This is close to the predicted value of $1/T^{1/2}$ for the temperature dependence of the dephasing mechanism in 2D by electron-electron scattering[44]. At lower temperatures however, the phase breaking length deviates from this dependence and saturates for unknown reasons. Figure **6.5** is representative of the temperature dependence for the wells presented in this study. HLN fits were made to the WAL signal for wells from 4.5 to 1.8 nm (see Appendix G) and the extracted fitting parameters as a function of thickness are plotted in Figure **6.6**.

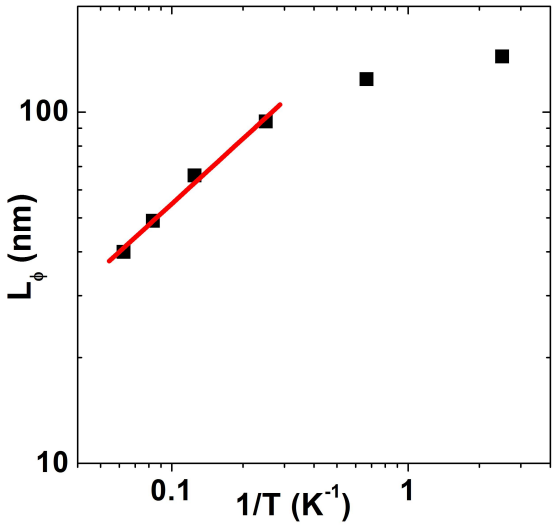

Figure 6.5: Phase breaking length for 2.3 nm versus inverse temperature. A fit to the high temperature region gives a slope of 0.6. This is close to the theoretical prediction for 2D electron-electron scattering of 0.5. No error bars are present, since they are smaller than the symbols.

Both the phase breaking length and pre-factor show very little thickness dependence. The pre-factor is close to $\frac{1}{2}$ which is the predicted value for a single channel. It is expected that for a 3D TI the top and bottom surfaces will each contribute to the conduction such that α=1. The calculated value of $\frac{1}{2}$ indicates that the top and bottom surfaces act as a single channel coupled through remaining bulk channels. WAL measurements in other 3D TI systems have also resulted in varying values of α [45–50]. This is common in TI systems because of residual bulk conduction which makes surface isolation difficult; thus making material engineering an important aspect of transport experiments on TI systems.

6.3 High Field Magneto-transport

Work at the National High Magnetic Field Laboratory (NHFML) allowed us to rotate the sample in field to probe the effects of parallel and perpendicular field. The MR was measured at different tilt angles using a rotator coupled to

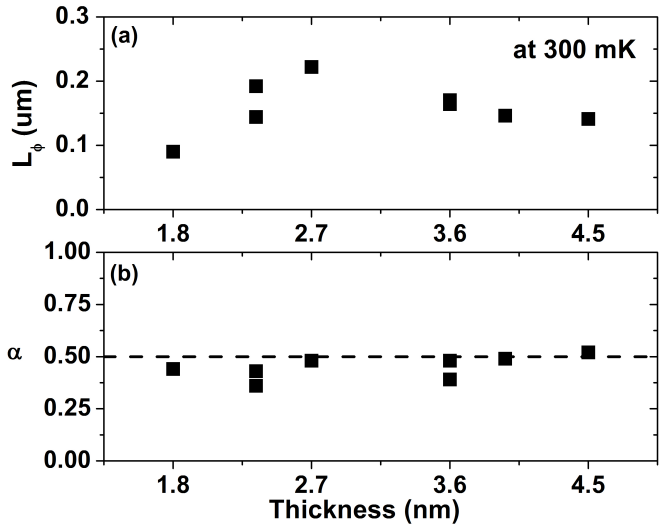

Figure 6.6: a) Phase breaking length as determined from HLN fits versus well thickness. The fits were made on data all measured at 300 mK. The phase breaking length shows little dependence on well thickness. b) The pre-factor, α, determined from HLN is around a value of $\frac{1}{2}$ and independent of well thickness. The value of $\alpha = \frac{1}{2}$ is predicted for a single channel. Our wells show single channel conduction due to residual bulk states which connect top and bottom surfaces.

the top of the cryostat by linear feed through that requires calibration before an accurate angle can be determined. Calibration is done by measuring the slope of the Hall signal at different positions as indicated by the rotator in inches. A plot of the Hall slope vs. tilter position can be seen in Figure **6.7**. The data is then fit to a cosine function of the following form,

$$A\cos[(x-B)*40*C] \qquad (\mathbf{6.4})$$

where A is the maximum value of the Hall slope, x is the linear position of the tilter in inches, B is the position of the tilter in inches corresponding to the 0° degree position, and C is a conversion factor in radians/turn. The value of 40 arises from one turn of the rotator corresponding to 0.025" of linear displacement. The solid line in Figure **6.7** is a fit to the data using equation **6.4**. With this calibration, we can relate a given linear displacement with the the tilt angle of

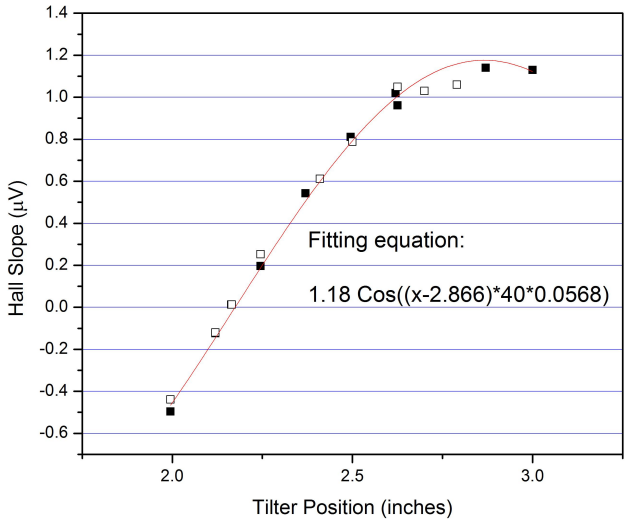

Figure 6.7: Plot of the Hall slope in μV versus the linear position of the tilter in inches. We use this plot to determine the calibration for the rotating stage. The rotator uses a linear feed through which is read out in inches, which we calibrate to determine the angle of the sample. We use the Hall signal due to its sensitivity to the perpendicular component of magnetic field. We then fit the Hall slope to a Cosine function, see equation **6.4**. The fitting equation for this set of data is given in the plot. Details of the equation can be found in the text.

the sample.

A plot of the the MR at different tilt angles is shown in Figure **6.8** for a 3.6 nm well and Figure **6.9** for a 5.8 nm well. The dip in resistance near zero is due to WAL. When the MR is plotted versus the perpendicular component of magnetic field as opposed to total field, we see that the plots collapse onto a single curve. This indicates that the MR is a 2D effect. There is one caveat though, because the magnetic length, l_B, goes as $\sqrt{h/eB}$ which even at higher fields is only 15 nm, much thicker than any of the wells measured here; even for the thickest well of 5.8 nm, we cannot distinguish between a 2D surface or 2D bulk effect.

The corresponding Hall signal for all wells is a linear up to 18 T (see Appendix **H.1**). Fits to the data using the single carrier Hall result gives a density in the mid 10^{14} cm^{-2}. This grossly overestimates the sample density. Rather band structure measurements indicate that there is more than a single carrier participating in

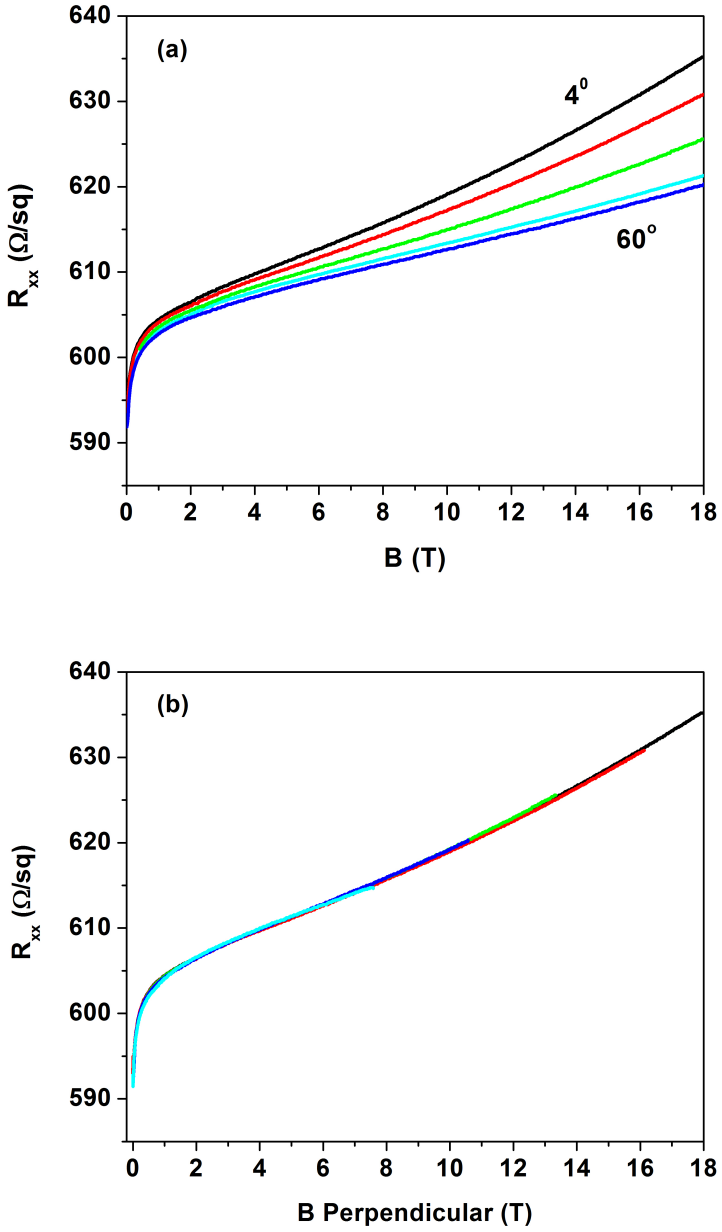

Figure 6.8: a) High field MR for 3.6 nm well at varying tilt angles of increasing value. b) Curves from a) plotted versus perpendicular field. All curves collapse onto single curve indicating 2D origin for the MR.

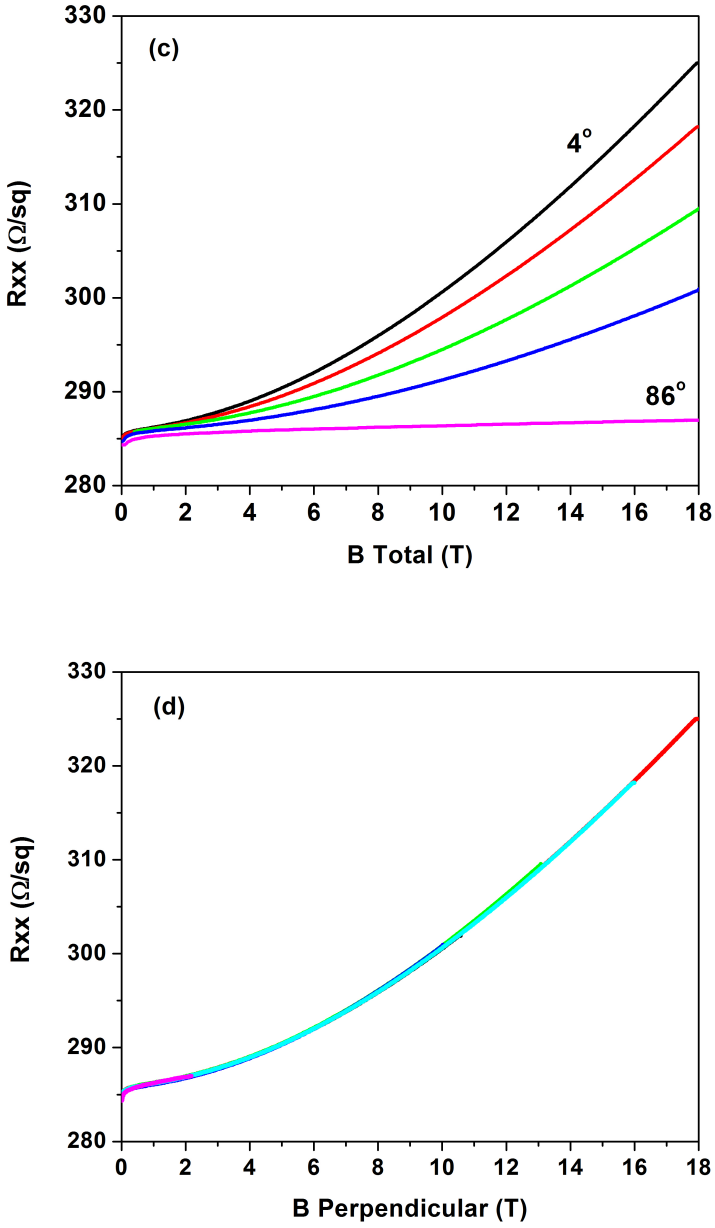

Figure 6.9: c) High field MR for 5.8 nm well for a range of tilt angles. d) Like with Figure **6.8**b), all curves collapse onto a single curve pointing towards a 2D effect.

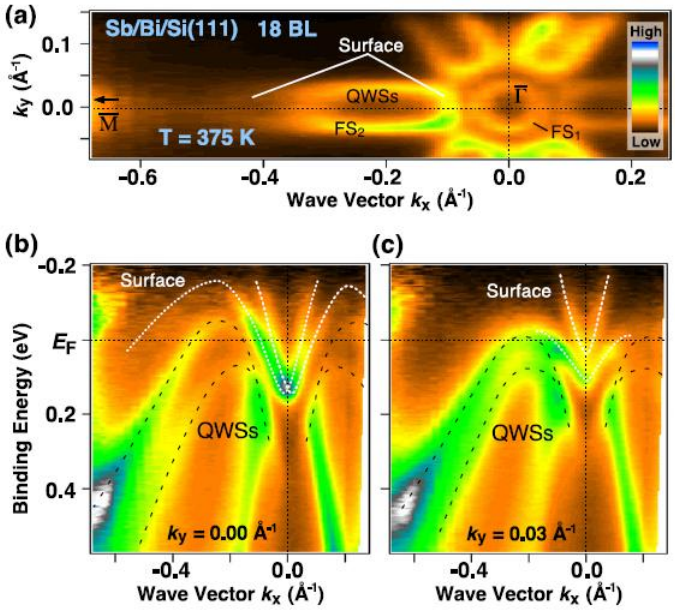

Figure 6.10: ARPES map of a 18 BL Sb thin well at 375 K taken from the $\bar{\Gamma}$ - $\bar{M}$ point. White and black dashed lines are a guide for eyes for the surface states and quantum well states (QWS) or bulk. There are two occupied Fermi surfaces, FS1 and FS2, where FS1 consists of electrons and FS2 consists of holes. Therefore, in Sb we expect more than a single carrier to participate in conduction. Figure taken from [9]

conduction as shown by a Fermi surface encircling the $\bar{\Gamma}$ point and a hole pocket along the $\bar{\Gamma}$ - $\bar{M}$ direction (See Figure **6.10**). Unfortunately multi-carrier fits to data using both the Hall and longitudinal resistance resulted in parameters that were not well constrained. Instead, from calculations using band structure, the expected carrier density was estimated to lie from 2-5x10^{12} cm^{-2} with sample mobilities ranging from 800-2000 cm^2/Vs.

In Figure **6.11** the high field MR for samples with different thicknesses is plotted together. In Figure **6.11**(a) the MR is normalized to the zero-field value of resistance for each well. For a range of thicknesses the high field behavior varies but it is difficult to visually separate the curves from each other when plotted as in Figure **6.11**(a). Instead, the curves are shifted by a fixed amount scaled by

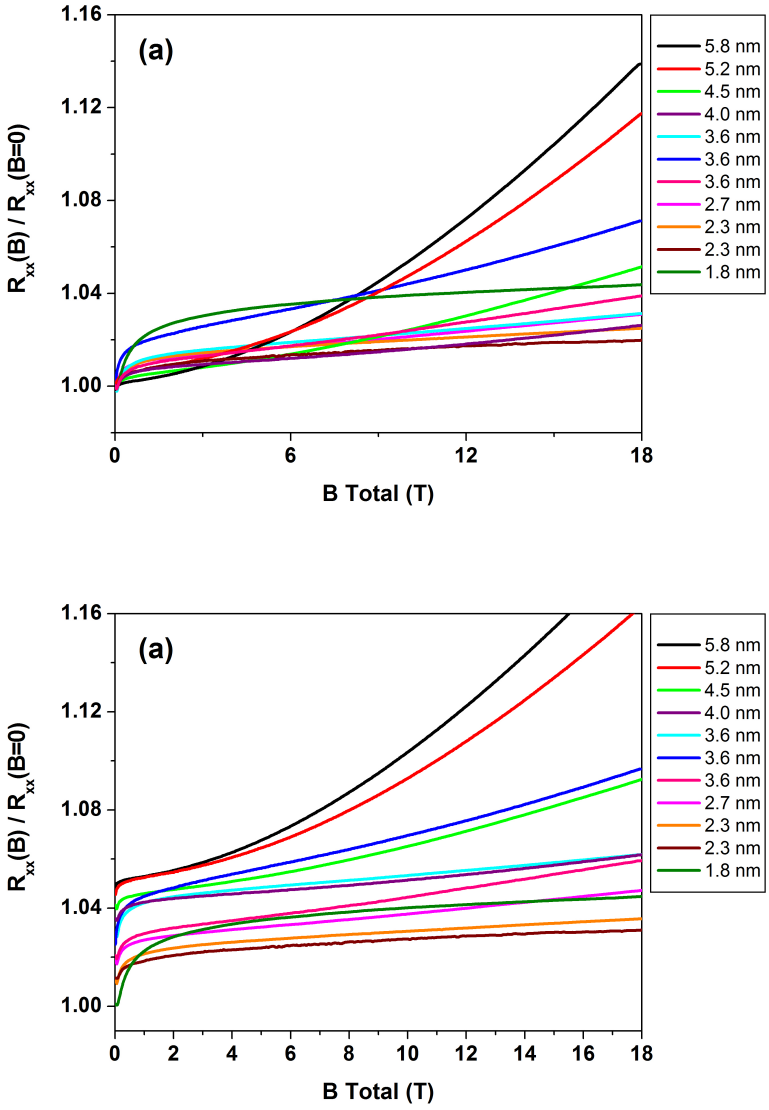

Figure 6.11: High field MR behavior for a range of sample thicknesses. The resistance is normalized by its zero-field value in both plots. (a) High field MR is plotted on top of each other showing a variation in the high field behavior across multiple well thicknesses. (b) is the same as (a) except that the curves were shifted a fixed amount scaled by their relative thickness. Starting from the 5.8 nm sample, the MR shows parabolic behavior associated with the classical MR effect but as the well thickness is decreased, the parabolic behavior evolves into a linear dependence. Observations of linear magneto-resistance with TI systems have been reported in literature[51–54].

their relative thickness, the result is Figure **6.11**(b). From this plot, as the well thickness is decreased from 5.8 nm to 1.8 nm, the MR evolves from parabolic to sub-linear behavior. The parabolic behavior is associated with classical MR; while the linear magneto resistance (LMR) behavior seen in very thin wells has been seen in other TI systems and has been attributed to Dirac linear dispersing surface states[51–54].

Abrikosov[55] studied LMR in silver chalcogenides which are gapless semiconductors with linear dispersion analogous to the energy spectrum of TIs. Abrikosov's model requires that the system be in the extreme quantum limit where all the carriers are in the lowest Landau level. However at the fields used in this study, we do not expect these samples to be in the lowest Landau level due their expected carrier density from band structure calculations ($\approx 2 - 5\text{x}10^{12}$ cm^{-2}). At these carrier densities, we would expect all states to be in the lowest Landau level at around 80 T.

Alternative models of LMR come from Parish[56] and Buttiker[57] both of whom have described LMR in systems with parabolic dispersion and varying degree of sample disorder. Parish *et. al.* does a numerical calculation using a random resistor network for an inhomogeneous semiconductor. The expected LMR using this model gives a mixing of the longitudinal resistance with the linear Hall signal. Even though the signal shows a symmetric nature as would be expected from the longitudinal resistance the Hall effect contributes a portion to the measured resistance. The size of the LMR is strongly influenced by the average mobility and mobility disorder in the sample. Comparison between this theory and our data is difficult due to the numerical nature of the calculation; nevertheless the magnitude of the LMR from this theory is considerably larger than that seen in Sb (200-400% change in silver chalcogenides vs 1-2% in Sb).

Buttiker[57] provided an explanation for LMR in simple metals (e.g. Al). If we consider a system that has grooves and protrusions due to variation in sample thickness, these sample variations can host skipping orbits. These skipping orbits are similar to what is seen in the quantum Hall effect and lead to the linear Hall effect coupling into the longitudinal resistance. The main concern with this explanation for out data is that it requires that the grooves and protrusions extend the width of the sample to contribute to the total resistance. While an SEM micrograph shows terraces in the Sb samples extending across the 4.5 μm field (See Chapter 3); it is unlikely that these terraces extend across the macroscopic size of the samples ($\sim$ 4 mm).

A more recent paper by Wang and Lei[58] provides yet another explanation for the observed LMR, invoking a linear dispersing material with over lapping Landau levels. These over lapping Landau levels can be brought about by disorder broadening, high temperatures, and/or low magnetic fields. The sign of the LMR in this theory is dependent on the sign of the g factor for the material. In Sb we observe a positive LMR while a negative g factor is expected for Sb suggesting that this too would be an unlikely explanation of our high field behavior.

Instead a better explanation of the data can be found using a simple model that takes into account both the bulk and surface channels. A similar model by Assaf *et. al.*[54] was used to explain the LMR seen in their Bi_2Te_2Se wells. The surface contribution, ρ_s, is taken to be thickness independent and its field dependence originates only from the WAL as described in Chapter 5 with experimentally determined parameters α and L_ϕ. It is assumed that the bulk contribution follows the usual classical MR of $R_B(1+\mu^2B^2)$ where R_B and μ are the thickness dependent sheet resistance and mobility of the bulk channel. These two contributions are then added in parallel which gives a model with the following parameters:

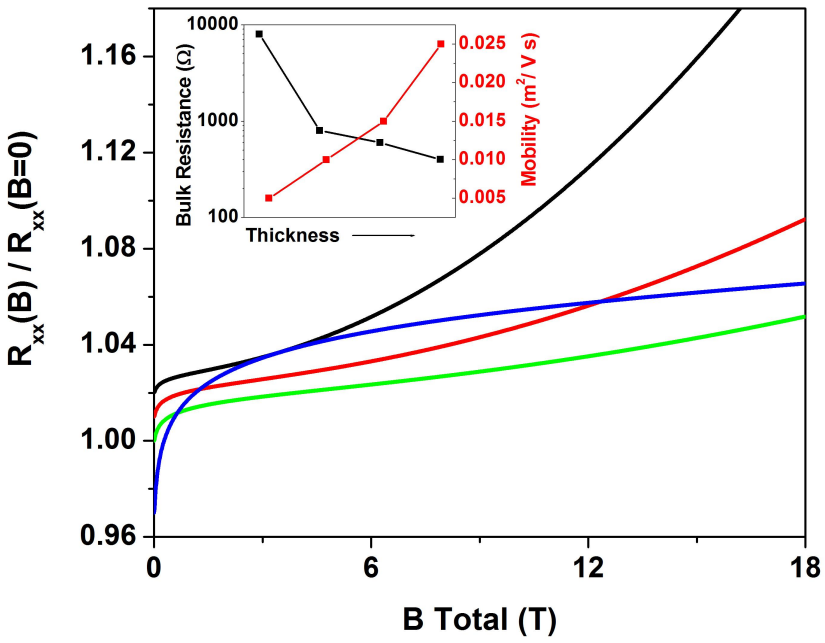

Figure 6.12: Plot of simulated MR curves generated by the simple model used to explain the high field MR. The model used to generate these curves uses a combination of bulk and surface channels simultaneously. The surface parameters are determined from experiment and are held fixed. Two bulk parameters, the bulk resistance and mobility, are varied to represent the changing well thickness. The starting values were determined when the black curve best represented the data for our thickest well. To represent a decrease in well thickness, the bulk resistance was increased while the bulk mobility was decreased. Using this model, the trend in behavior as a function of well thickness can be duplicated.

$\alpha, L_\phi, \rho_s, R_B,$ and μ. To simulate our data the value of α is kept fixed at 1/2 and ρ_s and L_ϕ are determined from experimental measurement, Figure **6.2** is used to determine ρ_s ($\approx 3000\ \Omega$) from the residual conductance at zero well thickness and L_ϕ (≈ 180 nm) is taken as the average value from WAL fits at 300 mK. Values for R_B and μ are determined such that the approximate shape and overall change of resistance are similar relative to the to experimental data. The curves in Figure **6.12** evolve from the thickest well (black) and to the thinnest well (blue). As the well thickness decreases, the value of R_B increases due to quantum confinement of the wells and the mobility decreases due to the increased role of interface roughness for thinner wells[59]. This simple model provides a good reproduction of the MR evolution of the wells for decreasing well thickness. Confirming our suspicion that surface conduction is present with a background of bulk as well.

6.4 Nano-wire Device Measurements

Our final measurements were performed on nano-wire devices. Figure **6.13** is an SEM image of a NWD measured at low temperatures. Comparing the resistance of a channel with and without a NWD is useful. In 2D the relevant quantity is the number of squares. The number squares is equal to the length of the channel divided by the width. For the 3.6 nm well the Hall bar channel (no NWD) had a sheet resistance of 515 $\Omega/\square$, while a channel with a NWD had a sheet resistance of 481 $\Omega/\square$. These two values are sufficiently comparable to each other taking into effect variations in carrier density over a single wafer.

MT measurements show the expected WAL signal at low fields, but additional features can be observed at higher fields. In Figure **6.14**(a) the longitudinal resistance vs total magnetic field is plotted at different tilt angles up to 18 T. Above 2 T reproducible aperiodic oscillations appear. Since these oscillations

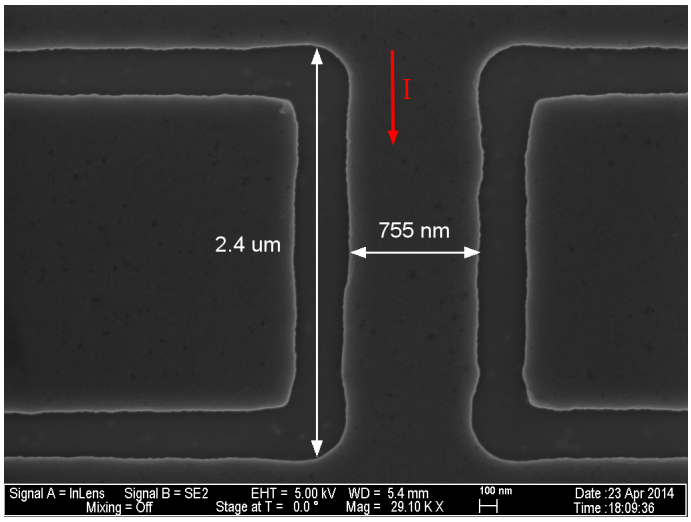

Figure 6.13: SEM image of a nano-wire device in a Hall bar channel. The length and with of the channel are needed for determining the number squares the device adds to the existing Hall bar. The red arrow indicates the flow of current through the device.

are aperiodic, they cannot be associated with Aharanov-Bohm or Shubnikov de Haas effects and because they are reproducible they are not due to random noise; rather they are universal conductance fluctuations (UCF), the manifestation of interference effects from scattering off sample impurities. Assigning a number to particular features in Figure **6.14** and tracking their position as a function of tilted magnetic field, the feature position can then be plotted as tilt angle. A $1/\cos(\theta)$ function was superimposed and describes the data well indicating that the UCF features have a 2D origin. To better identify the UCF features a linear background is subtracted from the data above 2 T. The MR with the background removed is plotted at different temperatures in Figure **6.15**. The UCF features are most pronounced at low temperatures (0.3 K) and dissipate with increasing temperature. These are preliminary results and experiments are ongoing.

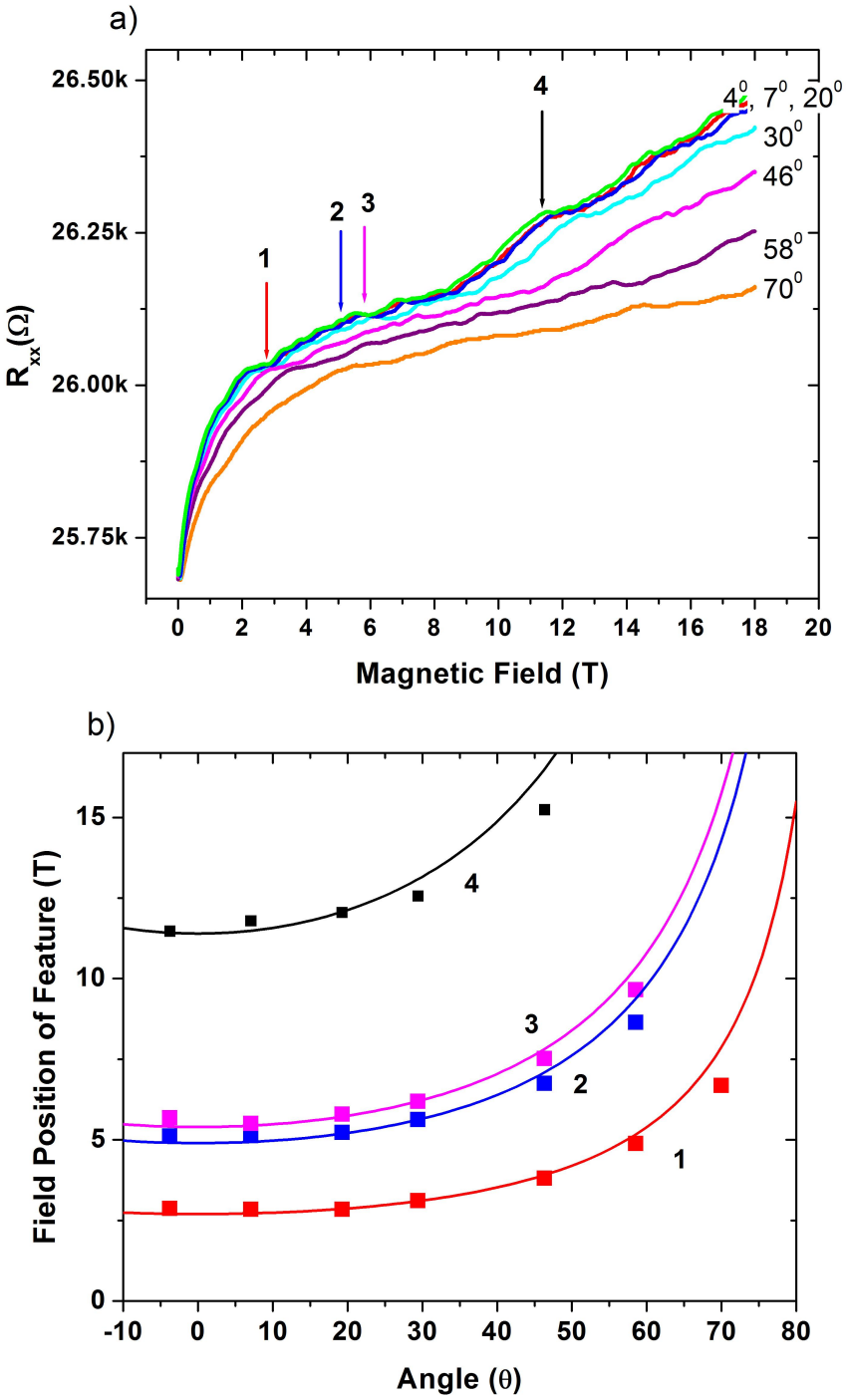

Figure 6.14: a) Longitudinal resistance versus magnetic field for 2.2 nm well at different tilt angles. For all traces, there are reproducible features associated with UCF that track with tilt angle. b) Four features, as labeled with arrows, are tracked at different tilt angles and their position in magnetic field is recorded. The field position of a feature is plotted at the given tilt angle for the sample. For each feature, the function $1/\cos(\theta)$ is plotted and well describes the data. This means the features track with the perpendicular component of magnetic field, indicating a 2D effect.

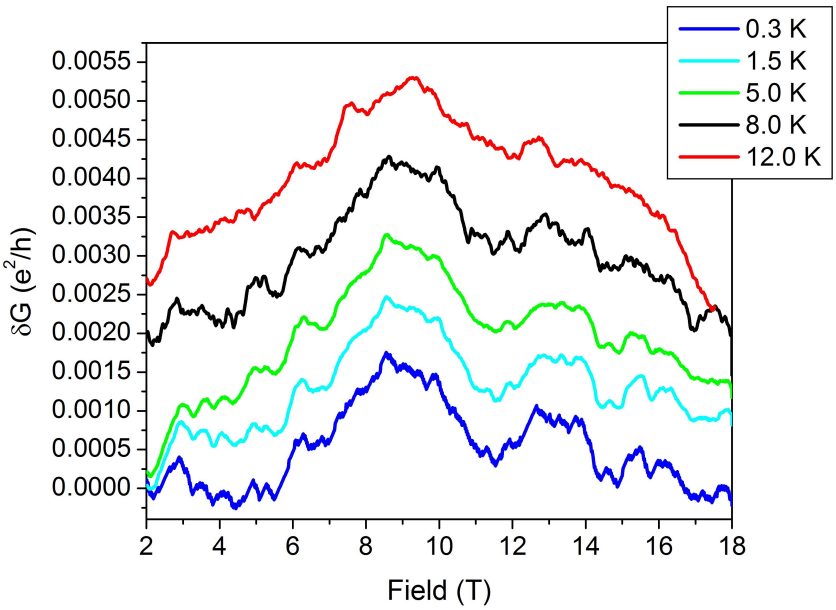

Figure 6.15: The UCF features occur on a large background that dominates the raw signal. To better study the UCF features, a linear background is subtracted from the data for fields greater than 2 T. The UCF features are most pronounced at low temperatures (0.3 K) and dissipate at higher temperatures before completely disappearing.

6.5 Summary

Multiple transport measurements were made on Hall bar and nano-wire devices of Sb quantum wells for a range of well thicknesses (2 to 6 nm). The zero field conductance of the Sb wells was measured at 20 K as a function of well thickness. A linear fit to the data showed reduced bulk conduction when compared to a continuously thinned bulk-like well, which is is expected due to the quantum confinement of the carriers in Sb. Extrapolating this fit to zero well thickness showed residual conductivity which is an indication that the Sb wells are exhibiting surface transport. There is also present an abrupt drop in the conductance around 2 nm which is due to incomplete coverage of the Sb layer for short growth times. This was confirmed using high-resolution cross-sectional TEM.

In low field, the Sb wells exhibit a large WAL signal as expected for TIs due to

topological surface states having a reduction in backscattering. This WAL signal can then be fit using the HLN model and the fitting parameters, α pre-factor and phase breaking length can be determined. For each well the HLN model is applied to WAL data for a range of temperatures (0.3 K to 15 K) to determine the temperature dependence of the phase breaking length, L_ϕ. Plots of the phase breaking length versus temperature show that at temperatures greater than 1 K the data matches well to the theory for electron-electron scattering acting as the main dephasing mechanism. Below 1 K the phase breaking deviates from theory and saturates; currently we have no explanation for this behavior.

The fitting parameters are then plotted as a function of well thickness at 0.3 K, to determine their thickness dependence. We expect for a 3D TI that the top and bottom surface should contribute an α value of $\frac{1}{2}$ to the conduction and therefore α_{TI}=1. The measured α pre-factor is on average about $\frac{1}{2}$ for well thicknesses between 1.8 and 4.5 nm. This would indicate that we have some residual bulk conduction such that our top and bottom surfaces are not well isolated, additionally over a range of thicknesses from 1.8 to 4.5 nm, we see that the WAL parameters, α and l_ϕ, are independent of well thickness.

At high fields the sample was tilted to determine whether the observed MR was either 2D or 3D in origin. Taking multiple MR traces at different tilt angles for a given well thickness and instead of plotting them versus total field were plotted versus perpendicular field where all the traces collapsed onto each other, indicating the observed effect is 2D in origin. The high MR is then plotted for a range of well thicknesses, from 6 nm to 2 nm, where the MR shows an evolution from parabolic field dependence to linear field dependence. The parabolic dependence can be explained using classical MR theory but the LMR is interesting due to current theories which expect LMR if you have a linear dispersion, as in TIs. Multiple theories were discussed but none could accurately explain the LMR seen

in our samples. We then employed a simple model that accurately reproduces our data qualitatively and quantitatively using a surface and bulk channel in concert with each other. This is not surprising since the previous stated results from measurements at zero and low field point toward our samples having a residual surface state in a bulk background.

Early measurements on NWDs show the indications of universal conductance fluctuations present in our samples, but the data was preliminary and detailed results could not be extracted. This is mainly because the fluctuations were unusually small at low temperatures and a large background was present making extraction of the UCFs difficult. Also we believe that the samples were not at as low of a temperature as measured due to resistive heating of the samples. This UCF work will be the thesis project for a future student.

Chapter 7

Conclusion

In this dissertation, a novel elemental topological insulator, Sb, was grown in ultrathin layers on GaAs (111) and GaSb (111) substrates. Growing Sb films on GaSb (111) substrates showed improved surface quality compared to GaAs (111) which had many defects due to the lattice of mismatch between the GaAs (111) substrate and the GaSb buffer layer. Resistance versus temperature plots showed reduced bulk conduction in these quantum confined Sb films. Turning these samples into Hall and nano-wire devices proved challenging due to unintentional etching by standard lithography developers, however recipes were finally established to allow for reliable photo and electron beam lithography. The optimal solution was the substitution of a 40 nm cap for the original 10 nm GaSb cap. After the successful fabrication of Hall bar devices, we were able to fabricate NWDs on top of existing channels using EBL and RIE.

Low temperature transport measurements showed $dR/dT<0$, in contrast to typical metallic behavior, pointing to reduced bulk conduction. Measuring the conductance of multiple films of different thickness, we were able to extrapolate to residual conduction at zero film thickness indicating surface transport. Additional evidence for surface transport comes from tilted MT measurements for which traces taken at different angles collapsed onto a single curve when plotted versus perpendicular field. High field MR behavior as a function of film thickness was consistent with a model that mimics the transport of a bulk channel (classical) and surface channel (WAL) in parallel. Low field MT measurements were well described the by the HLN model for WAL resulting in values of $\alpha=\frac{1}{2}$ and an average $L_\phi \approx 180$ nm at 300 mK where α and L_ϕ showed little thickness dependence.

The temperature dependence of L_ϕ was consistent with that for electron-electron scattering as the main de-phasing mechanism.

Initial measurements on NWD showed the presence of UCF. Tilted measurement of UCF indicated 2D origins. Calculations of expected δG_{rms} were smaller than that predicted by theory however these preliminary measurements were not ideal due to unexpected processing complications and self-heating effects during measurement.

Taken in concert the transport data points to the existence of significant surface conduction with α and L_ϕ independent of film thickness. The WAL shows that the states have suppressed backscattering (due to either strong spin-orbit or topological effects) in a background of residual bulk conduction. Additional evidence for a TI state is seen in the abrupt transition in conduction at 2 nm thickness although it is unclear if this is the effect of discontinuous films at the lower well thickness limit. Additional experiments are required to confirm the topological origin of the surface conduction.

7.1 Future Work

In the immediate future, the investigation and refining of the NWDs will allow for a more thorough explanation of the UCF observed at low temperatures. Presently three different NWD widths are being used but the length the device is kept constant. Variation of device length should show a transition between phase coherent regimes. Other quantum interference effects could also be studied in Sb films such as the Aharonov-Bohm (AB) effect. In TIs the AB effect is a way of probing the topological surface state. For 3D TIs where the transport is only on the surface, by taking a nano-wire and applying a magnetic field along the long axis of the wire, then the topological surface states will enclose some flux. This

incorporated flux will then cause periodic oscillations in the MR. Determination of the oscillation period can then be equated to the cross-sectional area of the wire. If the calculated cross-sectional area matches the experimentally measured cross-sectional area by SEM and/or atomic force microscopy, then this is confirmation of surface transport.

Some other high quality TIs have been explored with Shubnikov de Haas oscillations (SdH). At the moment we do not see the presence of SdH oscillations in the MR data for Sb. If we produce a better quality sample such that SdH oscillations are present then we could produce a plot of oscillation index versus inverse field where the index corresponds to either a minimum or maximum in the oscillation. A linear fit to this data with an x intercept of 1/2 vs. 0 indicates a non-trivial vs. trivial Berry's phase. Respectively, the data must be analyzed carefully as there are many caveats to be aware of.

Additionally investigations into gating the samples is currently a work in progress. In this project a layer of Al_2O_3 is applied using atom layer deposition on top of a complete set of Hall bar devices. This layer will act as a gate dielectric, which is then covered with a gate metal (e.g. Cr/Au or Ti/Au). Gated Sb devices will allow for probing of the Dirac point in the Sb band structure along with depletion of bulk carriers to enhance surface channel signal. Overall Sb based TIs are a technically challenging area of research worth pursuit due to the unique aspects of an elemental TI.

References

[1] M. Z. Hasan and C. L. Kane, "*Colloquium* : Topological insulators," *Rev. Mod. Phys.*, vol. 82, pp. 3045–3067, Nov 2010.

[2] B. A. Bernevig, T. L. Hughes, and S.-C. Zhang, "Quantum spin hall effect and topological phase transition in hgte quantum wells," *Science*, vol. 314, no. 5806, pp. 1757–1761, 2006.

[3] M. König, S. Wiedmann, C. Brne, A. Roth, H. Buhmann, L. W. Molenkamp, X.-L. Qi, and S.-C. Zhang, "Quantum spin hall insulator state in hgte quantum wells," *Science*, vol. 318, no. 5851, pp. 766–770, 2007.

[4] Y. Liu and R. E. Allen, "Electronic structure of the semimetals bi and sb," *Phys. Rev. B*, vol. 52, pp. 1566–1577, Jul 1995.

[5] D. Hsieh, Y. Xia, L. Wray, D. Qian, A. Pal, J. H. Dil, J. Osterwalder, F. Meier, G. Bihlmayer, C. L. Kane, Y. S. Hor, R. J. Cava, and M. Z. Hasan, "Observation of unconventional quantum spin textures in topological insulators," *Science*, vol. 323, no. 5916, pp. 919–922, 2009.

[6] P. F. Zhang, Z. Liu, W. Duan, F. Liu, and J. Wu, "Topological and electronic transitions in a sb(111) nanofilm: The interplay between quantum confinement and surface effect," *Phys. Rev. B*, vol. 85, p. 201410, May 2012.

[7] C. K. Gaspe, S. Cairns, L. Lei, K. S. Wickramasinghe, T. D. Mishima, J. C. Keay, S. Q. Murphy, and M. B. Santos, "Epitaxial growth of elemental sb quantum wells," *Journal of Vacuum Science & Technology B*, vol. 31, no. 3, pp. –, 2013.

[8] C. S. Wu, Y. Makiuchi, and C. Chen, *High-energy Electron Beam Lithography for Nanoscale Fabrication*. InTech, 2010.

[9] A. Takayama, T. Sato, S. Souma, and T. Takahashi, "Rashba effect in antimony and bismuth studied by spin-resolved arpes," *New Journal of Physics*, vol. 16, p. 055004, 2014.

[10] S. Hikami, A. I. Larkin, and Y. Nagaoka, "Spin-orbit interaction and magnetoresistance in the two dimensional random system," *Progress of Theoretical Physics*, vol. 63, no. 2, pp. 707–710, 1980.

[11] Y. Ando, "Topological insulator materials," *Journal of the Physical Society of Japan*, vol. 82, no. 10, p. 102001, 2013.

[12] C. Brüne, C. X. Liu, E. G. Novik, E. M. Hankiewicz, H. Buhmann, Y. L. Chen, X. L. Qi, Z. X. Shen, S. C. Zhang, and L. W. Molenkamp, "Quantum hall effect from the topological surface states of strained bulk hgte," *Phys. Rev. Lett.*, vol. 106, p. 126803, Mar 2011.

[13] L. Fu and C. L. Kane, "Topological insulators with inversion symmetry," *Phys. Rev. B*, vol. 76, p. 045302, Jul 2007.

[14] K. v. Klitzing, G. Dorda, and M. Pepper, "New method for high-accuracy determination of the fine-structure constant based on quantized hall resistance," *Phys. Rev. Lett.*, vol. 45, pp. 494–497, Aug 1980.

[15] R. B. Laughlin, "Quantized hall conductivity in two dimensions," *Phys. Rev. B*, vol. 23, pp. 5632–5633, May 1981.

[16] S. Datta, *Electronic Transport in Mesocopic Systems*. Cambridge University Press, 1995.

[17] B. L. Altshuler, D. Khmel'nitzkii, A. I. Larkin, and P. A. Lee, "Magnetoresistance and hall effect in a disordered two-dimensional electron gas," *Phys. Rev. B*, vol. 22, pp. 5142–5153, Dec 1980.

[18] G. Bergmann, "Weak localization in thin films: a time-of-flight experiment with conduction electrons," *Physics Reports*, vol. 107, no. 1, pp. 1 – 58, 1984.

[19] A. H. Castro Neto, F. Guinea, N. M. R. Peres, K. S. Novoselov, and A. K. Geim, "The electronic properties of graphene," *Rev. Mod. Phys.*, vol. 81, pp. 109–162, Jan 2009.

[20] L. Fu and C. L. Kane, "Superconducting proximity effect and majorana fermions at the surface of a topological insulator," *Phys. Rev. Lett.*, vol. 100, p. 096407, Mar 2008.

[21] V. Mourik, K. Zuo, S. M. Frolov, S. R. Plissard, E. P. A. M. Bakkers, and L. P. Kouwenhoven, "Signatures of majorana fermions in hybrid superconductor-semiconductor nanowire devices," *Science*, vol. 336, p. 1003, 2012.

[22] C. Nayak, S. H. Simon, A. Stern, M. Freedman, and S. Das Sarma, "Non-abelian anyons and topological quantum computation," *Rev. Mod. Phys.*, vol. 80, pp. 1083–1159, Sep 2008.

[23] M. Leijnse and K. Flensberg, "Introduction to topological superconductivity and majorana fermions." arXiv:1206.1736 [cond-mat.mes-hall].

[24] A. Ibrahim and D. Thompson, "Thermoelectric properties of bisb alloys," *Materials Chemistry and Physics*, vol. 12, no. 1, pp. 29 – 36, 1985.

[25] G. Bian, X. Wang, Y. Liu, T. Miller, and T.-C. Chiang, "Interfacial protection of topological surface states in ultrathin sb films," *Phys. Rev. Lett.*, vol. 108, p. 176401, Apr 2012.

[26] C.-H. Lee and C.-K. Yang, "Topological surface states revealed by sb thin films adsorbed with impurity atoms," *Phys. Rev. B*, vol. 87, p. 115306, Mar 2013.

[27] A. Narayan, I. Rungger, and S. Sanvito, "Topological surface states scattering in antimony," *Phys. Rev. B*, vol. 86, p. 201402, Nov 2012.

[28] S.-X. Wang, P. Zhang, and S.-S. Li, "Topological properties of sb(111) surface: A density functional theory study." arXiv:1201.1976 [con-mat.mtrl-sci], 2012.

[29] T. D. Golding, J. A. Dura, W. C. Wang, A. Vigliante, S. C. Moss, H. C. Chen, J. H. Miller, C. A. Hoffman, and J. R. Meyer, "Sb/gasb heterostructures and multilayers," *Applied Physics Letters*, vol. 63, no. 8, pp. 1098–1100, 1993.

[30] T. D. Golding, J. A. Dura, H. Wang, J. T. Zborowski, A. Vigliante, H. C. Chen, J. H. M. Jr, and J. R. Meyer, "Investigation of sb/gasb multilayer structures for potential application as an indirect narrow-bandgap material," *Semicond. Sci. Technol*, vol. 8, p. S117, 1993.

[31] L. J. van der Pauw, "A method for measuring specific resistivity and hall effect of discs of arbitrary shape," *Phllips Res. Repts.*, vol. 13, pp. 1–9, 1958.

[32] C. Kittel, *Introduction to Solid State Physics*. John Wiley & Sons, Inc, 2005.

[33] A. Girschik, F. Libisch, and S. Rotter, "Topological insulator in the presence of spatially correlated disorder," *Phys. Rev. B*, vol. 88, p. 014201, Jul 2013.

[34] P. S. Dutta, H. L. Bhat, and V. Kumar, "The physics and technology of gallium antimonide: An emerging optoelectronic material," *Journal of Applied Physics*, vol. 81, no. 9, pp. 5821–5870, 1997.

[35] MicroChemicals, "Aluminum etching." `http://www.microchemicals.com/technical_information/aluminium_etching.pdf`.

[36] P. A. Lee and A. D. Stone, "Universal conductance fluctuations in metals," *Phys. Rev. Lett.*, vol. 55, pp. 1622–1625, Oct 1985.

[37] Y. Aharonov and D. Bohm, "Significance of electromagnetic potentials in the quantum theory," *Phys. Rev.*, vol. 115, pp. 485–491, Aug 1959.

[38] P. A. Lee, A. D. Stone, and H. Fukuyama, "Universal conductance fluctuations in metals: Effects of finite temperature, interactions, and magnetic field," *Phys. Rev. B*, vol. 35, pp. 1039–1070, Jan 1987.

[39] S. Washburn and R. A. Webb, "Aharonov-bohm effect in normal metal quantum coherence and transport," *Advances in Physics*, vol. 35, no. 4, pp. 375–422, 1986.

[40] E. Akkermans and G. Montambaux, *Mesocopic Physics of Electrons and Photons*. Cambridge University Press, 2007.

[41] A. Ghosh and A. K. Raychaudhuri, "Universal conductance fluctuations in three dimensional metallic single crystals of si," *Phys. Rev. Lett.*, vol. 84, pp. 4681–4684, May 2000.

[42] P. Lindqivst, "Analysis of the magnetoresistance of three-dimensional amorphous metals with weak localization and electron-electron interaction theories," *Journal of Physics: Condensed Matter*, vol. 4, p. 177, 1992.

[43] A. Gilbertson, A. Newaz, W.-J. Chang, R. Bashir, S. Solin, and L. Cohen, "Dimensional crossover and weak localization in a 90 nm n-gaas thin film," *Applied Physics Letters*, vol. 95, p. 012113, 2009.

[44] B. L. Altshuler, A. G. Aronov, and D. E. Khmelnitsky, "Effects of electron-electron collisions with small energy transfers on quantum localisation," *Journal of Physics C: Solid State Physics*, vol. 15, no. 36, p. 7367, 1982.

[45] J. Chen, H. J. Qin, F. Yang, J. Liu, T. Guan, F. M. Qu, G. H. Zhang, J. R. Shi, X. C. Xie, C. L. Yang, K. H. Wu, Y. Q. Li, and L. Lu, "Gate-voltage control of chemical potential and weak antilocalization in bi_2se_3," *Phys. Rev. Lett.*, vol. 105, p. 176602, Oct 2010.

[46] J. Chen, X. Y. He, K. H. Wu, Z. Q. Ji, L. Lu, J. R. Shi, J. H. Smet, and Y. Q. Li, "Tunable surface conductivity in bi_2se_3 revealed in diffusive electron transport," *Phys. Rev. B*, vol. 83, p. 241304, Jun 2011.

[47] H.-T. He, G. Wang, T. Zhang, I.-K. Sou, G. K. L. Wong, J.-N. Wang, H.-Z. Lu, S.-Q. Shen, and F.-C. Zhang, "Impurity effect on weak antilocalization in the topological insulator bi_2te_3," *Phys. Rev. Lett.*, vol. 106, p. 166805, Apr 2011.

[48] Y. S. Kim, M. Brahlek, N. Bansal, E. Edrey, G. A. Kapilevich, K. Iida, M. Tanimura, Y. Horibe, S.-W. Cheong, and S. Oh, "Thickness-dependent bulk properties and weak antilocalization effect in topological insulator bi_2se_3," *Phys. Rev. B*, vol. 84, p. 073109, Aug 2011.

[49] M. Liu, C.-Z. Chang, Z. Zhang, Y. Zhang, W. Ruan, K. He, L.-l. Wang, X. Chen, J.-F. Jia, S.-C. Zhang, Q.-K. Xue, X. Ma, and Y. Wang, "Electron interaction-driven insulating ground state in bi_2se_3 topological insulators in the two-dimensional limit," *Phys. Rev. B*, vol. 83, p. 165440, Apr 2011.

[50] J. Wang, A. M. DaSilva, C.-Z. Chang, K. He, J. K. Jain, N. Samarth, X.-C. Ma, Q.-K. Xue, and M. H. W. Chan, "Evidence for electron-electron interaction in topological insulator thin films," *Phys. Rev. B*, vol. 83, p. 245438, Jun 2011.

[51] X. Wang, Y. Du, S. Dou, and C. Zhang, "Room temperature giant and linear magnetoresistance in topological insulator bi_2te_3 nanosheets," *Phys. Rev. Lett.*, vol. 108, p. 266806, Jun 2012.

[52] Y. Yan, L.-X. Wang, D.-P. Yu, and Z.-M. Liao, "Large magnetoresistance in high mobility topological insulator bi2se3," *Applied Physics Letters*, vol. 103, no. 3, pp. –, 2013.

[53] H. B. Zhang, H. L. Yu, D. H. Bao, S. W. Li, C. X. Wang, and G. W. Yang, "Weak localization bulk state in a topological insulator bi_2te_3 film," *Phys. Rev. B*, vol. 86, p. 075102, Aug 2012.

[54] B. A. Assaf, T. Cardinal, P. Wei, F. Katmis, J. S. Moodera, and D. Heiman, "Linear magnetoresistance in topological insulator thin films: Quantum phase coherence effects at high temperatures," *Applied Physics Letters*, vol. 102, no. 1, pp. –, 2013.

[55] A. A. Abrikosov, "Quantum magnetoresistance," *Phys. Rev. B*, vol. 58, pp. 2788–2794, Aug 1998.

[56] M. M. Parish and P. B. Littlewood, "Non-saturating magnetoresistance in heavily disordered semiconductors," *Nature*, vol. 42, pp. 162–165, 2003.

[57] M. Büttiker, "Magnetoresistance of very pure simple metals," *Phys. Rev. B*, vol. 42, pp. 3197–3200, Aug 1990.

[58] C. M. Wang and X. L. Lei, "Linear magnetoresistance on the topological surface," *Phys. Rev. B*, vol. 86, p. 035442, Jul 2012.

[59] H. Sakaki, T. Noda, K. Hirakawa, M. Tanaka, and T. Matsusue, "Interface roughness scattering in gaas/alas quantum wells," *Applied Physics Letters*, vol. 51, no. 23, pp. 1934–1936, 1987.

[60] N. W. Ashcroft and N. D. Mermin, *Solid State Physics*. Harcourt College Publishers, 1976.

Appendix A

Wet Etching Recipe

1. Take 30% H_2O_2 out of fridge to allow bottle to come to room temperature.
2. Add DI water to "DI water only" plastic beaker for rinsing after etching.
3. Measure out 25 mL and 90 mL of DI water in plastic graduated cylinders.
4. Add 25 mL of DI water to plastic beaker label "HF etching".
5. Using the 1-5 mL pipettor, extract 1.8 mL of H_2O_2 from the 30% H_2O_2 bottle and add it to the 25 mL DI water.
6. Using the 1-5 mL pipettor, extract 3 mL of Lactic Acid from 85% Lactic Acid bottle and add it to the H_2O_2/water solution.
7. Using the 100-1000 μL pipettor, extract 0.46 mL of 49% HF and add it to the H_2O_2/Lactic acid/water solution.

Notes

- Use only plastic beakers and items. HF will etch glass
- Use clean pipettor tips to extract amounts from stock chemicals. This prevents contamination of bulk bottle.
- If bulk bottle is not full enough to use pipettor safely then pour an appropriate amount of chemical into a small plastic beaker.
- Make sure to use protection when using HF (e.g. double gloves, smock, face mask, etc.)

- When using pipettor, depress the plunger to fully expel air from tip. When dispensing chemical, fully depress the pipettor past the catch point or there will leave a small amount of chemical left in the tip.

Appendix B

Standard Processing

1. Cleave out sample from wafer. Size of sample should be larger than 6 mm x 6 mm for adequate vacuum on spinner.
2. De-grease sample using ultrasonic in Acetone, Methanol, and Isopropyl for five minutes each.
3. Dehydration bake in oven at 150° C for 10 minutes.
4. Let sample cool on aluminum plate for two minutes.
5. Pre-spin sample at 4000 RPM for 40 sec while blowing on sample with N2 gun.
6. Apply resist using disposable pipette.
7. Spin resist at 4000 RPM for 40 sec.
8. Pre-bake sample at 95° on hot plate.
9. Let sample cool on aluminum plate for two minutes.
10. Expose sample for 6.5 sec at 275 W.
11. Develop for 60 sec in MF-319 or AZ 1:1 developer.
12. Rinse in DI water for two minutes.
13. Hard bake sample at 120° C for one minute.
14. Etch mesa for desired time.
15. Remove resist using 1165 remover for one minute.

16. Repeat steps 6 to 13.

17. Expose sample for 2.5 sec.

18. Heat sample on hot plate for 120° C for 1.5 min.

19. Flood expose sample for 50 sec.

20. Develop for 60 sec in MF-319 or AZ 1:1 developer.

21. Rinse in DI water for two minutes.

22. Paste sample using photoresist to silicon wafer for loading into evaporator.

23. Deposit 100 nm indium film.

24. Lift-off metal with 1165 remover.

Appendix C

Revised Processing

1. Cleave out sample from wafer. Size of sample should be larger than 6 mm x 6 mm for adequate vacuum on spinner.
2. Using photoresist, paste the sample and stand off posts on a silicon wafer.
3. Paste the Kapton shadow mask to the posts using photoresist.
4. Deposit 100 nm indium film.
5. Remove mask and sample from silicon wafer with 1165 remover.
6. De-grease sample using ultrasonic in Acetone, Methanol, and Isopropyl for five minutes each.
7. Dehydration bake in oven at 150° C for 10 minutes.
8. Let sample cool on aluminum plate for two minutes.
9. Pre-spin sample at 4000 RPM for 40 sec while blowing on sample with N2 gun.
10. Apply resist using disposable pipette.
11. Spin resist at 4000 RPM for 40 sec.
12. Pre-bake sample at 95° on hot plate.
13. Let sample cool on aluminum plate for two minutes.
14. Expose sample for 6.5 sec at 275 W.
15. Develop for 60 sec in MF-319 or AZ 1:1 developer.

16. Rinse in DI water for two minutes.

17. Hard bake sample at 120° C for one minute.

18. Etch mesa for desired time.

19. Remove resist using 1165 remover for one minute.

Appendix D

EBL Procedure

1. Clean sample in ultrasonic with Acetone and Isopropyl for five minutes each.
2. Dehydration bake at 150° for 10 min.
3. Cool sample on aluminum plate for two minutes.
4. Dry spin sample at 5000 RPM for 45 sec while blowing with N2 gun.
5. Apply ZEP520A using disposable pipette.
6. Spin ZEP520A at 5000 RPM for 45 sec for film thickness of about 300 nm.
7. Expose sample in SEM using line dose of 2.2 nC. This gives a good balance between clearing resist and line resolution.
8. Develop in Xylenes for 45 sec.
9. Rinse in Isopropyl for 30 sec.
10. Bake at 130° C for two minutes.
11. Etch lines into sample using RIE recipe.
12. Remove ZEP520A using 1165 remover in ultrasonic for 3-5 min as needed to completely remove resist.

Notes

- Nominal values of SEM settings: Probe Current: 1x10^{-}10 - 3x10^{-}11, Filament Current: 240μA, Emission Current 40μA, and Beam Current 15-33 pA.

- Spin e-beam resist the day of exposure to prevent prolonged white light exposure
- The SEM beam needs to be warmed up for at least 30 min, this gives time for the tungsten filament to stabilize
- The stage and beam in the SEM are not aligned such that X-Y moves horizontal and vertical on the CRT. To square the stage and beam use the following procedure:

    1. Find a vertical edge, usually the sample itself.
    2. Bring up the CRT cross-hairs using "B-UP".
    3. Using scan rotate, align the vertical edge of the sample parallel with the cross-hair.
    4. Using the stage rotate, bring the vertical edge of the sample on top of the cross-hair.
    5. Translate in Y to make sure that you can travel the length of sample without any horizontal shifting.
    6. This process maybe have to be iterated until the stage and beam are squared.

Appendix E

RIE Recipe

1. Attach samples and witness to wafer plate with Kapton tape. Use small strips over the corners to secure pieces to wafer plate.
2. Load wafer plate into load lock chamber and pump.
3. RIE will automatically load wafer plate into reactor chamber when load lock pressure has reached 50 mTorr.
4. Let chamber pump down to 5x10^{-5} Torr.
5. Run O_2 descum recipe. When descum starts check through sight glass to make sure plasma has struck.
6. Let chamber pump down to 1x10^{-5} Torr.
7. "Run BCl_3+Ar" recipe. Check sight glass to make sure plasma has struck.
8. Unload wafer plate and remove samples.
9. Clean wafer plate with Isopropyl to remove leftover Kapton adhesive.

Notes

- O_2 Descum settings:
  - O_2 flow 50 sccm
  - RIE Power 40 W
  - ICP Power 100 W

  - Time 30 s
  - Chamber pressure 25 mTorr

- BCl_3+Ar settings:
  - BCl_3 flow 4 sccm
  - Ar flow 6 sccm
  - RIE Power 100 W
  - ICP Power 150 W
  - Etch time 17 s
  - Chamber pressure 3 mTorr
- Etch depth approximately 100 nm for 17s etch.
- Cover half the witness sample in Kapton to form a step edge for measuring etch depth on profilometer.

Appendix F

Background Subtraction for WAL fitting

Drude model or classical magneto-resistance effect:

$$\rho_{xx} = \frac{1}{ne\mu} = \frac{1}{\sigma_o}$$
$$\rho_{xy} = \frac{B}{ne}$$
$$\sigma_{xx} = \frac{\sigma_o}{1+\mu^2B^2}$$
$$\sigma_{xy} = \frac{\sigma_o\mu B}{1+\mu^2B^2}$$

Now lets include WAL ($\Delta\sigma$)

$$\sigma_{xxTotal} = \frac{\sigma_o}{1+\mu^2B^2} + \Delta\sigma = \frac{\sigma_o + \Delta\sigma(1+\mu^2B^2)}{1+\mu^2B^2}$$

ρ_{xx} is measured in experiment so

$$\rho_{xx} = \frac{\sigma_{xxTotal}}{\sigma_{xxTotal}^2 + \sigma_{xy}^2} = \frac{\frac{\sigma_o+\Delta\sigma(1+\mu^2B^2)}{1+\mu^2B^2}}{\left(\frac{\sigma_o+\Delta\sigma(1+\mu^2B^2)}{1+\mu^2B^2}\right)^2 + \left(\frac{\sigma_o\mu B}{1+\mu^2B^2}\right)^2}$$

Expanding the squares gives

$$\rho_{xx} = \frac{\frac{\sigma_o+\Delta\sigma(1+\mu^2B^2)}{1+\mu^2B^2}}{\left(\frac{\sigma_o^2+2\sigma_o\Delta\sigma(1+\mu^2B^2)+\Delta\sigma^2(1+\mu^2B^2)^2}{(1+\mu^2B^2)^2}\right) + \left(\frac{\sigma_o^2\mu^2B^2}{(1+\mu^2B^2)^2}\right)}$$
$$= \frac{(\sigma_o + \Delta\sigma(1+\mu^2B^2))(1+\mu^2B^2)}{(\sigma_o^2(1+\mu^2B^2) + 2\sigma_o\Delta\sigma(1+\mu^2B^2) + \Delta\sigma^2(1+\mu^2B^2)^2)}$$

Assume that $\Delta\sigma^2(1+\mu^2B^2) \ll 2\sigma_o\Delta\sigma$

$$\rho_{xx} = \frac{\sigma_o + \Delta\sigma(1+\mu^2B^2)}{\sigma_o^2 + 2\sigma_o\Delta\sigma}$$

Now fit ρ_{xx} to R+αB^2 to get background (ignore the B dependence of WAL), where

$$R = \frac{\sigma_o + \Delta\sigma}{\sigma_o^2 + 2\sigma_o\Delta\sigma}$$
$$\alpha = \frac{\Delta\sigma\mu^2}{\sigma_o^2 + 2\sigma_o\Delta\sigma}$$

for $\Delta\sigma \ll \sigma_o$

$$R = \frac{1}{\sigma_o}$$
$$\alpha = \frac{\Delta\sigma\mu^2}{\sigma_o^2}$$

so now the background is subtracted from ρ_{xx}

$$\rho_{xx} - (R + \alpha B^2) = \frac{\sigma_o + \Delta\sigma(1+\mu^2B^2)}{\sigma_o^2 + 2\sigma_o\Delta\sigma} - \frac{1}{\sigma_o} - \frac{\Delta\sigma\mu^2B^2}{\sigma_o^2}$$

for $2\sigma_o\Delta\sigma \ll \sigma_o^2$

$$\rho_{xx} - (R + \alpha B^2) = \frac{\Delta\sigma}{\sigma_o^2}$$

Appendix G

WAL Data Fitting

This appendix collects the results of fitting the WAL data for various Sb well thicknesses at different temperatures. Out of the 14 Sb well thicknesses measured in Figure **6.2**, eight are shown here. The two thinnest wells were not measured because the layer was incomplete as determined from cross-sectional TEM studies. One sample, t702, with a well thickness of 3.6 nm was grown at a substrate temperature of 170°C was not included in this WAL study since a sample of the same well thickness was grown at a lower substrate temperature of 160°C leading to a better quality sample. The three uncapped samples did not have good quality WAL data due to a resistance mismatch between the superconducting indium contacts and the Sb quantum well. An Sb 5.2 nm well was only measured at low temperatures (< 0.5 K) so no extensive temperature study was possible.

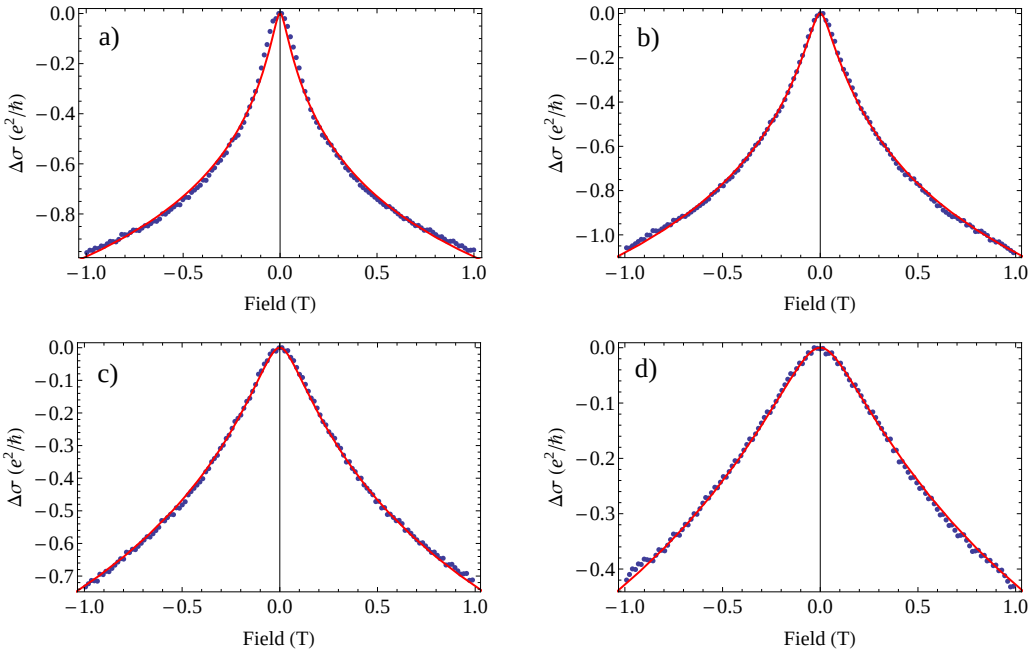

Figure G.1: Plot of the conductivity correction vs. field for a 2.3 nm well. The WAL data (blue dots) is fit using the HLN model (solid red line) at a) 1.5 K b) 4 K c) 8 K and d) 12 K.

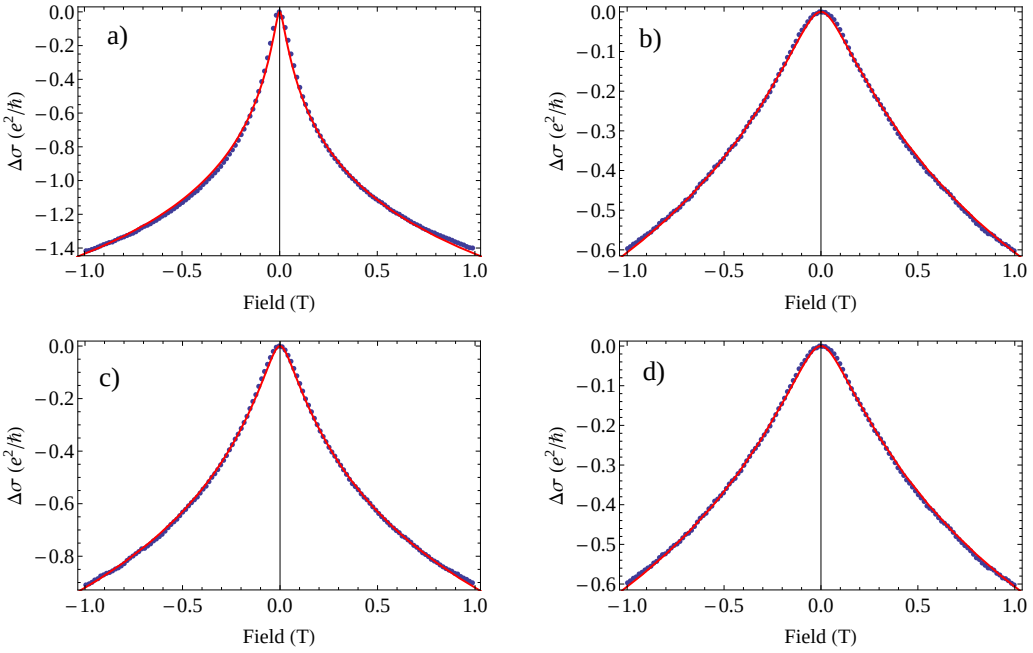

Figure G.2: Plot of conductivity correction vs field for a 4.0 nm well. The WAL data (blue dots) with is fit using the HLN model (solid red line) at a) 1.5 K b) 4 K c) 8 K and d) 12 K.

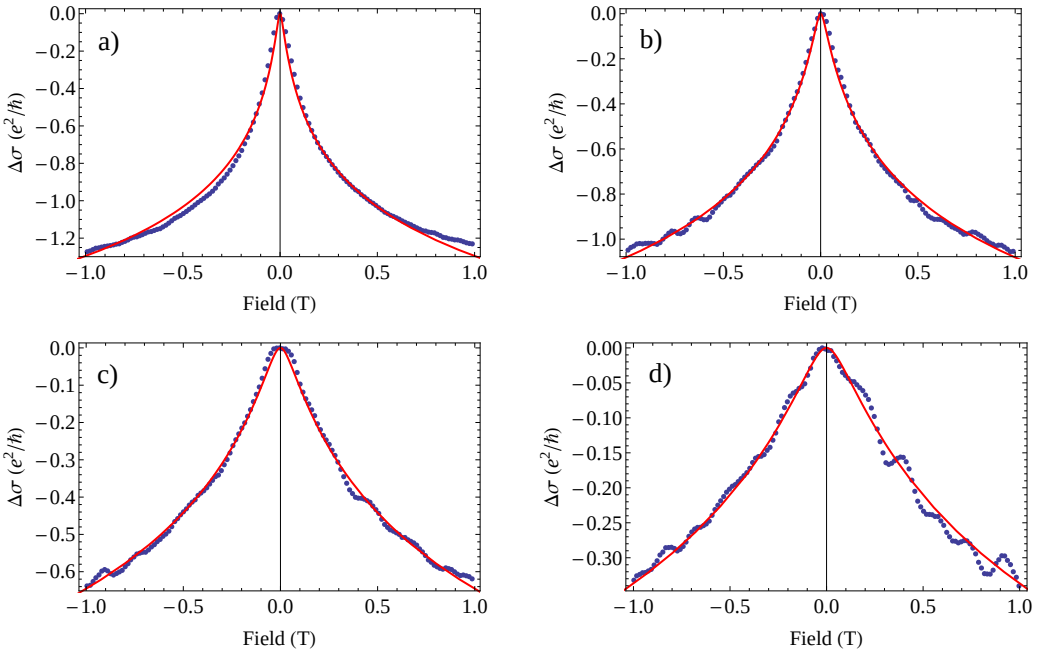

Figure G.3: Plot of conductivity correction vs field for a 3.6 nm well. The WAL data (blue dots) is fit by the HLN model (red solid line) at a) 1.5 K b) 4 K c) 8 K d) 12 K.

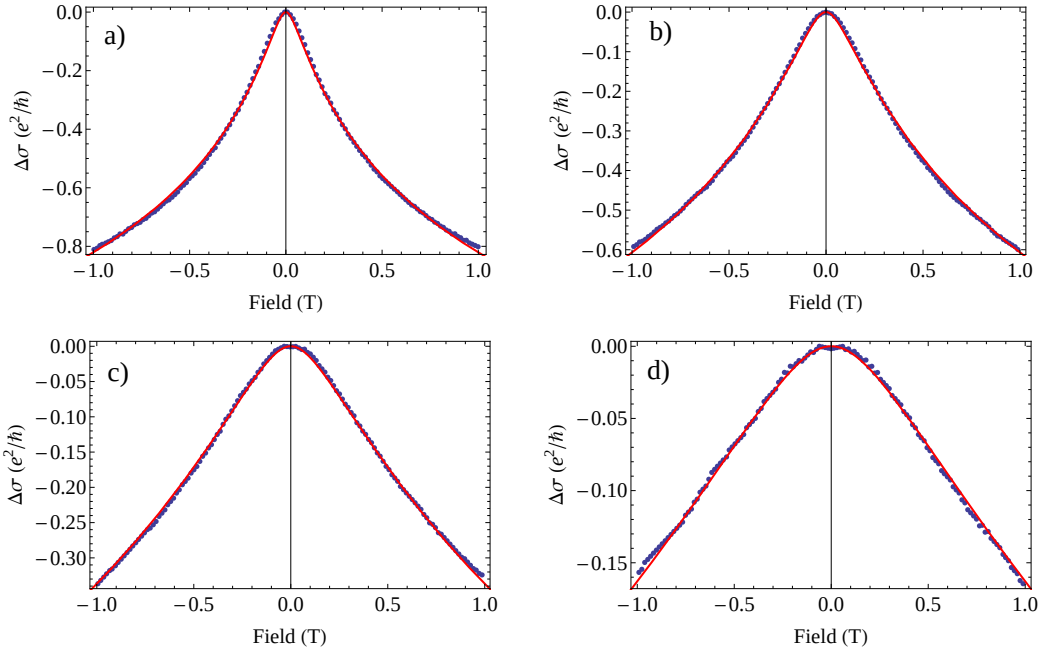

Figure G.4: Plot of conductivity correction vs field for a 1.8 nm well. The WAL data (blue dots) is fit by the HLN model (red solid line) at a)1.5 K b) 4 K c) 8 K d) 12 K.

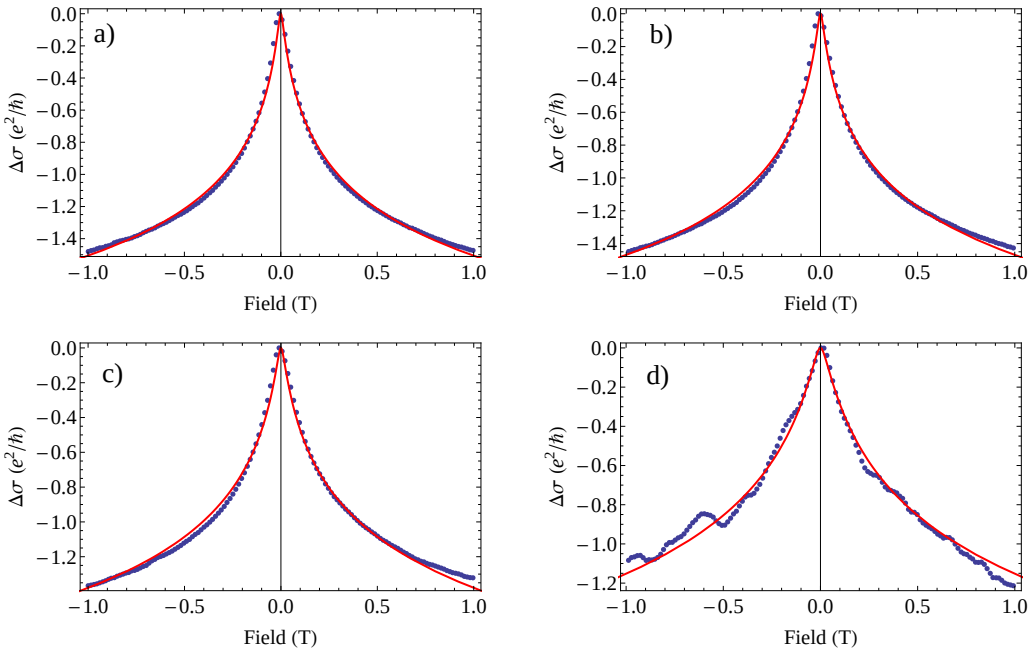

Figure G.5: Plot of conductivity correction vs field for a 2.3 nm well. The WAL data (blue dots) is fit by the HLN model (red solid line) at a) 0.3 K b) 1 K c) 2 K d) 4 K.

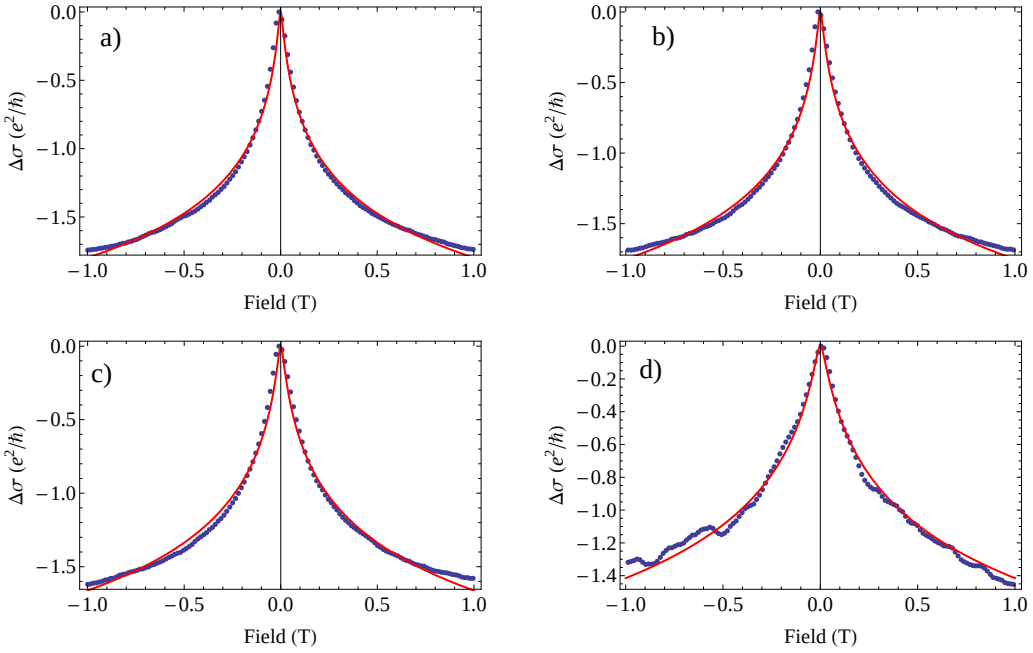

Figure G.6: Plot of conductivity correction vs field for a 2.7 nm well. The WAL data (blue dots) is fit by the HLN model (red solid line) at a) 0.3 K b) 1 K c) 2 K d) 4 K.

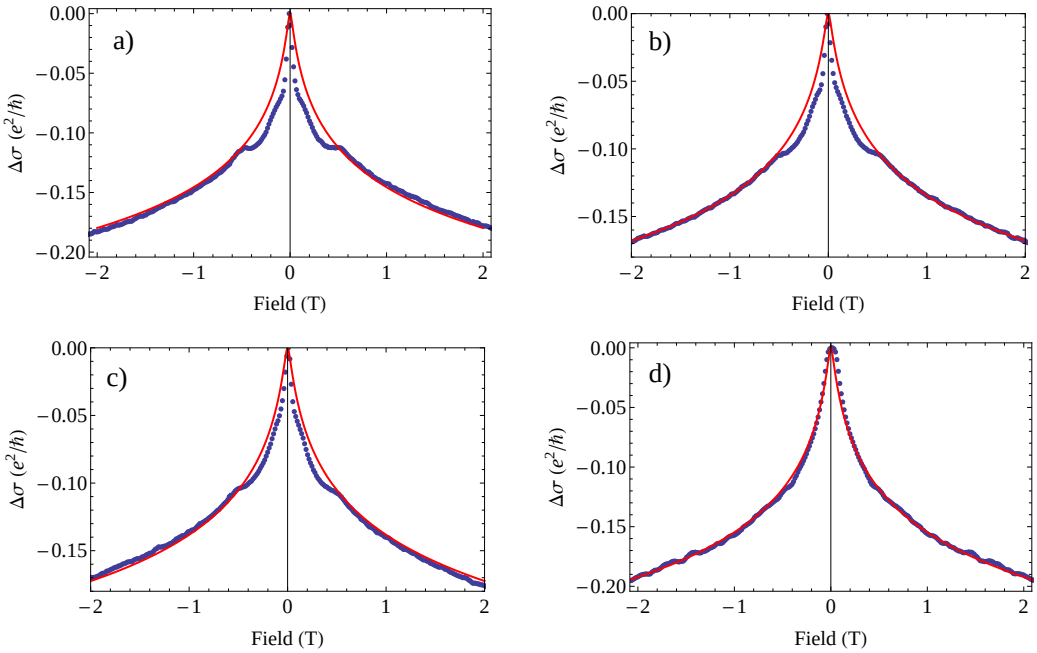

Figure G.7: Plot of conductivity correction vs field for a 4.5 nm well. The WAL data (blue dots) is fit by the HLN model (red solid line) at a) 0.3 K b) 1 K c) 2 K d) 4 K.

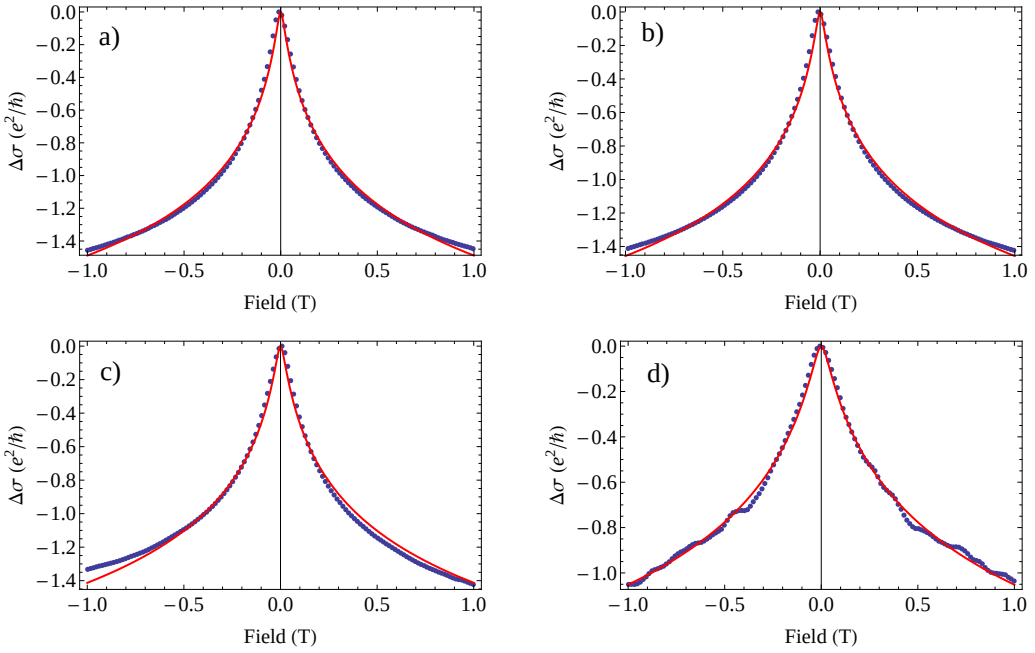

Figure G.8: Plot of conductivity correction vs field for a 3.6 nm well. The WAL data (blue dots) is fit by the HLN model (red solid line) at a) 0.3 K b) 1 K c) 2 K d) 4 K.

Appendix H

Hall Results

Hall measurements were made on van der Pauw samples and Hall bar devices; measured across multiple different growths of Sb quantum well thicknesses. The van der Pauw samples were measured using a closed cycle He-4 cryostat from 300 K to 20 K, in fields up to 0.12 T. The Hall bar devices were measured on a He-3/He-4 fridge at the National High Magnetic Field Laboratory in field up to 18 T. Hall traces for both types of sample show linear behavior up to 18 T (Figure **H.1**). Using the single carrier Hall result from Chapter 5 the carrier density can be determined from the slope of the line. Fits across multiple samples give a density ranging between 2 - 5x10^{14} cm^{-2}. The sign of the Hall slope indicates the type of carrier measured, in the case of our Sb wells we see p-type or hole conduction for all samples. This carrier density we believe is an overestimate of the carrier density present in our samples. Using theoretical band structure we calculate that the expected carrier density is $\sim$ 2x10^{12} cm^{-2}. From band structure, Sb is expected to exhibit multi-carrier conduction; this is because the Fermi level crosses an electron and hole pocket such that both types of carriers can participate in conduction.

Given that we expect multi-carrier conduction we can use the theoretical expressions for the longitudinal and transverse resistance[60] for multi-carrier conduction and attempt a fit to the data. The expressions for the longitudinal and

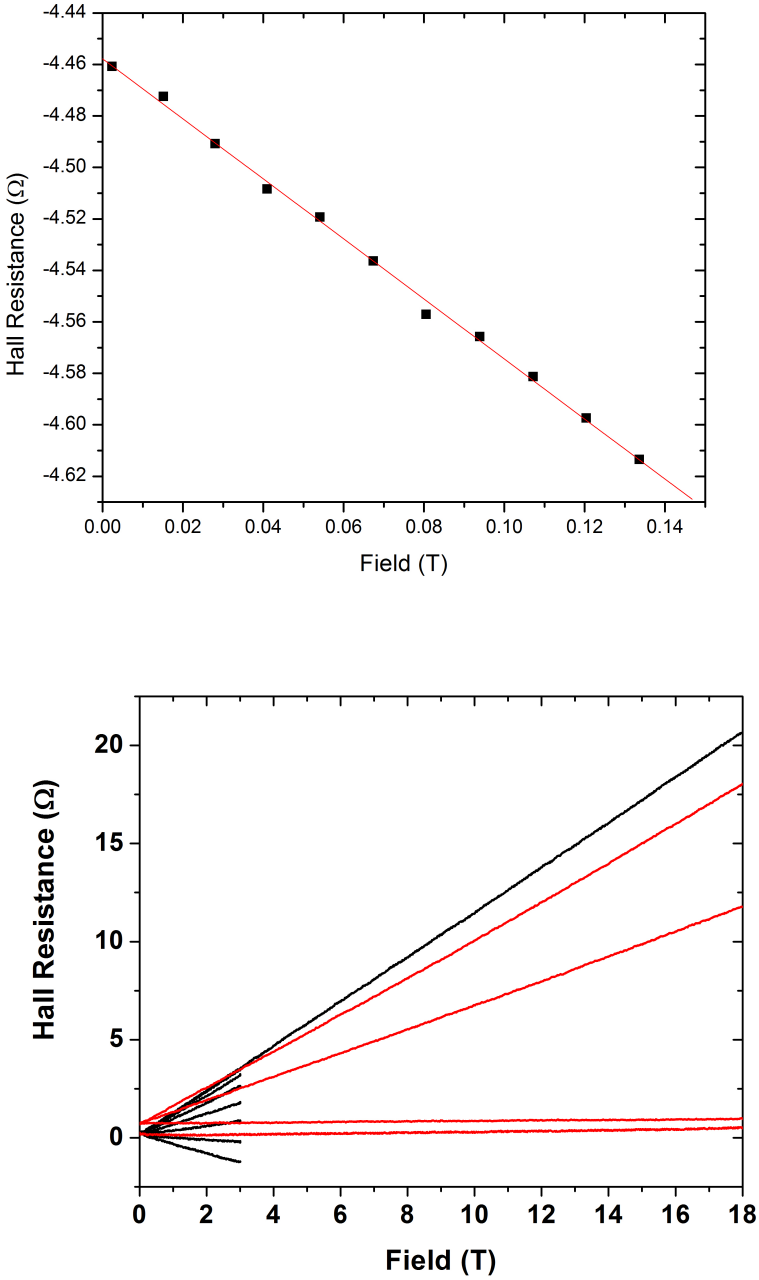

Figure H.1: Plot of Hall Resistance versus magnetic field. Hall signal is linear in both low field (<0.15 T) and up to 18 T. Plots shown are for a 3.6 nm well and are representative of the Hall traces across all well thicknesses. The change in sign of the slope is due to the experimental configuration because if the field direction is flipped that changes the sign of the Hall effect. Using the single carrier Hall equation, the slope gives a carrier density ranging between 2 - 5x10^{14} cm^{-2}.

transverse resistance are

$$R_{xx} = \frac{\rho_1\rho_2(\rho_1+\rho_2) + (R_2^2\rho_1 + R_1^2\rho_2)B^2}{(\rho_1+\rho_2)^2 + (R_1+R_2)^2B^2} \quad \textbf{(H.1)}$$

$$R_{xy} = \frac{(R_1\rho_2^2 + R_2\rho_1^2) + R_1R_2(R_1+R_2)B^2}{(\rho_1+\rho_2)^2 + (R_1+R_2)^2B^2} \quad \textbf{(H.2)}$$

where $R_{1,2} = \frac{1}{e\,n_{1,2}}, n_{1,2}$ is the carrier density for carrier 1 or 2, e is the elementary charge, $\rho_{1,2} = \frac{1}{e\,n_{1,2}\,\mu_{1,2}}$, $\mu_{1,2}$ is the mobility for carrier 1 or 2, and B is the magnetic field. From the above equations, there are four free fitting parameters: $n_1, n_2, \mu_1,$ andμ_2. Fits to both R_{xx} and R_{xy} did not provide well constrained fitting parameters; a reason being that the multi-carrier model has more free parameters than features in the data, which is over-specifying the results. This lack in features lead to fitting parameters being highly correlated such that multiple solutions for each parameter could give the overall same result.